FACULDADE DE ENGENHARIA DA UNIVERSIDADE DO PORTO

Fracture Strength of Metal Structures for Automotive Battery Systems Under Severe Impact Loading

Pedro Resende Conceição



Mestrado em Engenharia Mecânica

FEUP Supervisor: Prof. Pedro José da Silva Carvalho Pereira de Sousa

INEGI Supervisor: Eng. Tiago Miguel dos Reis Marques Domingues

July 29, 2026

© Pedro Resende Conceição, 2026

Fracture Strength of Metal Structures for Automotive Battery Systems Under Severe Impact Loading

Pedro Resende Conceição

Mestrado em Engenharia Mecânica

Approved in oral examination by the committee:

President: Prof. Mário Augusto Pires Vaz
Examiner: Prof. António Manuel de Bastos Pereira
Member: Prof. Pedro José da Silva Carvalho Pereira de Sousa

July 29, 2026

Resumo

As ligas de alumínio são cada vez mais usadas em caixas de bateria de veículos elétricos, onde têm de resistir ao impacto. A sua tenacidade à fratura sob carregamento dinâmico está pouco caracterizada, e os valores quase-estáticos não podem ser assumidos válidos às taxas de deformação atingidas numa colisão. Este trabalho mede a tenacidade à fratura das ligas AA2024 e AA6082-T651 sob carregamento quase-estático e dinâmico, usando uma única geometria de provete e um único procedimento de redução de dados, para permitir a comparação direta entre os dois regimes.

Os provetes de flexão das duas ligas foram maquinados a partir do material tal como recebido e pré-fissurados por fadiga antes do ensaio. Os entalhes laterais foram abertos após a pré-fissuração para guiar a frente de fenda. Ambas as ligas foram ensaiadas em flexão em três pontos nos dois regimes, e a tenacidade à fratura foi reduzida a uma curva de resistência J segundo a norma ASTM E1820. Os ensaios quase-estáticos correram numa máquina servo-mecânica. Os ensaios dinâmicos usaram uma Barra de Pressão Split-Hopkinson adaptada à flexão em três pontos, onde o evento dura algumas centenas de microssegundos e a carga é transmitida por ondas elásticas nas barras. A Correlação Digital de Imagem mediu o comprimento de fenda e a abertura da boca da fenda nos dois regimes, em substituição dos clip gauges que não conseguem seguir o evento dinâmico. A AA6082-T651, em grande medida insensível à taxa, serviu de referência. Espera-se que a sua tenacidade dinâmica iguale a quase-estática, pelo que reproduzi-la confirma a validade do setup antes de o resultado da AA2024 ser lido como um efeito de taxa.

A tenacidade de iniciação quase-estática foi de 8,4 kJ/m^2 para a AA2024 e 7,8 kJ/m^2 para a AA6082-T651. Sob carregamento dinâmico, a AA2024 subiu para 10,9 kJ/m^2, um aumento de cerca de 30%, enquanto a AA6082-T651 se manteve praticamente inalterada em 8,0 kJ/m^2. O mesmo quadro mantém-se a igual extensão de fenda, onde o J dinâmico fica 17 a 27% acima do ajuste quase-estático para a AA2024 e coincide com ele para a AA6082-T651, independentemente de como a iniciação é definida. A AA6082-T651 reproduziu a sua tenacidade quase-estática sob carregamento dinâmico e confirmou a validade do setup, pelo que o aumento medido na AA2024 reflete o comportamento do material. O efeito da taxa na tenacidade à fratura destas ligas é real, mas depende da liga.

Palavras-chave: tenacidade à fratura • ligas de alumínio • carregamento dinâmico • barra de Hopkinson • integral J • correlação digital de imagem

Abstract

Aluminium alloys are increasingly used in electric vehicle battery enclosures, where they must resist impact. Their fracture toughness under dynamic loading is not well characterised, and quasi-static data cannot be assumed to hold at the strain rates reached in a crash. This work measures the fracture toughness of AA2024 and AA6082-T651 under quasi-static and dynamic loading, using one specimen geometry and one data reduction to allow a direct comparison between the two regimes.

Single-edge notched bend specimens of both alloys were machined from the as-received material and fatigue pre-cracked before testing. Side grooves were cut after pre-cracking to guide the crack front. Both alloys were tested in three-point bending under the two regimes, and the fracture toughness was reduced to a J-resistance curve following ASTM E1820. The quasi-static tests ran on a servo-mechanical machine. The dynamic tests used a Split Hopkinson Pressure Bar adapted for three-point bending, where the event lasts a few hundred microseconds and the load is carried by elastic waves in the bars. Digital Image Correlation measured the crack length and the crack-mouth opening in both regimes, in place of the clip gauges and extensometers that cannot follow the dynamic event. The AA6082-T651, known to be largely rate-insensitive, served as a reference: its dynamic toughness is expected to match its quasi-static value, so reproducing it confirms that the setup is sound before the AA2024 result is read as a rate effect.

The quasi-static initiation toughness was 8.4 kJ/m^2 for the AA2024 and 7.8 kJ/m^2 for the AA6082-T651. Under dynamic loading the AA2024 rose to 10.9 kJ/m^2, an increase of about 30%, while the AA6082-T651 was practically unchanged at 8.0 kJ/m^2. The same picture holds at equal crack extension, where the dynamic J sits 17 to 27% above the quasi-static fit for the AA2024 and coincides with it for the AA6082-T651, independently of how initiation is defined. The AA6082-T651 reproduced its quasi-static toughness under dynamic loading and confirmed the setup, so the rise measured on the AA2024 reflects material behaviour. The rate effect on the fracture toughness of these alloys is real but depends on the alloy.

Keywords: fracture toughness • aluminium alloys • dynamic loading • split Hopkinson bar • J-integral • digital image correlation

Acknowledgements

The work presented here is the result of a long process, and it would not have been possible without the support of many people, to whom I owe my sincere thanks.

To my supervisors, Prof. Pedro Sousa and Eng. Tiago Domingues, for their guidance throughout the whole process, their constant availability, and the rigour with which they followed every stage of this work.

To INEGI and FEUP, for providing the conditions and the means that made this work possible. To the whole UMAI team, always available to help and supervise the experimental work, in particular to engineers Mário Cunha, Beatriz Silva and Daniela Azevedo, without whom the tests would not have been carried out.

To my friends from university and my friends from Tarouca, who were the balance of these years. The time spent with them gave me the rest and the good spirits that a work like this also demands. To the staff and players of ADR Tarouquense, with whom I shared that same balance on and off the pitch.

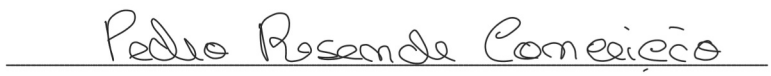
To my parents and my brother, for their unconditional support and for giving me the stability and the peace of mind to do the best work I am capable of.

To Luísa, for her love, patience and unconditional support throughout this journey.

Pedro Resende Conceição

Declaração de Honra

The author declares the use of generative AI in the research and writing process. According to the GAIDeT taxonomy (2025), the following tasks were delegated to GAI tools under full human supervision: literature search and systematization, code generation, code optimization, process automation, creation of algorithms for data analysis, visualization, proofreading and editing, summarizing text, translation, reformatting, quality assessment, and publication support. The GAI tool used was Claude Opus 4.8. Responsibility for the final manuscript lies entirely with the authors. GAI tools are not listed as authors and do not bear responsibility for the final outcomes.



"O que dá o verdadeiro sentido ao encontro é a busca, e é preciso andar muito para se alcançar o que está perto."

José Saramago

Contents

1 Introduction **1**
- 1.1 Context and Motivation . . . 1
- 1.2 Problem Statement . . . 1
- 1.3 Objectives . . . 2
- 1.4 Approach . . . 2
- 1.5 Dissertation Structure . . . 2

2 State of the Art **4**
- 2.1 Context and Motivation . . . 4
  - 2.1.1 Transition to electric mobility . . . 4
  - 2.1.2 Aluminium Alloys in Automotive Industry . . . 5
  - 2.1.3 Battery Enclosure Architecture and Material Selection . . . 7
- 2.2 Aluminium Alloys . . . 8
  - 2.2.1 The AA2024 . . . 9
  - 2.2.2 The AA6082-T651 . . . 11
- 2.3 Fundamentals of Fracture Mechanics . . . 13
  - 2.3.1 Stress Concentrations and the Energy Approach . . . 14
  - 2.3.2 Loading Modes . . . 15
  - 2.3.3 Stress Intensity Factor Formulation . . . 16
  - 2.3.4 Linear Elastic versus Elastic Plastic Fracture Mechanics . . . 17
  - 2.3.5 Elastic Plastic Fracture Mechanics Parameters . . . 18
  - 2.3.6 Stress Triaxiality and Constraint at the Crack Tip . . . 22
  - 2.3.7 J-Resistance Curves . . . 23
- 2.4 Mechanical Behaviour of Aluminium Alloys at High Strain Rates . . . 25
  - 2.4.1 Strain Rate Sensitivity . . . 25
  - 2.4.2 Adiabatic Heating and Thermal Softening . . . 26
  - 2.4.3 Effects of Strain Rate on Fracture Toughness . . . 27
- 2.5 Constitutive Modelling of the Dynamic Response . . . 27
- 2.6 Dynamic Experimental Techniques . . . 29
  - 2.6.1 The Split Hopkinson Pressure Bar (SHPB) . . . 29
  - 2.6.2 SHPB Adaptation for Three-Point Bending Fracture Testing . . . 30
  - 2.6.3 Digital Image Correlation . . . 32
- 2.7 Review of Related Studies and Research Gaps . . . 33

3 Experimental Methodology **37**
- 3.1 Overview of the Experimental Program . . . 37
- 3.2 Aluminium Alloys . . . 39
- 3.3 Specimen Design and Manufacturing . . . 40

3.3.1 Geometry and Dimensioning . . . 40
3.3.2 Crack-Plane Orientation . . . 41
3.3.3 Specimen Manufacturing . . . 42
3.4 Digital Image Correlation Methodology . . . 43
3.4.1 Speckle Pattern Design . . . 43
3.4.2 Speckle Application . . . 43
3.4.3 Imaging Hardware . . . 44
3.4.4 Calibration and Correlation Parameters . . . 45
3.4.5 Crack-Length Determination by DIC . . . 46
3.5 Tensile Characterisation of AA2024 . . . 48
3.5.1 Miniaturised Specimen Geometry . . . 48
3.5.2 Test Setup and Procedure . . . 49
3.5.3 Data Reduction . . . 50
3.6 Fatigue Pre-Cracking . . . 51
3.7 Quasi-Static Fracture Testing . . . 53
3.7.1 Apparatus and Fixtures . . . 53
3.7.2 Crack-Length Measurement on the Fracture Surface . . . 55
3.8 Dynamic Fracture Testing . . . 56
3.8.1 SHPB Apparatus and Three-Point Bending Fixtures . . . 56
3.8.2 Force Determination from the Transmitted Bar . . . 59
3.8.3 Dynamic Equilibrium Verification . . . 60
3.8.4 Synchronisation of Force and Crack Length . . . 60
3.8.5 Validity Window . . . 62

4 Results and Discussion **64**
4.1 Tensile Properties of AA2024 . . . 64
4.2 Quasi-Static Fracture . . . 66
4.2.1 *J-R* Curves and Initiation Toughness . . . 66
4.2.2 Validity Assessment . . . 68
4.2.3 Comparison and Fracture Behaviour . . . 70
4.3 Dynamic Fracture Behaviour . . . 71
4.3.1 SHPB Signals and Dynamic Equilibrium . . . 71
4.3.2 Validity Window Assessment . . . 74
4.3.3 Crack-Length and CMOD Histories . . . 75
4.3.4 Dynamic J-R Curves . . . 77
4.4 Setup Validation against the Quasi-Static Baseline . . . 80
4.4.1 Setup Development . . . 80
4.4.2 Comparison with the Quasi-Static Baseline . . . 81
4.5 Strain-Rate Effects on Fracture Toughness . . . 82
4.6 Methodological Discussion . . . 86

5 Conclusions and Future Work **88**
5.1 Conclusions . . . 88
5.2 Future Work . . . 89

References **90**

A Quasi-Static Fracture Surfaces **95**

B Dynamic Fracture Surfaces **97**

C SHPB Force Signals **99**

List of Figures

2.1 Ashby chart mapping yield strength against density for various material classes. Aluminium alloys achieve specific strength values comparable to or exceeding those of structural steels at roughly one third of the density. Source: Originally from [5], adapted from [52]. 6

2.2 Exploded view of a typical electric vehicle battery enclosure, showing the top cover, extruded frame, cooling plate, and bottom skid plate. Adapted from [59]. . 8

2.3 Intermetallic particle morphologies on the polished surface of AA2024-T3 identified by electron microprobe. Left: multiphase particles comprising Al_2CuMg (mauve) and Al_2Cu (orange) surrounded by a peripheral phase (cyan). Right: sub-phase regions of $Al_3(Cu,Fe,Mn)$ (brown) within a larger $Al_{20}(Cu,Fe,Mn)_5Si$ particle. Adapted from [12]. 9

2.4 Crack orientation designation system for wrought plate products according to ASTM E1820. L is the rolling direction, T the transverse direction, S the short transverse (thickness) direction. The first letter identifies the direction normal to the crack plane and the second the direction of crack propagation. Adapted from [10]. 10

2.5 Optical micrographs of as-cast AA6082 showing the coarse intermetallic phases identified by Keller's etch: needle-shaped β-Al_5FeSi (dark), script-type α-$Al_{15}(FeMn)_3Si_2$ (grey), Mg_2Si (black), and complex eutectic clusters within the α-Al matrix. These phases form during solidification and are retained after solution treatment and artificial ageing to T-651. From [45]. 12

2.6 Theoretical linear elastic stress singularity compared with the actual elastic-plastic stress distribution at the crack tip, showing the plastic zone [2]. 14

2.7 The three fundamental modes of fracture: Mode I (opening), Mode II (in-plane shear), and Mode III (out-of-plane shear) [2]. 15

2.8 Polar coordinate system (r,θ) at the crack tip [2]. 16

2.9 Fracture toughness specimen showing the characteristic dimensions a, $b-a$, and h. The same dimensional criterion applies to other standard geometries, including the SENB used in this work [14]. 18

2.10 Contour path Γ around a crack tip used to evaluate the J-integral [2]. 20

2.11 Typical J-R curve showing the blunting line, the 0.2 mm offset line, the tearing data, and the construction of the initiation toughness J_{Ic} [2]. 24

2.12 Analytical flow stress curves for the 6061-T6 aluminium alloy using the Johnson-Cook parameters [38], showing the isolated effects of strain rate hardening and thermal softening. 28

2.13 Schematic of the Split Hopkinson Pressure Bar, showing the bars, strain gauges, data acquisition system, and the synchronised high-speed imaging setup used for Digital Image Correlation. Adapted from [73]. 29

3.1 Overview of the experimental program. AA2024 is characterised in tension; both alloys are prepared as pre-cracked SENB specimens and tested under quasi-static and dynamic loading. The *J*-*R* curves from the two regimes are compared, validating the setup with AA6082-T651 and isolating the strain-rate effects on AA2024. 38
3.2 SENB specimen geometry and dimensions (mm), showing the machined V-notch before fatigue pre-cracking. 40
3.3 Side groove geometry. (a) groove profile (90° angle, 0.50 mm root radius, 0.75 mm depth per face); (b) machined specimen after EDM grooving. 42
3.4 Speckle patterns used in this work. (a) stamped pattern on a miniaturised tensile specimen; (b) sprayed pattern on a SENB fracture specimen. 44
3.5 Displacement field across the crack. (a) Vertical displacement v in a dynamic test, where the crack opens vertically. (b) Horizontal displacement u in a quasi-static test, where the specimen is rotated and the crack opens horizontally. The discontinuity along the crack separates the two halves, and the crack opening displacement is the jump across it. 47
3.6 Miniaturised tensile specimen geometry and dimensions (mm). 48
3.7 Tensile test setup, showing the Shimadzu AGX-V, the DIC camera, and the two LED lights. 49
3.8 Miniaturised tensile specimen in VIC-2D, showing the region of interest and the virtual extensometer used to measure strain. 50
3.9 Fatigue pre-cracking setup on the Step Lab machine, in three-point bending, with the travelling microscopes used to follow the crack on both faces. 51
3.10 Specimen after fatigue pre-cracking, showing the sharp crack extending from the machined notch. 53
3.11 Quasi-static fracture test setup on the STEPLab machine, in three-point bending, with the DIC camera and illumination. 54
3.12 Schematic of the quasi-static loading protocol, showing the calibration cycles, the incremental loading with partial unloadings, and the rise and fall of the force as the crack grows. The values are representative and vary between specimens and alloys. 55
3.13 Schematic of the dynamic three-point bending split Hopkinson bar, showing the gas gun, the striker, the incident and transmitted bars with their strain gauges, and the specimen held in the three-point bending fixture. Adapted from Shamchi [60]. 56
3.14 Copper pulse shaper mounted on the impact face of the incident bar. 58
3.15 High-speed imaging setup for the dynamic tests, with the Photron camera and the two GSVITEC LED units. 59
3.16 Lagrange diagram of the wave propagation in the bars, showing the incident, reflected, and transmitted pulses in the position-time plane, the pulse duration at the impact face, and the clean window in which the incident pulse is read at its gauge. 63

4.1 Engineering stress–strain curves of the five valid AA2024 tensile specimens. . . . 64
4.2 *J*-*R* construction for four of the valid quasi-static specimens, following ASTM E1820 Annex A9. Left column AA2024, right column AA6082-T651. Each plot shows the experimental points, the power-law fit, the blunting line, the 0.2 mm offset line, and the exclusion lines at 0.15 and 1.5 mm. 67
4.3 *J*-*R* construction for the remaining two quasi-static specimens, AA2024 (left) and AA6082-T651 (right), following the same procedure as Figure 4.2. 67

4.4 Fracture surface of a representative specimen of (a) AA2024 and (b) AA6082-T651. The two curved lines mark the fatigue pre-crack front (a_0) and the final crack front (a_f). Each length was measured at nine equally spaced points along these lines, following ASTM E1820. 71
4.5 Incident, reflected and transmitted strain signals over the full event, for one specimen of each alloy. 72
4.6 Incident, reflected and transmitted forces around the loading event, referred to the specimen. 73
4.7 Fracture surfaces showing the fatigue pre-crack front, from which the initial crack length was measured by the nine-point method. 76
4.8 Crack-length and CMOD histories over the loading window, for one specimen of each alloy. 77
4.9 Dynamic *J*-*R* curves for the four AA2024 specimens. Each plot shows the loading points at $\Delta a = 0$, the propagation points, the initiation point, and the blunting and exclusion lines. Specimen 2 is marked as marginal, since its initiation time falls within the uncertainty of the transition time, Section 4.3.2. 78
4.10 Dynamic *J*-*R* curves for the four AA6082-T651 specimens, following the same layout as Figure 4.9. 79
4.11 Incident and transmitted strains from a commissioning test, showing the spurious tensile spike on the incident signal that was traced to a debonded strain gauge. . . 81
4.12 Initiation toughness under quasi-static and dynamic loading for the two alloys. Bars are the mean of each set, error bars the standard deviation, and open circles the individual specimens. 83
4.13 AA2024 resistance behaviour under quasi-static and dynamic loading. The quasi-static fit is shown over its qualified range and the dynamic points directly, with the blunting and exclusion lines for reference. 85
4.14 AA6082-T651 resistance behaviour under quasi-static and dynamic loading, in the same layout as Figure 4.13. 85

A.1 Fracture surfaces of AA2024 95
A.2 Fracture surfaces of AA6082-T651 96

B.1 Fracture surfaces of AA2024 97
B.2 Fracture surfaces of AA6082-T651 98

C.1 Incident, reflected and transmitted forces, AA2024, specimen 1. 99
C.2 Incident, reflected and transmitted forces, AA2024, specimen 2. 100
C.3 Incident, reflected and transmitted forces, AA2024, specimen 3. 100
C.4 Incident, reflected and transmitted forces, AA2024, specimen 4. 101
C.5 Incident, reflected and transmitted forces, AA6082-T651, specimen 4. 101
C.6 Incident, reflected and transmitted forces, AA6082-T651, specimen 6. 102
C.7 Incident, reflected and transmitted forces, AA6082-T651, specimen 7. 102
C.8 Incident, reflected and transmitted forces, AA6082-T651, specimen 8. 103

List of Tables

2.1 Typical mechanical properties and specific strength values for representative automotive steel grades and aluminium alloys. Source: Adapted from Davies [22], European Aluminium [26], and ASM International [7]. 7
2.2 Representative plane-strain fracture toughness values for AA2024 plate in selected temper and orientation combinations. Source: [6]. 10
2.3 Summary of representative experimental studies on dynamic fracture toughness of aluminium alloys. 35

3.1 Test matrix of the experimental program. 39
3.2 Chemical composition of the AA6082-T651 batch (wt.%), from the EN 10204-3.1 inspection certificate. 39
3.3 Mechanical properties of the AA6082-T651 batch, from the EN 10204-3.1 inspection certificate. 40
3.4 Imaging hardware for the three DIC setups. 45
3.5 DIC correlation parameters for the three setups. 46
3.6 Fatigue pre-cracking parameters for the two alloys. 52

4.1 Tensile properties of the AA2024, measured on five valid specimens. 65
4.2 Quasi-static initiation toughness. K_{JIc} is converted from J_{Ic} with $E = 70$ GPa and $\nu = 0.33$. 68
4.3 ASTM E1820 validity criteria and outcome across the six specimens. The qualification criteria are met by all. The crack-extension capacity is exceeded in most specimens, which limits the valid range of the curve but not the initiation value. The criteria tied to a_{0q} apply only to the unloading-compliance method and are not required here. 69
4.4 Incident rise time, measured initiation time, and peak crack speed for the dynamic specimens. The initiation time is compared against the transition time, $t_T \approx 71$ µs, and the peak crack speed against the Rayleigh wave speed of aluminium, $c_R \approx 2900$ m/s. 74
4.5 Initial crack length a_0 of each specimen, from the nine-point method of ASTM E1820. 75
4.6 Dynamic initiation toughness. K_{Ji} is converted from J_i with $E = 70$ GPa and $\nu = 0.33$. 80
4.7 Dynamic J at the first propagation point compared with the mean quasi-static J at the same crack extension. The quasi-static value is the mean of the three power-law fits of the alloy, with its standard deviation. 84

List of Acronyms

AHSS	Advanced High-Strength Steel
ASTM	American Society for Testing and Materials
CMOD	Crack-Mouth Opening Displacement
CNC	Computer Numerical Control
COD	Crack Opening Displacement
CTOD	Crack Tip Opening Displacement
DIC	Digital Image Correlation
EDM	Electrical Discharge Machining
EPFM	Elastic-Plastic Fracture Mechanics
FEA	Finite Element Analysis
FOV	Field of View
fps	frames per second
GPB	Guinier-Preston-Bagaryatsky (zones)
HRR	Hutchinson-Rice-Rosengren (field)
HSLA	High-Strength Low-Alloy (steel)
LEFM	Linear Elastic Fracture Mechanics
LED	Light-Emitting Diode
SENB	Single-Edge Notched Bend
SHPB	Split Hopkinson Pressure Bar
UMAI	Unidade de Monitorização Avançada e Integridade Estrutural
ZNCC	Zero-Mean Normalised Cross-Correlation

Chapter 1

Introduction

1.1 Context and Motivation

The transition to electric mobility has made the battery enclosure one of the most safety-critical structures in the modern vehicle. It carries the battery pack low in the chassis, and in a crash it is the barrier between an intrusion and the cells, where a breach can lead to thermal runaway and fire. To keep the vehicle light while meeting this role, enclosures are built largely from aluminium alloys, which combine low density with the strength needed to absorb impact energy. The structural frame, the part that resists side-pole intrusion, is typically an extruded 6xxx-series profile, while higher-strength 2xxx alloys are candidates where greater load capacity is required.

In a crash, the enclosure is loaded in a few milliseconds, at strain rates far above those of a standard mechanical test. Under such loading a pre-existing flaw, a manufacturing defect or fatigue crack, can initiate and propagate before the surrounding material has time to redistribute the load. The property that governs this is the fracture toughness, the resistance of the material to the growth of a crack. Designing an enclosure that survives an impact, and building the failure models that predict it, therefore requires the fracture toughness of these alloys measured not only under quasi-static loading but at the high strain rates the structure actually sees.

1.2 Problem Statement

The fracture toughness of aluminium alloys under dynamic loading is far less established than under quasi-static loading. The quasi-static measurement is standardised and routine, but the dynamic case has no equivalent consensus. Reported studies use incompatible methods, test geometries, and loading rates, which makes their results hard to compare, and most report a single initiation value rather than a full resistance curve. For pre-cracked specimens of the alloys of interest here, dynamic fracture data are scarce. This leaves a gap between the loading the enclosure experiences in service and the data available to design against it.

1.3 Objectives

This work measures the fracture toughness of two aluminium alloys, AA2024 and AA6082-T651, under both quasi-static and dynamic loading, using a single consistent method so that the two regimes can be compared directly. The specific objectives are:

- to define an experimental methodology for fracture toughness testing of these alloys, covering specimen geometry, the applicable standard, the test setups, and the instrumentation;
- to manufacture, fatigue pre-crack, and test single-edge notched bend specimens of both alloys;
- to measure the quasi-static fracture toughness as a J-resistance curve following ASTM E1820;
- to measure the dynamic fracture toughness on a split Hopkinson bar adapted for three-point bending, at the high strain rates representative of impact;
- to use Digital Image Correlation to track crack growth in both regimes, in place of the mechanical methods that cannot follow a dynamic event;
- to assess the effect of loading rate by comparing the dynamic and quasi-static results for each alloy.

1.4 Approach

Both alloys are tested as single-edge notched bend specimens in three-point bending, fatigue pre-cracked before testing, and reduced to a J-resistance curve following ASTM E1820. The quasi-static tests run on a servo-mechanical machine and the dynamic tests on a split Hopkinson bar in a three-point bending configuration, where the event lasts a few hundred microseconds. Digital Image Correlation provides the crack length and the crack-mouth opening in both regimes from full-field surface measurements. The AA6082-T651, whose fracture toughness is known to be largely rate-insensitive, serves as a reference. Reproducing its quasi-static toughness under dynamic loading will inform on whether the setup is sound, so that the rate effects measured on the AA2024 can be read as material behaviour rather than experimental artefact.

1.5 Dissertation Structure

This dissertation is organised into five chapters. Chapter 1 introduces the context, the problem, and the objectives. Chapter 2 reviews the state of the art, covering the industrial context, the two alloys, the fundamentals of fracture mechanics, the behaviour of aluminium at high strain rates, the experimental techniques, and the existing dynamic fracture literature. Chapter 3 describes the experimental methodology, from specimen design and the digital image correlation setup to the quasi-static and dynamic test procedures. Chapter 4 presents and discusses the results, the tensile

properties, the quasi-static fracture toughness, and the dynamic behaviour. Chapter 5 draws the conclusions and outlines future work.

Chapter 2

State of the Art

The structural integrity of electric vehicle battery enclosures under high strain rate loading conditions depends directly on the fracture behaviour of their constituent aluminium alloys. Characterising this behaviour requires knowledge of both the mechanics of fracture and the dynamic phenomena that alter material response at elevated deformation rates. This chapter reviews the theoretical background for the present work, beginning with the industrial context and the characteristics of the aluminium alloys studied. The fundamentals of fracture mechanics are then reviewed, from linear elastic theory to the elastic-plastic parameters, namely the J-integral and crack tip opening displacement (CTOD), applicable when significant plastic deformation precedes crack extension. The Split Hopkinson Pressure Bar technique for high strain rate loading is then reviewed, followed by Digital Image Correlation as the non-contact optical method used to measure full-field surface displacements in both the quasi-static and dynamic fracture tests performed in this work. Finally, the existing literature is reviewed and the open questions addressed in this work are identified.

2.1 Context and Motivation

2.1.1 Transition to electric mobility

European emissions legislation is forcing the transition to electric mobility. Regulation (EU) 2023/851 requires a 100% reduction in CO_2 emissions from light vehicles by 2035 [29], and although a draft amendment in December 2025 relaxed this target to 90% [28], the regulatory push towards electrification remains clear. Market data supports this trend: according to the International Energy Agency's Global EV Outlook [35], electric vehicles already represented around 20% of global car sales in 2024, a share expected to reach 40% by 2030.

This transition brings a specific engineering problem. Lithium-ion battery packs are heavy, and that mass has to be compensated elsewhere in the vehicle structure. Aluminium alloys, with their high specific strength, are a natural choice. Data compiled by Ducker Carlisle for European Aluminium [27] shows that a European electric vehicle now contains on average 256 kg of aluminium. In battery enclosures in particular, aluminium is selected for its combination of strength, low density, and energy absorption capacity under dynamic loading [4].

The problem is that the structural performance of these enclosures under impact depends on the fracture behaviour of the alloys at high strain rates, and this is where the available knowledge falls short. Constitutive models such as Johnson-Cook and fracture simulation approaches such as Cohesive Zone Modelling are well established, but their accuracy at high strain rates is limited by the lack of experimental fracture data for the alloys actually used in these components. Chen et al. [17] showed that the fracture response of aluminium alloys depends simultaneously on strain rate and stress triaxiality, a coupled effect that standard models do not capture well. Olasumboye et al. [47] reached a similar conclusion, noting that the dynamic calibration of constitutive models for high-strength aluminium alloys remains unresolved. Obtaining reliable experimental fracture toughness data at high strain rates is the main motivation for this work.

2.1.2 Aluminium Alloys in Automotive Industry

In electric vehicles, the battery pack adds significant mass to the structure, and this has to be compensated through lighter materials in chassis members, battery enclosures, pillars, and suspension components [20]. Aluminium alloys are well suited for this role. Their density is about 2.7 g/cm^3 against 7.85 g/cm^3 for steel, and alloying and heat treatment raise their yield strength enough to give a specific strength well above that of conventional automotive steels, as shown in Figure 2.1.

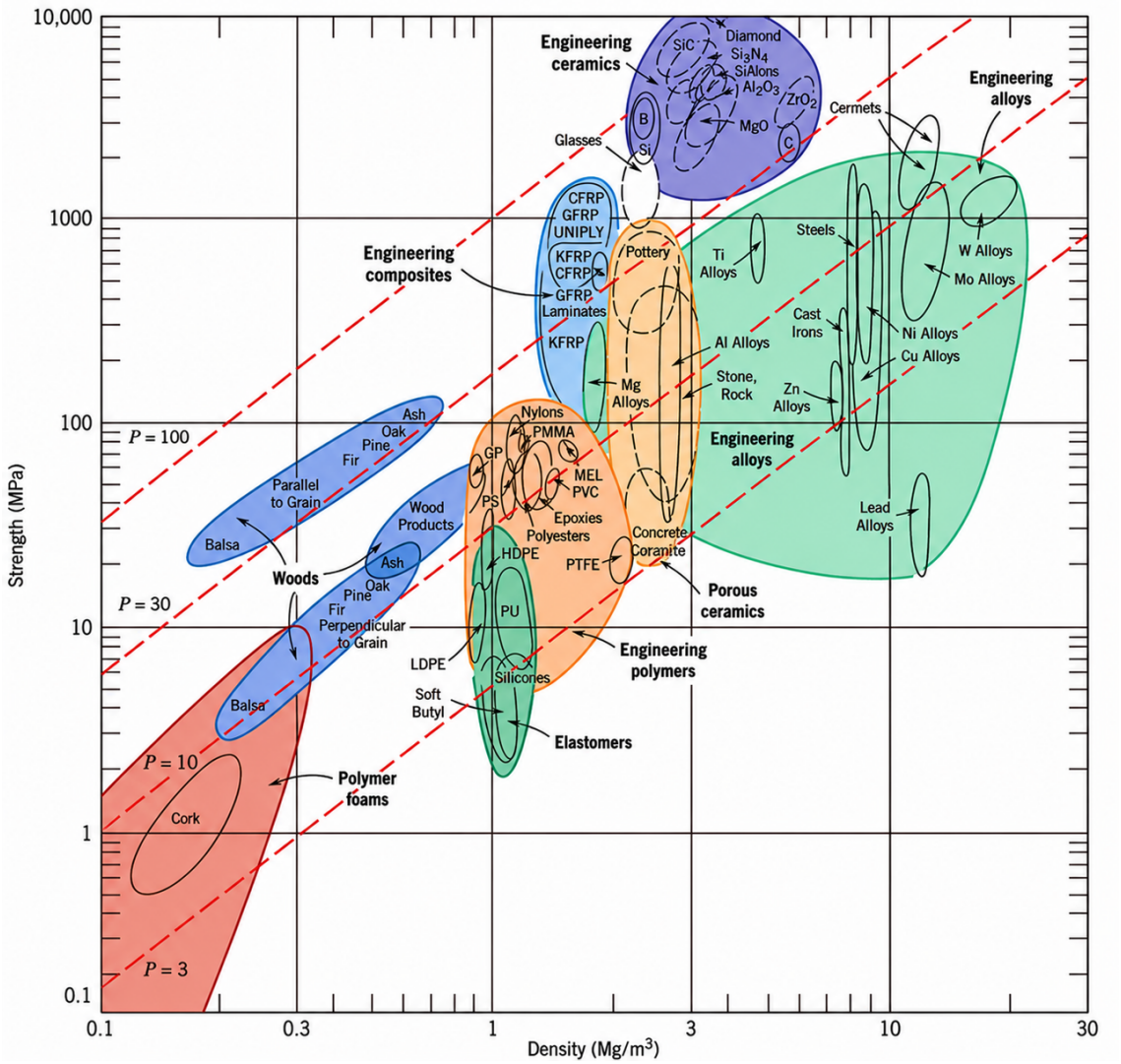


Figure 2.1: Ashby chart mapping yield strength against density for various material classes. Aluminium alloys achieve specific strength values comparable to or exceeding those of structural steels at roughly one third of the density. Source: Originally from [5], adapted from [52].

This advantage applies to strength-governed design. For stiffness-governed components, the elastic modulus of aluminium is roughly 70 GPa, about one third of the 210 GPa typical of steel [8], and thicker sections are needed to compensate, which partially offsets the mass saving. In the case of battery enclosures and crash members, where strength and energy absorption under impact are the governing criteria, specific strength is the relevant metric [20].

Table 2.1 compares yield strength and specific strength for steel grades and aluminium alloys used in current automotive applications. Pure aluminium has very low yield strength, but the addition of copper, magnesium, silicon, or zinc, combined with heat treatment, raises it considerably while keeping the density low [22].

Table 2.1: Typical mechanical properties and specific strength values for representative automotive steel grades and aluminium alloys. Source: Adapted from Davies [22], European Aluminium [26], and ASM International [7].

Material	Typical Automotive Application	Density, ρ (g/cm^3)	Yield Strength, σ_y (MPa)	Specific Strength (MPa·cm^3/g)
Mild Steel (DC04)	Exterior panels and non-structural components	7.85	150	19.1
HSLA Steel (HX340LAD)	Subframes, local reinforcements, and suspension	7.85	340	43.3
AHSS (DP600)	Structural chassis members and crash zones	7.85	400	51.0
Aluminium 6082-T6	Extrusions for crash boxes and battery enclosures	2.70	260	96.3
Aluminium 2024-T3	Aerospace structures; reference alloy for constitutive model validation	2.78	345	124.1
Aluminium 7075-T6	Ultra-high-strength structural applications	2.81	503	179.0

Among these, AA2024 from the 2xxx series is one of the most studied aluminium alloys under both quasi-static and dynamic loading. Its primary application is in aerospace structures [22]; however, the extensive experimental database available for this alloy makes it a practical reference for developing and validating constitutive and fracture models, which is why it was selected for this study.

2.1.3 Battery Enclosure Architecture and Material Selection

This specific strength advantage is the reason aluminium alloys dominate battery enclosure design. These enclosures are not simple boxes. They combine structural protection, thermal management, electromagnetic shielding, and environmental sealing in a single assembly [4], and each subsystem has different functional demands that call for different alloy families [15].

As shown in Figure 2.2, the enclosure is built from several distinct layers. The housing (aluminium extrusion) is the most structurally demanding component. It provides torsional stiffness to the enclosure and acts as the primary barrier against intrusion during side pole impacts, absorbing energy through the progressive plastic folding of hollow cross-sections [4]. Multi-cavity extruded profiles from the 6xxx series (typically 6082-T6 or 6063-T6) are the standard choice here, because they combine the yield strength needed for crash performance with the extrudability required to produce complex hollow geometries. The Audi e-tron GT frame is one documented example of this approach [18]. The single cooling plate (brazing), positioned directly adjacent to the serviceable lean modules, has a different set of requirements. Its function is to maintain cell temperatures within safe operating limits and prevent thermal runaway [4]. This demands high thermal conductivity and enough formability for stamping and brazing operations, which makes the 3xxx series (such as 3003) and certain 1xxx grades common choices for this application. The top lid carries no

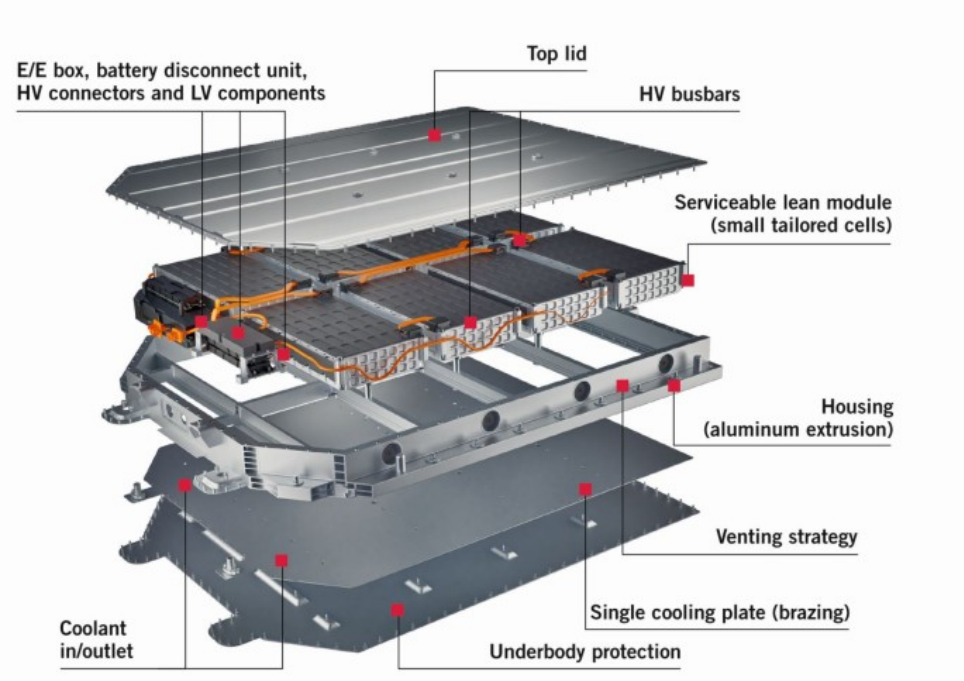


Figure 2.2: Exploded view of a typical electric vehicle battery enclosure, showing the top cover, extruded frame, cooling plate, and bottom skid plate. Adapted from [59].

primary structural load from the vehicle chassis. It provides environmental sealing, fire containment, and electrical isolation of the cells from the passenger compartment. Thin stamped sheets from the 5xxx series, particularly 5754, are typically used because they offer good formability, stable work-hardening behaviour, and natural corrosion resistance [63]. The underbody protection faces a different problem altogether. It must resist puncture from road debris and localised vertical impacts, meaning the governing failure mode is penetration rather than global deformation. This requires high yield strength combined with resistance to fracture under concentrated loading. High-strength 5xxx alloys (5182, 5754) and 6xxx grades are used, sometimes in multi-layered configurations for extreme protection requirements [69]. What ties all of this together is the housing. During a crash, it is the component that absorbs kinetic energy through plastic deformation of its aluminium profiles. How well it performs under high strain rate loading sets the limit for the entire battery system, and that performance depends directly on the fracture behaviour of the constituent alloys under dynamic conditions.

2.2 Aluminium Alloys

Two aluminium alloys are studied in this work, AA2024 and AA6082-T651. They belong to different alloy systems, Al-Cu-Mg and Al-Mg-Si, and harden through different precipitates and particle populations. These differences set their fracture behaviour, described for each alloy in Sections 2.2.1 and 2.2.2.

2.2.1 The AA2024

2.2.1.1 Chemical Composition and Microstructure

The AA2024 alloy belongs to the Al–Cu–Mg system. Its nominal composition consists of an aluminium matrix with copper (3.8–4.9 wt.%), magnesium (1.2–1.8 wt.%), and manganese (0.3–0.9 wt.%) as principal additions, with iron and silicon as residual impurities [7]. The mechanical strength of this alloy comes from precipitation hardening. In the naturally aged tempers (T3, T4, T351), solution heat treatment followed by ageing produces a fine distribution of Cu–Mg co-clusters and Guinier-Preston-Bagaryatsky (GPB) zones, which are nanoscale atomic aggregates that act as obstacles to dislocation motion [65].

Besides these fine precipitates, the microstructure contains coarse intermetallic particles, mainly Al_7Cu_2Fe and Al_2CuMg, that form during solidification and are not dissolved by subsequent heat treatment [12]. These particles, with diameters typically between 1 and 20 μm, are visible in Figure 2.3.

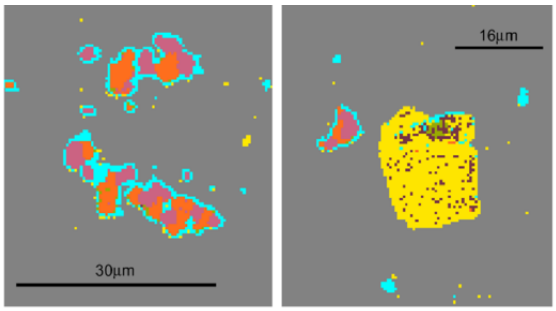


Figure 2.3: Intermetallic particle morphologies on the polished surface of AA2024-T3 identified by electron microprobe. Left: multiphase particles comprising Al_2CuMg (mauve) and Al_2Cu (orange) surrounded by a peripheral phase (cyan). Right: sub-phase regions of $Al_3(Cu,Fe,Mn)$ (brown) within a larger $Al_{20}(Cu,Fe,Mn)_5Si$ particle. Adapted from [12].

These intermetallics are what controls the toughness of the alloy. Under plastic deformation, stress concentrations at the particle–matrix interface cause void nucleation, either by particle cracking or by debonding. The voids then grow and coalesce, leading to the ductile fracture typical of this alloy [2, 53]. The size, spacing, and volume fraction of these particles directly affect the resistance to stable crack growth, which is the property that the experimental work in this thesis aims to measure.

2.2.1.2 Fracture Toughness Properties

For flaw-tolerant design, the relevant property is not yield strength but fracture toughness. In AA2024, fracture is driven by the previously described void nucleation and coalescence mechanism, and the measured toughness depends on the temper condition, the specimen orientation relative to the rolling direction, and the level of constraint at the crack tip.

The orientation dependence comes from the processing of the plate. Thermomechanical processing of wrought aluminium plate produces elongated grains and aligns the intermetallic particles along the rolling direction. Fracture toughness is therefore anisotropic, and values must be reported using the crack orientation system defined in ASTM E1820 [9], shown in Figure 2.4.

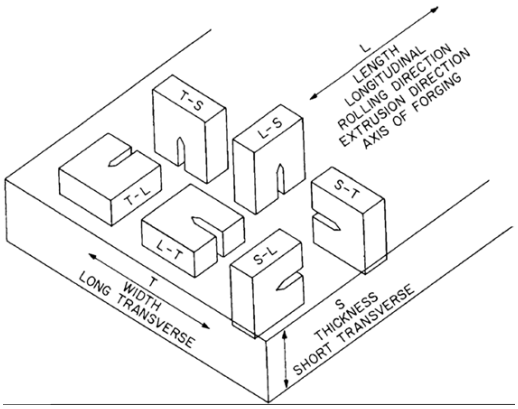


Figure 2.4: Crack orientation designation system for wrought plate products according to ASTM E1820. L is the rolling direction, T the transverse direction, S the short transverse (thickness) direction. The first letter identifies the direction normal to the crack plane and the second the direction of crack propagation. Adapted from [10].

The two orientations most commonly reported for plate products are L-T and T-L. In L-T, the crack propagates transversely and has to cross the elongated grain boundaries, which tends to give higher toughness. In T-L, propagation follows the rolling direction along the aligned particles and grain boundaries, and toughness is correspondingly lower, typically by 10–15% for the same temper [6].

The combined effect of temper and orientation is summarised in Table 2.2, which lists representative plane-strain fracture toughness values for AA2024 in several temper and orientation combinations.

Table 2.2: Representative plane-strain fracture toughness values for AA2024 plate in selected temper and orientation combinations. Source: [6].

Temper	**Orientation**	K_{Ic} **(MPa$\sqrt{\mathrm{m}}$)**
T3	L-T	23–26
T3	T-L	20–23
T351	L-T	22–27
T4	L-T	24–28
T6	L-T	20–23
T8	L-T	20–22

Among these tempers, the naturally aged conditions (T3, T4, T351) tend to give the highest toughness. Artificial ageing to T6 or T8 raises yield strength but reduces K_{Ic}, which is consistent

with the well-known strength-toughness trade-off in precipitation-hardened alloys: overageing coarsens the precipitate distribution, increasing the flow stress but also reducing the spacing between potential void nucleation sites [13].

2.2.1.3 Elastic-plastic characterisation and the J-R curve

For the specimen thicknesses and geometries relevant to this study, the plane-strain condition required for a valid K_{Ic} measurement is not always met in AA2024, given its combination of moderate yield strength and relatively high toughness. When this happens, LEFM does not apply and the characterisation must use Elastic-Plastic Fracture Mechanics (EPFM), with the J-integral as the crack driving force [2].

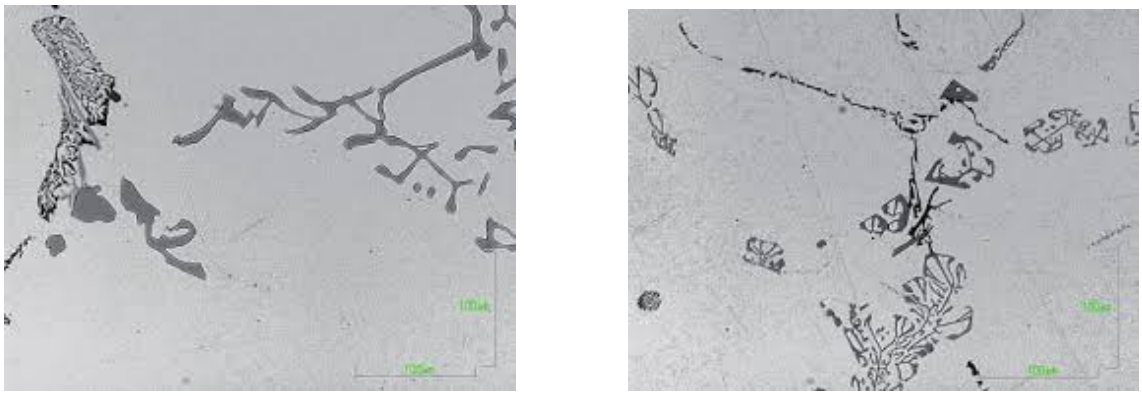
The resistance to stable crack extension is then quantified through the J-R curve, following the procedure in ASTM E1820 [9]. No direct J_{Ic} data were found for these tempers. Converting the K_{Ic} values of Table 2.2 through $J = K_{Ic}^2/E'$, with $E' = E/(1-\nu^2)$, gives an equivalent J_{Ic} of roughly 5 to 10 kJ/m^2 for AA2024 in naturally aged tempers. This is an elastic conversion of the plane-strain values, not measured J_{Ic}, and serves only as an order-of-magnitude reference. Moreover, J_{Ic} is sensitive to test conditions, which means that literature values cannot be used directly for model calibration. The J-R curve must be measured on specimens from the same material batch and with the same geometry used in the dynamic tests.

The exact temper condition of the AA2024 plate used in this study was not specified by the supplier. Tensile tests were therefore carried out to determine the actual yield and ultimate tensile strengths of the as-received material. These results, presented in Chapter 4, define the baseline mechanical properties against which the published data in Table 2.2 can be compared.

2.2.2 The AA6082-T651

2.2.2.1 Chemical Composition and Microstructure

AA6082 belongs to the Al–Mg–Si system. Its nominal composition, according to EN 573-3, includes silicon (0.7–1.3 wt.%), magnesium (0.6–1.2 wt.%), and manganese (0.4–1.0 wt.%) as the main additions, with iron below 0.50 wt.% and copper below 0.10 wt.% [7]. The copper content is an order of magnitude lower than in AA2024, which gives AA6082 better general corrosion resistance but also means a completely different precipitate chemistry and a different population of coarse particles [23]. The coarse intermetallic phases that control the fracture behaviour of the alloy form during solidification. Mrówka-Nowotnik et al. [45] identified five types of intermetallic compounds in as-cast 6082 using optical microscopy with Keller's etch and X-ray diffraction (Figure 2.5). The main phases are β-Al_5FeSi, which appears as dark, needle-shaped particles, α-$Al_{15}(FeMn)_3Si_2$, which forms in a characteristic script morphology, and Mg_2Si, visible as black compact particles. Al_9Mn_3Si and α-$Al_{12}Fe_3Si$ were also detected. Some of these phases grow together into complex eutectic clusters within the α-Al matrix.



(a) (b)

Figure 2.5: Optical micrographs of as-cast AA6082 showing the coarse intermetallic phases identified by Keller's etch: needle-shaped β-Al_5FeSi (dark), script-type α-$Al_{15}(FeMn)_3Si_2$ (grey), Mg_2Si (black), and complex eutectic clusters within the α-Al matrix. These phases form during solidification and are retained after solution treatment and artificial ageing to T-651. From [45].

The manganese addition is relevant here. It promotes the transformation of the needle-shaped β-Al_5FeSi into the more compact α-Al(FeMn)Si phase, which is less harmful mechanically, and forms fine Al–Mn–Si dispersoids that pin grain boundaries and help control the recrystallised grain structure [45].

These coarse intermetallics survive the T651 heat treatment. The solution treatment dissolves the fine Mg_2Si precipitates back into solid solution, and the subsequent artificial ageing produces a dense distribution of metastable β'' needles, which are the nanoscale precipitates responsible for the strength of the T651 condition [53]. But the coarse Fe-rich intermetallics and the large eutectic Mg_2Si particles are too stable to dissolve at the solution treatment temperature. Mrówka-Nowotnik and Sieniawski [44] confirmed this by measuring fracture toughness of 6082 after different ageing treatments: the fracture surfaces consistently showed large dimples nucleated around the coarse Al_8Fe_2Si and Al_5FeSi particles, with smaller dimples around the finer hardening precipitates.

The fracture mechanism is therefore the same as described for AA2024 in Section 2.2.1.1: plastic deformation causes stress concentrations at the particle–matrix interface, voids nucleate by particle cracking or debonding, grow, and coalesce into a macroscopic crack. What differs between the two alloys is the particle population. In AA2024, the dominant nucleation sites are Al_7Cu_2Fe and Al_2CuMg. In AA6082, they are Fe-rich intermetallics (β-Al_5FeSi, α-Al(FeMn)Si) and coarse Mg_2Si. The volume fraction, spacing, and morphology of these particles differ, which is why the two alloys have different toughness values despite broadly similar yield strengths.

2.2.2.2 Quasi-Static Mechanical Properties

The mechanical properties of AA6082 in the peak-aged condition typically fall around 250–290 MPa in yield strength and 290–320 MPa in tensile strength, with about 8–12% elongation [8,

17]. The specific T651 plate used in this work was supplied with an EN 10204-3.1 inspection certificate. Its certified properties are given in Table 3.3, with a certified yield strength of 321 MPa, above the typical range.

It remains below the 345 MPa of AA2024-T3, but the specific strength stays competitive. For battery enclosure frames, where the governing requirement is energy absorption through plastic folding rather than peak load, the moderate strength and good ductility of AA6082-T651 matter more than the higher yield of the 2xxx series.

The crack orientation system of Section 2.2.1.2 applies in the same way, and the SENB specimens are machined with the same orientation as those of AA2024.

Fracture toughness data for 6082 in the peak-aged condition are less abundant than for AA2024 but broadly consistent across sources. Reported K_{Ic} values for plate and extruded products in the L-T orientation fall between 20 and 29 MPa$\sqrt{\text{m}}$ [44], clustering around 23–26 MPa$\sqrt{\text{m}}$. These are somewhat lower than the T3 and T4 tempers of AA2024 (Table 2.2), consistent with the lower toughness of peak-aged conditions in aluminium alloys [13].

With the certified yield strength of 321 MPa and the criterion $B \geq 2.5\,(K_{Ic}/\sigma_{YS})^2$, a valid LEFM measurement would need a thickness of about 22 mm for a conservative $K_{Ic} \approx 30$ MPa$\sqrt{\text{m}}$, and 13 to 16 mm for the 23–26 MPa$\sqrt{\text{m}}$ reported in the literature. The SENB specimens have $B = 7.5$ mm, well below either limit. LEFM does not apply, and the characterisation uses the J-integral.

Chen et al. [17] studied the flow and fracture behaviour of AA6082-T6 over a wide range of strain rates, from quasi-static (10^{-4} s^{-1}) to dynamic (3.4×10^{3} s^{-1}), using smooth and notched specimens. They found that the alloy is relatively insensitive to strain rate in terms of flow stress, with a moderate rate effect between 10^{-3} and 1 s^{-1} that is partly offset by adiabatic heating at higher rates. They also calibrated a Johnson-Cook model and a fracture locus as a function of stress triaxiality. Their work provides a useful baseline for the dynamic response of this alloy, but does not include pre-cracked fracture specimens or J-integral measurements, which is the gap addressed by the present work. The low rate sensitivity also has a practical advantage for the experimental campaign. Although Chen et al. tested the T6 temper, the low strain-rate sensitivity reflects the deformation behaviour of the Al-Mg-Si system and is not expected to differ appreciably between T6 and the T651 used here. Because the dynamic toughness should not differ drastically from the quasi-static value, AA6082-T651 allows the new SHPB three-point bending setup to be validated against a known baseline before rate effects are interpreted as material behaviour.

2.3 Fundamentals of Fracture Mechanics

Classical strength-of-materials design compares the applied stress to the yield or ultimate strength of the material, assuming the component behaves as a continuous and homogeneous medium. Real components do not. They contain cracks, inclusions, and welding defects that concentrate stress locally, and the stress at the tip of such a flaw can be far higher than the nominal applied stress. This is why structures sometimes fail at loads well below their nominal yield strength [2].

This limitation became impossible to ignore in the mid-twentieth century. The Liberty ships of World War II are the textbook example: several of these welded cargo vessels broke in half in cold waters at stresses well below the yield strength of their steel hulls [2]. The early De Havilland Comet jetliners failed in similar circumstances. Both cases made clear that yield strength alone is not enough to predict structural failure when flaws are present.

Fracture mechanics emerged as the framework that links applied stress, flaw size, and the material's resistance to crack growth. Its foundations were laid by Griffith [32] in 1921, using a thermodynamic energy balance to describe brittle fracture, and extended in the 1950s by Irwin [36], who built on the crack-tip stress field solutions of Westergaard [67] to make the theory work for engineering metals. The same ideas apply directly to this work. To measure how AA2024 resists crack growth under dynamic loading, the nominal stress in the specimen is not enough. What matters is the stress and energy at the crack tip, and that is what the rest of this chapter is about, with focus on the elastic-plastic regime where ductile aluminium alloys actually fail.

2.3.1 Stress Concentrations and the Energy Approach

When a sharp crack is loaded, the stress field right ahead of the crack tip rises sharply. Linear elastic analysis predicts that the stress goes to infinity at the tip itself, which is not what happens in practice. In real metals, once the local stress reaches the yield strength, the material yields locally and a small plastic zone forms ahead of the crack, as shown in Figure 2.6. The stress stays finite, but the mathematical singularity from the elastic solution makes traditional maximum-stress failure criteria useless for cracked components.

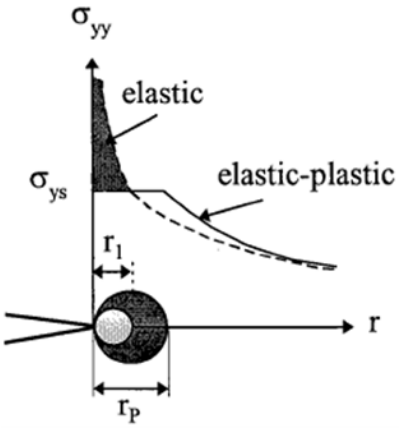


Figure 2.6: Theoretical linear elastic stress singularity compared with the actual elastic-plastic stress distribution at the crack tip, showing the plastic zone [2].

The way around this is to look at the problem from an energy point of view rather than a stress one. As a crack grows, elastic strain energy stored in the body is released. The rate at which this happens, per unit of new crack area, is called the energy release rate G [2]:

$$G = -\frac{\partial U}{\partial A} = -\frac{1}{b}\frac{\partial U}{\partial a} \tag{2.1}$$

where U is the strain energy, A the crack area, a the crack length, and b the thickness. The crack propagates when G reaches a critical value G_c, which is a property of the material.

This idea is due to Griffith [32], who applied it to brittle materials. He assumed that the released elastic energy goes entirely into creating new fracture surfaces, so G_c is set by the specific surface energy γ_s. For a centre crack of length $2a$ in an infinite plate, the critical stress is:

$$\sigma_c = \sqrt{\frac{2E\gamma_s}{\pi a}} \tag{2.2}$$

Griffith's expression works well for glass and ceramics, but it falls short for metals by orders of magnitude. The reason is the plastic zone in Figure 2.6: in a ductile material, most of the energy released by the advancing crack is spent on plastic deformation around the tip, not on creating new surface. Orowan [48] fixed this by adding a plastic work term γ_p to the energy balance:

$$\sigma_c = \sqrt{\frac{2E(\gamma_s + \gamma_p)}{\pi a}} \tag{2.3}$$

In structural metals, γ_p is much larger than γ_s, often by three or four orders of magnitude [2]. The practical consequence is that the toughness of a ductile alloy is set almost entirely by how much plastic work it can dissipate at the crack tip before the crack advances. This is the basic idea that the rest of this chapter develops, first within linear elastic fracture mechanics and then in the elastic-plastic regime relevant to AA2024.

2.3.2 Loading Modes

A crack can open up in three different ways depending on how the load is applied relative to the crack plane. Fracture mechanics calls these the three fundamental loading modes [2], shown in Figure 2.7.

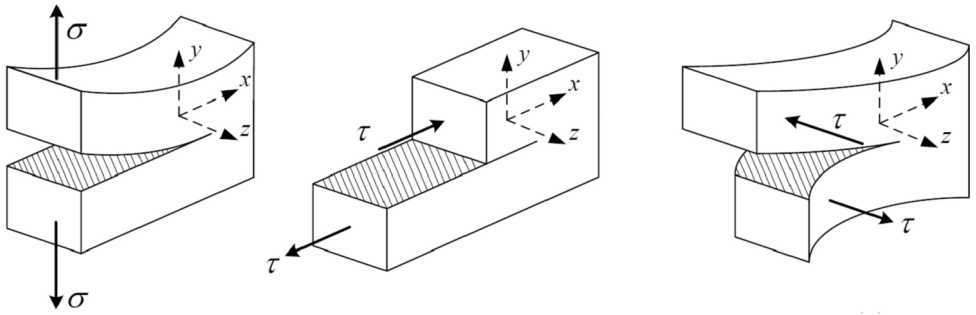


Figure 2.7: The three fundamental modes of fracture: Mode I (opening), Mode II (in-plane shear), and Mode III (out-of-plane shear) [2].

In Mode I, the load pulls the crack surfaces straight apart. This is the opening or tensile mode. Mode II is in-plane shear: the load slides the surfaces past each other, parallel to the crack plane and perpendicular to the crack front. Mode III is out-of-plane shear, where the surfaces slide sideways along the crack front [2].

Real components often see a mix of these, but Mode I is the one that typically matters most. Most engineering materials, including aluminium alloys, resist crack growth far less under pure tensile opening than under shear [2], which makes Mode I the worst case.

This is directly relevant to battery enclosures. During a crash, the aluminium profiles absorb energy by folding. The component as a whole is being compressed, but each fold puts the outer surface under high local tension. Any pre-existing defect or microcrack in that region gets pulled open, which is a Mode I situation in practice. Since this localised tearing is what eventually limits how much energy the profile can absorb, testing the fracture toughness under pure Mode I is both the most representative and the most conservative choice for this work.

2.3.3 Stress Intensity Factor Formulation

The energy approach indicates when a crack will grow, but says nothing about the stresses around the tip. The stress field there was first worked out by Westergaard [67] in 1939 for an infinite cracked plate, and generalised by Irwin [36]. The result is one of the most useful in fracture mechanics: the stress field very close to the crack tip always has the same shape, regardless of the component geometry or how it is loaded.

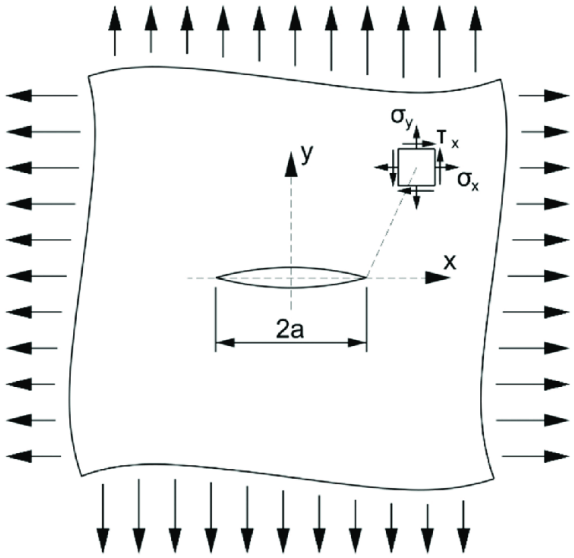


Figure 2.8: Polar coordinate system (r, θ) at the crack tip [2].

Using the polar coordinates in Figure 2.8, the stress components in Mode I can be written in the form:

$$\sigma_{ij}(r,\theta) = \frac{K_I}{\sqrt{2\pi r}} f_{ij}(\theta), \tag{2.4}$$

where $f_{ij}(\theta)$ are known angular functions and K_I is the Mode I stress intensity factor. The full expressions for $f_{ij}(\theta)$ can be found in any standard fracture mechanics textbook [2]. What matters here is the $1/\sqrt{r}$ singularity and the fact that a single scalar parameter, K_I, sets the amplitude of the entire field. Two cracked components with the same K_I have the same stress state near the tip,

even if the geometries and loads are completely different. This is what makes K_I a useful design parameter.

For a real component, K_I is normally written as

$$K_I = Y\,\sigma\sqrt{\pi a}, \tag{2.5}$$

where σ is the remote applied stress, a the crack length, and Y a dimensionless geometry factor that accounts for the finite size of the component, the crack shape, and the loading configuration [2]. For a through crack of length $2a$ in an infinite plate under uniform tension, $Y = 1$. For laboratory specimens and real geometries, Y is tabulated in handbooks or comes from finite element solutions. The component fails when K_I reaches the material's fracture toughness K_{Ic}.

2.3.3.1 Stress intensity factor for the SENB geometry

The fracture toughness tests in this work use single edge notched bend (SENB) specimens loaded in three-point bending, following ASTM E1820 [9]. For this geometry, the standard gives the stress intensity factor as

$$K_I = \frac{P\,S}{B\,W^{3/2}}\,f\!\left(\frac{a}{W}\right), \tag{2.6}$$

where P is the applied force, S the span between the lower supports, B the specimen thickness, W the specimen width, and a the crack length. The function $f(a/W)$ is a polynomial that depends only on the normalised crack length:

$$\begin{aligned} f\!\left(\tfrac{a}{W}\right) = {} & \frac{3\sqrt{a/W}}{2\,(1+2a/W)\,(1-a/W)^{3/2}} \\ & \times\left[1.99 - \tfrac{a}{W}\left(1-\tfrac{a}{W}\right)\left(2.15 - 3.93\,\tfrac{a}{W} + 2.7\,(\tfrac{a}{W})^2\right)\right]. \end{aligned} \tag{2.7}$$

Equation (2.6) is the expression used to compute K_I from the force histories measured in the SHPB three-point bending tests described in Chapter 3. The function $f(a/W)$ is also the starting point for the elastic-plastic analysis based on the J-integral, since the elastic part of J relates directly to K_I through the relations introduced in Section 2.3.5.2.

2.3.4 Linear Elastic versus Elastic Plastic Fracture Mechanics

Linear elastic fracture mechanics (LEFM) is built on the stress intensity factor K_I and the energy release rate G. It assumes that the material behaves linearly across the whole component and that the $1/\sqrt{r}$ singularity describes the crack tip correctly. In real metals this is only true if the plastic zone that forms at the tip stays much smaller than the component itself.

The condition for this to hold is known as small-scale yielding. Irwin [37] estimated the plastic zone radius ahead of the crack tip in plane stress as

$$r_y = \frac{1}{2\pi}\left(\frac{K_I}{\sigma_{YS}}\right)^2. \tag{2.8}$$

For LEFM to remain valid, the characteristic dimensions of the specimen, illustrated in Figure 2.9, (the crack length a, the thickness b, and the uncracked ligament $b-a$) must be at least four times the plastic zone diameter. This gives the dimensional criterion:

$$a,\, b-a,\, h \geq \frac{4}{\pi}\left(\frac{K_I}{\sigma_{YS}}\right)^2. \tag{2.9}$$

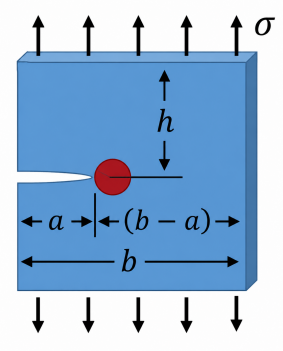


Figure 2.9: Fracture toughness specimen showing the characteristic dimensions a, $b-a$, and h. The same dimensional criterion applies to other standard geometries, including the SENB used in this work [14].

This gives a physical estimate of small-scale yielding. For laboratory K_{Ic} testing, ASTM E399 adopts a more conservative form of the same requirement, $a, B, (W-a) \geq 2.5\,(K_{Ic}/\sigma_{YS})^2$, as reported in Section 2.2.2.2, which also ensures plane-strain conditions along the crack front. This is the criterion used in this work.

Whether this condition is satisfied depends on the combination of yield strength, fracture toughness, and specimen size. For moderate-strength, tough alloys such as AA2024, satisfying it requires specimens that are considerably thicker than what is practical in many laboratory and structural applications. When the condition is not met, the plastic zone at the crack tip is no longer small compared to the specimen dimensions. The elastic field around the tip becomes distorted and K_I on its own stops being a meaningful description of the fracture process.

When this happens, the analysis has to move to elastic plastic fracture mechanics (EPFM), where the parameter that drives crack extension accounts for the plastic work dissipated at the tip. The two parameters used for this purpose are the crack tip opening displacement (CTOD), introduced by Wells [66], and the J-integral, formulated by Rice [55]. Both are developed in the next section. The experimental campaign in this work follows the EPFM route and uses the J-integral to characterise the resistance of AA2024 to crack propagation under dynamic loading.

2.3.5 Elastic Plastic Fracture Mechanics Parameters

Two parameters are used in elastic-plastic fracture mechanics: the crack tip opening displacement (CTOD) and the J-integral. This work uses J, but CTOD is covered first because the two are related and both appear in the ASTM E1820 framework.

2.3.5.1 Crack Tip Opening Displacement

The crack tip opening displacement was proposed by Wells [66] in 1961, after he observed during fracture tests on structural steels that the crack faces in ductile materials separate and the originally sharp crack tip blunts before the crack starts to grow. The amount of opening at the original crack tip, denoted δ, reflects the plastic deformation in the fracture process zone, and can be used as a fracture parameter in its own right.

Two analytical models give explicit expressions for δ. Irwin [37] obtained one by treating the plastic zone as an effective extension of the crack and computing the elastic displacement at the original tip, which leads to

$$\delta = \frac{4}{\pi} \frac{K_I^2}{E\,\sigma_{YS}}. \tag{2.10}$$

Dugdale [24] arrived at a different expression using a strip yield model in which the plastic zone is replaced by a cohesive region of length ρ ahead of the crack, loaded to the yield stress. The Dugdale solution is

$$\delta = \frac{8\,\sigma_{YS}\,a}{\pi E} \ln\left[\sec\left(\frac{\pi\sigma}{2\sigma_{YS}}\right)\right], \tag{2.11}$$

which, in the limit of small-scale yielding ($\sigma \ll \sigma_{YS}$), reduces to

$$\delta = \frac{K_I^2}{E\,\sigma_{YS}} = \frac{G}{\sigma_{YS}}. \tag{2.12}$$

Both models therefore link the crack tip opening to the energetic and stress-based parameters G and K_I, differing only in the proportionality constant. Full derivations are given by Anderson [2].

2.3.5.2 The J-Integral

The J-integral was introduced by Rice [55] in 1968 as a way of characterising the stress and strain field around a crack in a non-linear elastic material. The mathematical idea has older roots: it builds on the energy momentum tensors developed earlier by Eshelby [25] for elastic singularities. Rice's contribution was to show that, for a crack in a two-dimensional body, a particular line integral around the tip has a value that depends only on the crack itself, not on the contour chosen to evaluate it.

For a contour Γ that starts on the lower crack face, encloses the tip, and ends on the upper crack face (Figure 2.10), the J-integral is defined as

$$J = \int_\Gamma \left(W\,dy - T_i \frac{\partial u_i}{\partial x}\,ds \right), \tag{2.13}$$

where W is the strain energy density, $T_i = \sigma_{ij} n_j$ is the traction vector on the contour, n_j the outward unit normal, u_i the displacement components, and ds an increment of arc length.

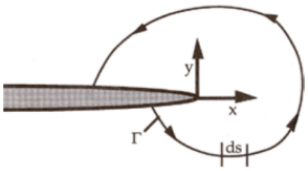


Figure 2.10: Contour path Γ around a crack tip used to evaluate the J-integral [2].

Two properties of J make it useful for fracture mechanics. The first is path independence. Rice showed that the value of J does not depend on the contour chosen, as long as the contour starts and ends on the crack faces and encloses the tip without crossing any other singularities. In practice this means J can be evaluated far from the heavily distorted region around the tip, which is what makes the parameter usable both in finite element analysis and in experimental data reduction. There is a caveat worth stating. Rice's proof of path independence assumes non-linear elastic behaviour, where loading and unloading follow the same stress-strain curve. Real metals do not work this way. Once they yield, unloading takes a different path. The integral is therefore path-independent only under deformation theory of plasticity, not under incremental plasticity with unloading [2]. In practice the two coincide as long as the loading is proportional and monotonic, with no unloading cycles. A fracture test loaded to failure satisfies this, and so do the SENB tests in this work.

The second property is its physical meaning. For a non-linear elastic material, J is the rate at which energy is released as the crack extends, that is, a generalisation of G to the elastic-plastic regime. In the linear elastic limit, J reduces exactly to G, and the relationship to K_I becomes

$$J = G = \frac{K_I^2}{E'}, \tag{2.14}$$

where $E' = E$ in plane stress and $E' = E/(1-\nu^2)$ in plane strain. This identity is the bridge between LEFM and EPFM and is used later in this work to compute the elastic part of J from the measured force histories.

The justification for using J as a single fracture parameter in elastic-plastic materials goes beyond the energy interpretation. Hutchinson [34] and Rice and Rosengren [56] showed independently that, for a material with power-law hardening, the stress and strain fields very close to the crack tip have a singular form whose amplitude is set by J. The stress varies as $r^{-1/(n+1)}$, where n is the power-law hardening exponent. When $n \to \infty$, which corresponds to a non-hardening linear elastic material, this reduces to the $1/\sqrt{r}$ singularity of LEFM. This is known as HRR field, after Hutchinson [34] and Rice and Rosengren [56]. What it means in practice is that J controls the entire stress state near the tip, just as K_I does in the elastic case. J characterises the crack-tip field with a single parameter and acts as the crack driving force. It increases with the applied load and depends on the specimen geometry. The crack starts to grow when J reaches a critical value, J_{Ic}. J is measured during the test, and J_{Ic} is the material property extracted from it. The distinction is the same one that separates K_I from K_{Ic} in LEFM.

2.3.5.3 Experimental evaluation according to ASTM E1820.

For laboratory tests on standard specimens, J is not computed from the contour integral directly. ASTM E1820 [9] prescribes a practical method based on the measured force-displacement record. The total J is split into an elastic and a plastic contribution:

$$J = J_{el} + J_{pl}. \tag{2.15}$$

The elastic part is obtained from the stress intensity factor at the same load level using the LEFM relation

$$J_{el} = \frac{K_I^2(1-\nu^2)}{E}, \tag{2.16}$$

where K_I is computed from an expression that depends on the specimen type. For SENB, it is the polynomial $f(a/W)$ given in Section 2.3.3.1.

The plastic part comes from the area under the force-displacement curve once the elastic contribution has been removed. For a single-edge notched bend specimen with a stationary crack, the standard expression is

$$J_{pl} = \frac{\eta_{pl} A_{pl}}{B_N (W - a_0)}, \tag{2.17}$$

where A_{pl} is the plastic area under the force-displacement record, B_N is the net specimen thickness, and $W - a_0$ is the initial uncracked ligament. The factor η_{pl} depends on the displacement from which A_{pl} is computed. For the load-line displacement, ASTM E1820 gives $\eta_{pl} = 1.9$. When A_{pl} is computed from the force versus crack-mouth opening displacement record, as is the case in this work, the standard gives instead

$$\eta_{pl} = 3.667 - 2.199\,(a/W) + 0.437\,(a/W)^2. \tag{2.18}$$

The CMOD-based form is used here because the crack-mouth opening is the displacement measured by DIC in both loading regimes.

Equation (2.17) holds while the crack is stationary. Once the crack grows, the ligament shrinks and part of the plastic area no longer contributes to driving the current crack tip, so the standard replaces the single evaluation by an incremental one, defined in Annex A9. The record is divided into steps, one per measurement point, and the plastic term is updated from step $i-1$ to step i as

$$J_{pl(i)} = \left[J_{pl(i-1)} + \frac{\eta_{pl(i-1)}}{b_{(i-1)}} \frac{A_{pl(i)} - A_{pl(i-1)}}{B_N} \right] \left[1 - \gamma_{(i-1)} \frac{a_{(i)} - a_{(i-1)}}{b_{(i-1)}} \right], \tag{2.19}$$

where $b_{(i)} = W - a_{(i)}$ is the current ligament, $A_{pl(i)} - A_{pl(i-1)}$ is the plastic area accumulated over the step, and $\eta_{pl(i-1)}$ is Equation (2.18) evaluated at the current crack length. The factor $\gamma_{(i-1)}$ corrects for crack growth and, for the CMOD-based evaluation of the SENB geometry, is given by

$$\gamma_{(i-1)} = 0.131 + 2.131\,(a_{(i-1)}/W) - 1.465\,(a_{(i-1)}/W)^2. \tag{2.20}$$

The elastic part is computed at each step from Equation (2.16) with K_I evaluated at the current crack length $a_{(i)}$, and the total at each step is $J_{(i)} = J_{el(i)} + J_{pl(i)}$. This incremental formulation is the one used to build the J-R curves of this work, in both loading regimes; the crack length $a_{(i)}$ at each step comes from the DIC measurement described in Chapter 3.

The validity of J as a fracture parameter is itself subject to size requirements. ASTM E1820 requires that the uncracked ligament and the specimen thickness satisfy

$$B,\ (W - a_0)\ \geq\ \frac{10J}{\sigma_Y}, \tag{2.21}$$

where σ_Y is the effective yield strength, taken as the average of yield and ultimate strength. This condition is the EPFM analogue of the small-scale yielding criterion in LEFM. It defines the maximum value of J that can be considered valid for a given specimen size, and has to be checked against the measured J values reported in this work.

2.3.6 Stress Triaxiality and Constraint at the Crack Tip

Ductile fracture in metals proceeds through three stages: voids nucleate at inclusions or second-phase particles, grow under plastic deformation, and eventually coalesce into a macroscopic crack. In AA2024 the nucleation sites are the coarse intermetallic particles described in Section 2.2.1.1, which crack or debond from the matrix once the local plastic strain becomes high enough.

Although the process is driven by plastic strain, the rate at which the voids grow depends strongly on the local stress state. Rice and Tracey [57] showed analytically that the volumetric growth of a spherical void in a plastic field is an exponential function of the stress triaxiality, defined as the ratio between the hydrostatic (mean) stress σ_m and the von Mises equivalent stress σ_e:

$$T = \frac{\sigma_m}{\sigma_e}. \tag{2.22}$$

The same exponential dependence is at the core of the porous plasticity model later developed by Gurson [33] and its many extensions. Small changes in triaxiality therefore translate into large changes in the effective ductility of the material at the crack tip.

In a cracked component, triaxiality is set by the geometric constraint imposed on the material ahead of the crack. The geometry of the specimen controls how freely the material can flow plastically. In low-constraint configurations such as a centre-cracked panel loaded in tension, the material can contract laterally and the triaxiality drops as the applied J increases. In high-constraint configurations such as a deeply notched bend specimen, lateral contraction is suppressed and the triaxiality stays high even when the plastic zone has spread well beyond the crack tip [1].

This matters because the relationship between the energetic and kinematic descriptions of the crack tip depends on the constraint level. In small-scale yielding, J and δ are linked by

$$J = m\,\sigma_{YS}\,\delta, \tag{2.23}$$

where m is a dimensionless factor that depends on the local triaxiality and on the strain hardening behaviour of the material. Anderson [1] showed that in configurations that lose constraint under large-scale yielding this single-parameter relationship breaks down: J rises disproportionately relative to δ, and the fracture resistance becomes geometry dependent.

This is the main reason for choosing the SENB geometry in this work. A deeply notched three-point bend specimen keeps the material at the crack tip under high triaxiality even when the plastic zone is large, and high triaxiality matters for two related reasons. The first is theoretical. The HRR field that justifies J as a single-parameter description of the crack tip is derived assuming high constraint [34, 56], so the measured J only corresponds to the theoretical field when the triaxiality is preserved. Without it, the same value of J in two different specimens describes two different stress states and the parameter loses its meaning as a unique fracture criterion [1, 2]. The second reason is practical. A J_{Ic} measured under high constraint represents a lower bound of the material toughness, which is conservative and transferable: a structural component made of the same alloy will have at least that much resistance to crack growth, regardless of its own geometry [2, 9]. Values measured under low constraint give artificially high toughness numbers that are specific to the test geometry and cannot be safely extrapolated to design situations. The deeply notched SENB geometry used in this work was chosen precisely to satisfy both requirements: it preserves J as a meaningful parameter and delivers a conservative estimate of the fracture resistance of AA2024 under dynamic loading.

2.3.7 J-Resistance Curves

In linear elastic fracture mechanics, crack propagation is treated as a single event: once K_I reaches K_{Ic}, the crack runs unstably and the component fails. Ductile metals do not behave this way. After the crack starts to grow, the material continues to resist further extension through plastic deformation at the tip, and the load required to drive the crack keeps rising. This process, known as stable ductile tearing, has to be characterised as a curve rather than a single critical value. Plotting the applied J against the crack extension Δa gives the J-resistance curve, or J-R curve [2].

The first part of the curve does not reflect real crack growth. What looks like an extension of the fatigue pre-crack is actually plastic stretching of the crack tip, which blunts as the load increases. ASTM E1820 [9] describes this stage with the blunting line

$$J = 2\,\sigma_Y\,\Delta a, \tag{2.24}$$

where σ_Y is the effective yield strength, taken as the average of yield and ultimate tensile strength. Once the blunting limit is reached, true tearing begins through the void nucleation and coalescence mechanism described in Section 2.3.6, and the curve enters the tearing regime. In this region, the experimental points are fitted by a power law of the form

$$J = C_1\,(\Delta a)^{C_2}, \tag{2.25}$$

where C_1 and C_2 are constants determined from the regression.

The transition from blunting to physical tearing is gradual and hard to identify directly from the data. ASTM E1820 resolves this by defining J_{Ic} operationally, as the intersection between the power-law regression and a line parallel to the blunting line offset by 0.2 mm of crack extension (Figure 2.11). J_{Ic} is therefore not the exact physical onset of tearing, but a reproducible, conventional measure of the toughness at initiation. The value obtained from this intersection is first taken as a provisional toughness J_Q. It is only accepted as J_{Ic} once the specimen meets the size and qualification requirements of the standard; if any of these fails, the value remains J_Q and does not qualify as a size-independent material property.

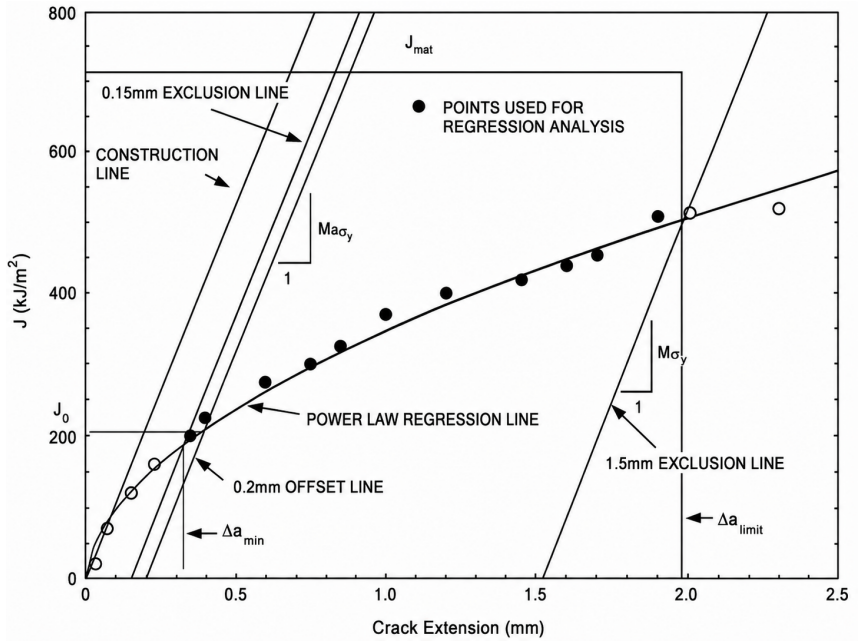


Figure 2.11: Typical J-R curve showing the blunting line, the 0.2 mm offset line, the tearing data, and the construction of the initiation toughness J_{Ic} [2].

2.3.7.1 Validity limits

The standard imposes restrictions on which experimental points can be used in the regression and on the maximum value of J_{Ic} that can be considered representative of the material. Two exclusion lines are drawn parallel to the blunting line, at 0.15 mm and 1.5 mm of crack extension. Only the points falling between these two lines are kept for the power-law fit. Above the 1.5 mm exclusion line, the crack extension is too large for the small-scale assumptions to hold; below the 0.15 mm line, the data is dominated by blunting rather than real tearing.

The validity of the resulting J_{Ic} also depends on specimen size. It must satisfy the same size requirement given in Equation 2.21, now applied to J_{Ic}. If the condition is not met, the reported value is denoted J_Q, a provisional toughness, and cannot be used as a transferable material property.

2.3.7.2 Experimental construction of the curve

Two methods are commonly used to generate the points of the J-R curve. The multiple-specimen method tests several nominally identical specimens loaded to different levels of crack extension, each one heat-tinted or fatigued at the end of the test to measure Δa on the fracture surface. Each specimen provides a single $(J, \Delta a)$ point. The single-specimen method extracts the entire curve from one test by repeatedly unloading and reloading the specimen during loading, measuring the elastic compliance after each unloading, and inferring the current crack length from the change in compliance. This is the unloading compliance technique.

The procedures described above are defined for quasi-static loading. Their adaptation to high strain rate testing in the Split Hopkinson Pressure Bar requires specific changes to the data acquisition and to the way the crack length is tracked, which are addressed in Chapter 3.

2.4 Mechanical Behaviour of Aluminium Alloys at High Strain Rates

During a vehicle crash, the structural components of a battery enclosure are loaded in milliseconds, and the local strain rate at the crack tip can easily reach 10^3–10^4 s^{-1} [47, 64]. Metals do not respond to this kind of loading in the same way they respond to a quasi-static tensile test [17, 68]. The effective yield strength changes, the temperature rises locally because the deformation is too fast for the heat to escape, and both effects act on the same material at the same time. Any reliable characterisation of the fracture toughness of an aluminium alloy for crashworthiness has to take this into account. This section reviews the two main physical effects that govern the dynamic response of aluminium alloys: strain rate sensitivity and adiabatic heating. Their consequences on fracture toughness are discussed in Section 2.4.3.

2.4.1 Strain Rate Sensitivity

When an aluminium alloy is deformed faster, its yield and ultimate tensile strengths rise. This is the basic definition of strain rate sensitivity, and it is commonly observed in the alloys used in automotive applications [64, 68]. The magnitude of the effect, however, is small compared to what is seen in steels. Between quasi-static rates ($\sim 10^{-3}$ s^{-1}) and dynamic rates ($\sim 10^{3}$ s^{-1}), the yield strength of a typical aluminium alloy increases by roughly 5 to 15 %, while for advanced high-strength steels the increase can be 30 to 50 % or more [68].

The reason for this difference lies in how dislocations move through the crystal lattice of each material. In body-centred cubic metals such as ferritic steels, dislocation motion at low temperatures is limited by the Peierls-Nabarro stress, a lattice-friction effect that is thermally activated and therefore rate-dependent. In face-centred cubic metals such as aluminium, the Peierls stress is much lower, and dislocation motion is primarily controlled by interactions with other dislocations and with obstacles in the microstructure, a mechanism that is far less sensitive to the loading rate. A detailed treatment of these mechanisms and their implications for constitutive modelling is

given by Meyers [43]. This physical picture is consistent with the low rate sensitivity parameters typically calibrated for aluminium alloys in phenomenological models such as Johnson-Cook.

For the purposes of this work, the practical consequence is that the effective yield strength of AA2024 under dynamic loading cannot be assumed to be the same as under quasi-static conditions, but the difference is moderate. It matters for an accurate fracture toughness measurement, one of the reasons for the dynamic tests in later chapters, but it does not dominate the response as it can in some steels.

2.4.2 Adiabatic Heating and Thermal Softening

The second effect pulls in the opposite direction. When a metal is deformed, most of the plastic work is converted into heat. The fraction of plastic work that becomes heat is usually denoted β and is known as the Taylor-Quinney coefficient; for aluminium alloys it is typically around 0.9 [62]. Under quasi-static conditions, this heat has time to diffuse into the surrounding material and the temperature rise is negligible. Under dynamic conditions the deformation is too fast for thermal diffusion, and the process becomes essentially adiabatic [17, 47].

The temperature rise in an adiabatic process can be estimated from the plastic work per unit volume as

$$\Delta T = \frac{\beta}{\rho\, c_p} \int_0^{\varepsilon_p} \sigma \, d\varepsilon_p, \tag{2.26}$$

where ρ is the density, c_p the specific heat, and the integral is the plastic work density. For AA2024 with $\rho \approx 2780$ kg/m^3, $c_p \approx 880$ J/(kg·K), and a flow stress around 450 MPa acting through a plastic strain of 0.1, this gives $\Delta T \approx 17$ °C. At larger strains and higher stress levels, as typically occur near the crack tip, the local temperature rise can easily reach 50–100 °C, and values above 200 °C have been reported in severe deformation localisation bands [47].

This heating reduces the flow stress of the material locally, which is known as thermal softening. In practice, dynamic deformation of an aluminium alloy therefore involves two competing effects: strain rate hardening, which tends to raise the flow stress, and thermal softening, which tends to lower it. The net effect depends on the specific alloy, the strain level, and how effectively heat can be conducted away from the deformation zone.

When thermal softening dominates locally, the deformation becomes unstable and concentrates into narrow bands of highly distorted material known as adiabatic shear bands. These bands are typically a few tens of micrometres wide, and the temperature inside them can be several hundred degrees above the surrounding material [47]. In ductile metals, adiabatic shear bands often act as preferential sites for void nucleation and coalescence, and can become the paths along which dynamic fracture propagates. For the present work, the presence of these bands at the crack tip under high strain rate loading is one of the reasons why the fracture toughness of an aluminium alloy measured under dynamic conditions can differ from the quasi-static value [17, 68].

2.4.3 Effects of Strain Rate on Fracture Toughness

The two effects previously described, strain rate hardening and adiabatic thermal softening, act on the same material at the same time, and their combined influence on the fracture toughness of aluminium alloys is not straightforward. The flow stress rises with rate, which increases the elastic energy available to drive a crack and tends to raise the measured toughness. At the same time, the temperature rise near the crack tip softens the material locally, which can either facilitate crack tip blunting and raise the toughness further, or promote strain localisation and adiabatic shear bands and lower it. Which effect dominates depends on the specific alloy, its temper, the crack tip constraint, and the strain rate range considered [43].

The experimental evidence for aluminium alloys under dynamic loading is limited and sometimes contradictory. Xing et al. [70] measured the dynamic fracture toughness of AA2024 using three-point bending and reported an increase in the apparent toughness with loading rate, although the strain rates achieved with their drop-tower setup remained well below those reached in the Split Hopkinson Pressure Bar. Rubio et al. [58] used a modified SHPB to test aluminium alloys in three-point bending at higher rates and showed that high-speed optical measurements of the crack mouth opening displacement are essential for reliable toughness determination under dynamic conditions, because the event duration is too short for conventional instrumentation. More recently, Pandouria and Tiwari [51] combined dynamic testing with digital image correlation on AA2014-T6 and highlighted the sensitivity of the measured toughness to the method used for tracking crack initiation.

Taken together, these studies point to two conclusions. The first is that the fracture toughness of aluminium alloys is not rate-independent, and quasi-static data cannot be used directly for crashworthiness assessment. The second is that reliable measurements at high strain rates require experimental techniques specifically adapted for the short duration of the event, including high-speed imaging and direct tracking of the crack tip. This is the motivation for the experimental methodology developed in this thesis, which combines a modified SHPB in three-point bending with high-speed DIC to resolve the crack tip response of AA2024 during dynamic loading.

2.5 Constitutive Modelling of the Dynamic Response

The rate hardening and thermal softening of Section 2.4 act together during a dynamic event, and representing their combined effect in an impact simulation requires a constitutive model. The standard choice for metals is the Johnson-Cook model, which is also the framework in which dynamic test data are reported and crashworthiness models calibrated. Seeing how it separates the two competing effects clarifies the response measured in this work, and the dynamic fracture data obtained here are the kind of input such models need.

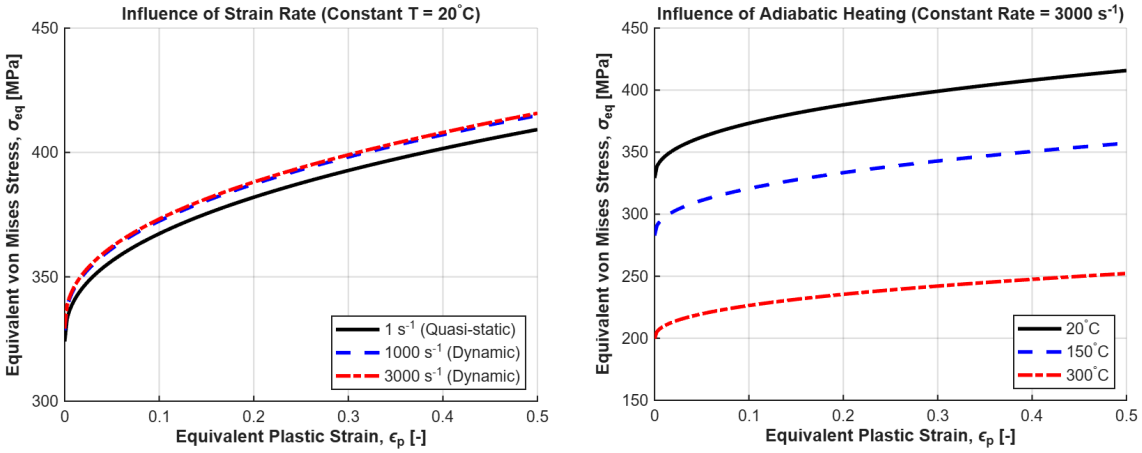
The Johnson-Cook model [38] is the phenomenological law most commonly used to describe the dynamic plastic response of metals. It is empirical, numerically simple, and available in every

major explicit finite element software. The equivalent flow stress is the product of three multiplicative terms:

$$\sigma_{eq} = \left(A + B\,\varepsilon_p^{n}\right)\left(1 + C\ln\dot{\varepsilon}^{*}\right)\left(1 - T^{*m}\right). \tag{2.27}$$

The first bracket is the quasi-static strain hardening response, with A the yield stress, B the hardening modulus, ε_p the equivalent plastic strain, and n the hardening exponent. The second bracket introduces strain rate sensitivity through the rate constant C and the dimensionless strain rate $\dot{\varepsilon}^{*} = \dot{\varepsilon}/\dot{\varepsilon}_0$, where $\dot{\varepsilon}_0$ is a reference quasi-static rate. The third bracket accounts for thermal softening through the softening exponent m and the homologous temperature T^{*}, which normalises the current temperature between room temperature and the melting point. The three terms are independent. This keeps the calibration simple, but it also means the model cannot capture any coupling between rate and temperature.

The rate and temperature terms can be evaluated separately to show their isolated influence. Using the Lesuer et al. parameters for 6061-T6 aluminium [42] ($A = 324$ MPa, $B = 114$ MPa, $n = 0.42$, $C = 0.002$, $m = 1.34$), the curves of Figure 2.12 were computed. Raising the strain rate from quasi-static to 3000 s^{-1} lifts the flow stress uniformly across the strain range (Figure 2.12a). The shift is modest, consistent with the small C typical of aluminium alloys; structural steels, with C between 0.01 and 0.05 [38], would show a much wider separation between rates. The temperature term acts in the opposite direction (Figure 2.12b): the flow stress falls as the temperature climbs towards the melting point, mirroring the softening mechanism of Section 2.4.2.



(a) Effect of dynamic strain rates at 20°C.

(b) Effect of temperature at 3000 s^{-1}.

Figure 2.12: Analytical flow stress curves for the 6061-T6 aluminium alloy using the Johnson-Cook parameters [38], showing the isolated effects of strain rate hardening and thermal softening.

Calibrating the five parameters requires quasi-static tensile tests, dynamic tests at several strain rates, and ideally tests at elevated temperature. For AA2024, several sets of Johnson-Cook parameters are available in the literature, but the values depend on the temper, the range of strain rates tested, and the calibration procedure, which limits their direct transferability to new experimental campaigns. Reliable dynamic data on the actual material, of the kind measured in this work, are

what such a calibration needs.

2.6 Dynamic Experimental Techniques

Conventional testing machines cannot resolve events that last only a few hundred microseconds because of the inertia of the load frame and the limited response of the load cells. Dynamic characterisation therefore relies on wave-propagation methods, of which the Split Hopkinson Pressure Bar is the standard example. This section reviews the SHPB technique in its classical compression form and in the three-point bending configuration used for fracture testing, and the Digital Image Correlation method used to resolve the specimen deformation during the dynamic event.

2.6.1 The Split Hopkinson Pressure Bar (SHPB)

The Split Hopkinson Pressure Bar, first proposed by Hopkinson in 1914 and developed into its modern two-bar form by Kolsky [40] in 1949, is the standard apparatus for measuring the mechanical response of materials at strain rates between 10^2 and 10^4 s^{-1}. A description of the method and its many variants is given by Chen and Song [16].

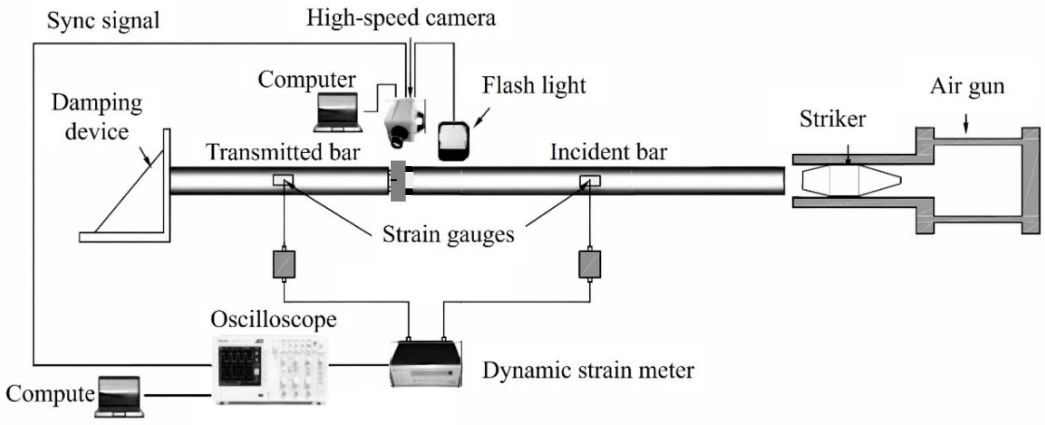


Figure 2.13: Schematic of the Split Hopkinson Pressure Bar, showing the bars, strain gauges, data acquisition system, and the synchronised high-speed imaging setup used for Digital Image Correlation. Adapted from [73].

The apparatus relies on one-dimensional elastic wave propagation in long, slender bars. A striker, launched by a gas gun, impacts the incident bar and generates a compressive elastic wave that travels along its length. When this incident wave $\varepsilon_I(t)$ reaches the specimen, part of it is reflected back into the incident bar as $\varepsilon_R(t)$ and the rest is transmitted through the specimen into the transmitted bar as $\varepsilon_T(t)$. The partition between reflected and transmitted waves is governed by the impedance mismatch between the bars and the specimen. Strain gauges mounted at fixed positions on both bars record the three pulses as a function of time, and the signals are sampled at rates of at least 1 MHz to resolve the microsecond-scale events.

For the classical compression test, and assuming the specimen deforms uniformly and reaches dynamic stress equilibrium, the engineering strain rate, strain, and stress in the specimen can be derived from the reflected and transmitted waves through Kolsky's one-dimensional analysis [16]:

$$\dot{\varepsilon}(t) = -\frac{2C_0}{L_s}\,\varepsilon_R(t), \tag{2.28}$$

$$\varepsilon(t) = -\frac{2C_0}{L_s}\int_0^t \varepsilon_R(\tau)\,d\tau, \tag{2.29}$$

$$\sigma(t) = \frac{A_b E_b}{A_s}\,\varepsilon_T(t), \tag{2.30}$$

where $C_0 = \sqrt{E_b/\rho_b}$ is the elastic wave speed in the bar material, L_s is the initial specimen length, A_b and A_s are the cross-sectional areas of the bars and the specimen, and E_b is the Young's modulus of the bars.

Two conditions have to be met for this analysis to be valid. The first is that the specimen deforms uniformly along its length, which requires the specimen to be short compared to the wavelength of the incident pulse. The second is dynamic stress equilibrium, meaning that the forces on the two faces of the specimen are approximately equal throughout the event. Equilibrium is not instantaneous: it takes several wave reflections within the specimen to develop, and any analysis applied to signals from before equilibrium is reached gives incorrect results. In practice, a pulse shaper, typically a small disk of ductile material placed between the striker and the incident bar, is used to lengthen and smooth the incident pulse. This gives the specimen enough time to reach equilibrium before the peak load is applied and also filters out high-frequency oscillations that would otherwise contaminate the signals [16].

The classical SHPB previously described was developed for compression testing of cylindrical specimens. The method used in this work applies a modified configuration in which the specimen is a single-edge notched bend (SENB) specimen loaded in three-point bending, with the incident bar striking the centre of the specimen and the transmitted bar acting through the supports. The principle of measurement, based on the waves travelling in the instrumented bars, is the same, but the relationships between the recorded signals and the mechanical quantities of interest (force, displacement, crack tip opening) are different. These adaptations are described in Section 2.6.2.

2.6.2 SHPB Adaptation for Three-Point Bending Fracture Testing

Measuring fracture toughness under dynamic loading requires a different configuration from the classical compression SHPB. Instead of placing the specimen between the incident and transmitted bars, the SENB specimen is supported at both ends on the transmitted bar, and the incident bar strikes the centre of the specimen, applying the central load of a three-point bend test. The striker, incident bar, and transmitted bar still operate through one-dimensional elastic wave propagation, but the quantities extracted from the recorded signals now describe the mechanical response of a bend specimen rather than a specimen in uniaxial compression.

In this configuration, the force applied to the specimen at the central point is related to the sum of the incident and reflected waves in the incident bar:

$$F_1(t) = E_b A_b \left[\varepsilon_I(t) + \varepsilon_R(t)\right], \tag{2.31}$$

and the force transmitted through the two supports is obtained directly from the transmitted bar:

$$F_2(t) = E_b A_b \, \varepsilon_T(t). \tag{2.32}$$

For the classical quasi-static analysis of a three-point bend test to remain applicable, dynamic stress equilibrium has to be satisfied throughout the event, meaning that the force on the loaded face of the specimen must be approximately equal to the force on the supports:

$$F_1(t) \approx F_2(t). \tag{2.33}$$

Before this condition is met, the specimen is in an inertial regime and the force measured at any single location does not represent the actual loading on the cracked ligament. The earliest instant at which equilibrium is reached, typically defined by a tolerance of a few percent between F_1 and F_2, marks the start of the valid analysis window. Everything recorded before that is discarded.

Once equilibrium is established, the load applied to the specimen can be taken directly from the transmitted bar signal,

$$P(t) = E_b A_b \, \varepsilon_T(t), \tag{2.34}$$

which has the practical advantage of filtering out the high-frequency inertial oscillations that contaminate the incident-bar signal during the early stages of the event [16]. As in the compression configuration, a pulse shaper is used to lengthen the incident pulse and reduce the time required to reach dynamic equilibrium.

Applying the quasi-static fracture mechanics framework to a dynamic bend test also requires additional validity checks that are not present in conventional SHPB compression testing. Nakamura, Shih and Freund [46] showed that a quasi-static J formula applies to a dynamically loaded bend specimen only after a characteristic transition time τ, defined as the instant beyond which the kinetic energy of the specimen falls below its deformation energy. Before τ, structural inertia dominates the response and the crack-tip field differs from its quasi-static counterpart; after τ, the two become indistinguishable and the deep-crack J formula holds. They expressed this transition time as

$$t_T = D S \frac{H}{c_0}, \tag{2.35}$$

where H is the specimen width, c_0 the longitudinal bar wave speed of the specimen material, S a dimensionless shape factor that depends on the elastic compliance of the specimen, and D a dimensionless coefficient set by the load-point displacement history. For a standard three-point bend specimen, finite element analysis gives the product $DS \approx 24$, so that $t_T \approx 24\,(H/c_0)$. Crack initiation must occur after this transition time for the ASTM E1820 formulation to be applied

without modification. In addition, the contribution of kinetic energy to the J-integral becomes significant when the crack propagation speed approaches an appreciable fraction of the elastic wave speeds of the material, on the order of the Rayleigh wave speed, which for aluminium alloys is about 2900 m/s [54]. While the crack stays slow relative to this limit, the inertial contribution is small and the quasi-static framework applies. When this is not the case, the inertia of the propagating crack must be accounted for, for which Kishimoto et al. [39] derived a path-independent dynamic J-integral that adds the kinetic-energy term to the conventional contour integral. Even when all these conditions are met, determining the crack length during a dynamic test remains an open problem. The unloading compliance method used in ASTM E1820 quasi-static testing relies on periodic partial unloadings of the specimen to measure the elastic compliance and infer the crack length from it. In an event that lasts only a few hundred microseconds, these unloadings are physically impossible. Alternative approaches have been explored in the literature, including potential drop methods, post-test marker techniques, and optical measurements of the crack mouth opening. The specific method adopted in this work, which uses Digital Image Correlation to track the opening of the notch at two distinct points on the specimen surface, is described in Chapter 3.

2.6.3 Digital Image Correlation

The signals from the strain gauges on the bars give the forces and displacements at the ends of the specimen, but say nothing about what is happening on the specimen surface. Clip gauges, which would normally provide this information in a quasi-static test, cannot be used here. Their response times are far too slow for an event that lasts a few hundred microseconds, and any physical contact with the specimen would disturb the measurement. Digital Image Correlation (DIC) is the standard non-contact alternative and gives access to the full-field displacement of the specimen surface throughout the test [61].

The method works by tracking the motion of small patches of the specimen surface between successive images. A reference image is taken before loading and a sequence of target images is recorded during the test. The surface is prepared with a random, high-contrast speckle pattern, usually applied by spraying black and white paint, so that small regions of the image can be distinguished from each other. For each point of interest, the algorithm defines a square subset of pixels around that point and searches for the subset in the target image that best matches it, using a similarity metric and subpixel interpolation to refine the result [61]. The displacement of the point is given by the offset between the reference and the matched positions, and the strain is obtained by differentiating the displacement field.

In dynamic fracture tests, the quality of the DIC results depends on two practical choices. The first is the imaging setup: the frame rate has to be high enough to capture the event without motion blur, typically 10^5 to 10^6 frames per second for SHPB applications, and the illumination has to provide enough light for the short exposure times this implies. The second is the speckle pattern itself, which must be fine enough to give good spatial resolution but not so fine that the features become smaller than the camera's pixel size.

When the specimen contains a propagating crack, the order in which the correlation processes the points matters. The DIC software used in this work relies on the reliability-guided scheme proposed by Pan [49], adopted by VIC-2D and other implementations [30]. The calculation starts from a seed point and evaluates the quality of each match with the Zero-Mean Normalised Cross Correlation (ZNCC) coefficient. The neighbours of the most reliable computed point are processed next, so the calculation path grows along the directions where the correlation is most trustworthy. This avoids crossing regions of low reliability such as cracks or shadows, where a fixed scanning path would let the error at one point propagate to the points that follow. For dynamic fracture testing, where the crack opening is the region of interest, the algorithm extracts reliable displacement fields on either side of the crack.

2.7 Review of Related Studies and Research Gaps

After reviewing the theoretical background, the dynamic effects, and the experimental techniques relevant to this work, this section looks at what has actually been done in the field of dynamic fracture of aluminium alloys, and where the gaps are that the present work aims to fill.

The fracture toughness of aluminium alloys is well characterised in the quasi-static regime. Standard references such as the ASM Handbook Vol. 19 [6] and the Granta EduPack database [3] compile design values for the most common tempers of the 2xxx, 6xxx, and 7xxx series, with established testing procedures defined by ASTM E399 [10] and E1820 [9]. Under dynamic loading the situation is different. Published data are scarce, scattered across heterogeneous methodologies, and strongly dependent on the specific test setup. There is no consolidated database of dynamic fracture properties for aluminium alloys equivalent to the quasi-static one, and this absence is itself the first relevant gap for crashworthiness modelling.

The earliest attempts to characterise the fracture behaviour of aluminium alloys at high loading rates relied on adaptations of the Hopkinson bar configuration. Yokoyama [72] introduced an impact bend test procedure for measuring the dynamic stress intensity factor at initiation, K_{Id}, in high-strength alloys including AA7075-T6. The loading rates reported in this kind of test, expressed as the rate of change of the stress intensity factor $\dot{K}_I$, are of the order of 10^6 MPa$\sqrt{m}$/s, which corresponds to the SHPB regime in terms of nominal strain rate. The fact that this line of work goes back to the early 1990s and that the field still lacks a unified normative procedure for dynamic J-R curves gives an idea of how difficult the problem is.

For intermediate strain rates, in the range of 10^1 to 10^2 s^{-1}, instrumented drop towers are the typical choice. Xing et al. [70] tested AA2024-T4 and AA7075-T6 in three-point bending and reported both initiation and average propagation toughness values. The limitation here is mechanical: drop towers cannot reach the strain rates involved in real crash events ($> 10^3$ s^{-1}), so the data they produce do not cover the regime that matters for impact applications such as battery enclosures or aerospace structures.

To reach truly dynamic conditions, the contemporary literature relies almost exclusively on the SHPB. Rubio et al. [58] used a modified SHPB in three-point bending on pre-cracked specimens and emphasised that without strict verification of dynamic force equilibrium between the incident and transmitted bars, the use of quasi-static fracture mechanics expressions is not justified. The same expressions that govern K_I for SENB specimens in ASTM E1820, namely $K_I = (PS/BW^{3/2})\, f(a/W)$, can be applied to dynamic tests once equilibrium is reached, but the validity window has to be checked for each test. Pandouria et al. extended this approach in two recent studies, the first on AA2014-T6 [51] and the second on AA6063-T6 [50], in both cases combining SHPB three-point bending with finite element simulation to overcome the difficulties of direct measurement on the specimen. The work on AA6063-T6 is particularly close in scope to what is proposed here, but the authors still report point values of K_{Id} at initiation rather than constructing the full J-R resistance curve. The recurring problem with all of these studies is the same: the standard output of a quasi-static fracture toughness test, which is the elastic-plastic resistance curve over a range of crack extensions, is essentially missing from the dynamic literature.

For AA2024 specifically, dynamic fracture data on pre-cracked specimens are particularly hard to find. The most cited recent work on this alloy under dynamic conditions, by Xue and Wierzbicki [71], characterises the ductile fracture locus of AA2024-T351 using smooth specimens under several stress states, within a damage plasticity framework. It is a rigorous study, but it is methodologically a different problem from the one addressed here: it tracks ductile failure in uncracked geometries, not the propagation of a macroscopic crack through a notched specimen.

Table 2.3 summarises the main experimental studies previously discussed, with the reported toughness values where available, and shows where the present work positions itself.

Table 2.3: Summary of representative experimental studies on dynamic fracture toughness of aluminium alloys.

Reference	**Alloy**	**Method**	**Rate (s^{-1})**	**Geom.**	**Parameter**	**Reported Value**	**Main Limitation**
Yokoyama (1993)	7075-T6	SHPB	$\sim 10^2$	SENB	K_{Id}	≈ 30 MPa$\sqrt{m}$	No J-R curve construction.
Rubio (2003)	7075-T651	Mod. SHPB	10^2–10^3	SENB	K_{Id}	$\approx$ 25–35 MPa$\sqrt{m}$	No J-R curve; focused on initiation.
Xing (2013)	2024-T4 & 7075-T6	Drop tower	$\approx 10^1$	SENB	K_{Id}	$\approx$ 28 & 32 MPa$\sqrt{m}$	Limited strain rates; not applicable to high-velocity crash.
Pandouria (2023a)	2014-T6	SHPB + FEA	10^2–10^3	SENB	K_{Id}	≈ 30 MPa$\sqrt{m}$	No experimental J-R curve.
Pandouria (2023b)	6063-T6	SHPB + FEA	10^2–10^3	SENB	K_{Id}	≈ 28 MPa$\sqrt{m}$	No experimental J-R curve.
Xue (2009)	2024-T351	Multi-stress	Static/Dyn.	Smooth	Fract. locus	—	Different framework; no crack propagation analysis.
Chen (2017)	6082-T6	Tensile + notched	10^{-4}–10^3	Smooth	Fract. locus	—	No pre-cracked specimens; no J-integral measurements.
Present work	**AA2024 & AA6082-T651**	**SHPB+DIC**	—	**SENB**	**J-R (J_{Id})**	**(to be determ.)**	**Complete dynamic J-R curve using adapted ASTM E1820.**

The picture that emerges from this review is that experimental work on dynamic fracture of aluminium alloys has used widely different methodologies. Most studies focus on initiation alone, reporting a single K_{Id} value rather than a full resistance curve. Validity criteria for the measured toughness, whether for plane-strain conditions in LEFM or for specimen size requirements in EPFM, are rarely checked against the actual test data. The normative framework of ASTM E1820, designed for quasi-static loading, is adapted to the SHPB regime on a case-by-case basis, taking into account the validity conditions discussed in Section 2.6.2.

For AA2024, which is one of the most studied aluminium alloys under dynamic loading, no published work constructs complete J-R curves through a procedure consistent with ASTM E1820 adapted to the SHPB. The available data are either limited to K_{Id} at initiation or obtained from smooth specimens within a damage plasticity framework, as in the work of Xue and Wierzbicki [71].

For AA6082-T651 the situation is worse. Chen et al. [17] provide detailed flow and fracture data over a wide range of strain rates and triaxialities, but their specimens are smooth and notched, not pre-cracked. They characterise the ductile fracture locus of the alloy, which is a different problem from measuring the resistance to crack propagation in a notched specimen. No J-integral measurements under dynamic loading have been reported for this alloy. AA6082-T651 is the standard choice for battery enclosure crash frames, yet no such data exist for it under dynamic loading.

The present work addresses both gaps. SENB specimens of AA2024 and AA6082-T651 are tested under quasi-static and dynamic loading using the same geometry, the same SHPB three-point bending configuration, and the same data reduction procedure based on ASTM E1820. The low strain rate sensitivity of AA6082-T6, documented by Chen et al. [17], is also useful from a methodological standpoint: because its dynamic toughness is expected to remain close to the quasi-static value, it provides a built-in check on the reliability of the test setup before rate effects are interpreted as material behaviour.

Chapter 3

Experimental Methodology

3.1 Overview of the Experimental Program

This work measures the resistance of two aluminium alloys, AA2024 and AA6082-T651, to crack propagation under quasi-static and dynamic loading. Both are tested as single-edge notched bend (SENB) specimens in three-point bending, instrumented with Digital Image Correlation (DIC), and reduced to a J-resistance curve following ASTM E1820 [9].

The same specimen geometry, three-point bending configuration, and data-reduction procedure are used for both materials and both loading regimes, as shown in Figure 3.1, so that any difference in the measured toughness reflects the material or the loading rate rather than the method. Section 2.7 showed that the dynamic fracture literature is fragmented across incompatible methods, and that most studies report a single initiation value rather than a full resistance curve. Holding the method fixed removes that source of scatter. Any difference between the quasi-static and the dynamic result can then be assigned to the loading rate rather than to a change in procedure.

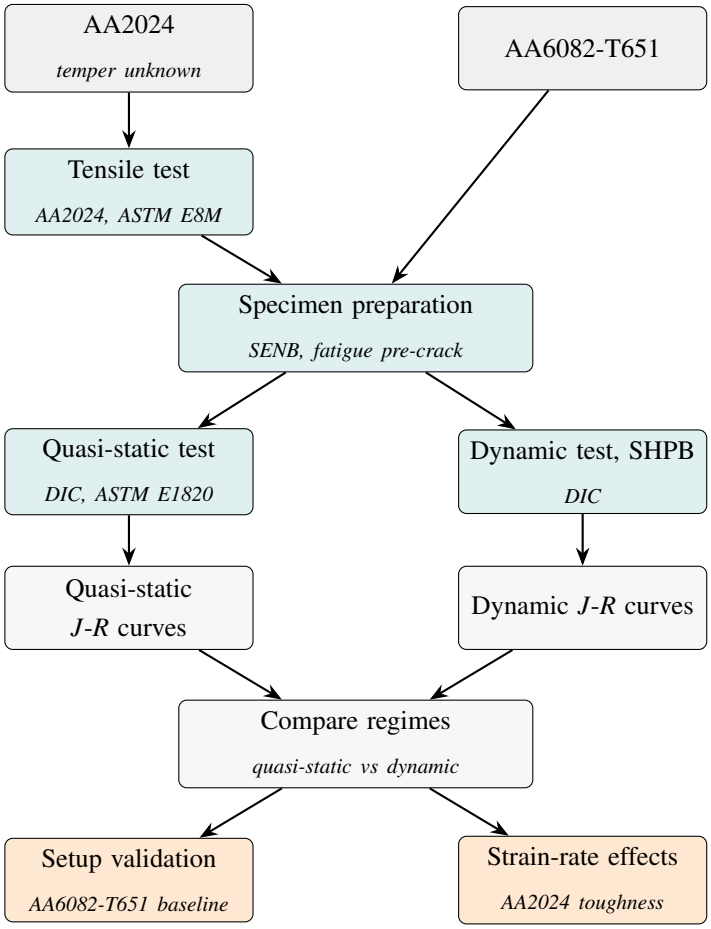


Figure 3.1: Overview of the experimental program. AA2024 is characterised in tension; both alloys are prepared as pre-cracked SENB specimens and tested under quasi-static and dynamic loading. The *J*-*R* curves from the two regimes are compared, validating the setup with AA6082-T651 and isolating the strain-rate effects on AA2024.

AA2024 and AA6082-T651 are tested for different reasons. The first is the alloy of interest for rate effects. Its strain-rate sensitivity is measurable, and the review in Section 2.2.1 found no dynamic fracture data on pre-cracked specimens for this alloy. The supplier did not specify its temper, so its quasi-static strength was measured by the tensile tests of Section 3.5 before any fracture test. AA6082-T651 serves a second purpose. Chen et al. [17] showed that this alloy has low strain-rate sensitivity, so its dynamic toughness should remain close to the quasi-static value. That makes it a reference. If the dynamic setup reproduces the quasi-static toughness of AA6082-T651, the setup is sound, and the rate effects measured on AA2024 can be read as material behaviour rather than as an experimental artefact.

Beyond characterising the material, the quasi-static tests fix the baseline against which the dynamic results are compared and check the data-reduction chain under conditions where conventional instrumentation still applies. The dynamic tests are the objective. They run on a split Hopkinson pressure bar adapted for three-point bending, where the event lasts a few hundred microseconds and no mechanical gauge can follow the load.

The campaign covers tension, quasi-static fracture, and dynamic fracture. Tensile tests were run on the AA2024 alone, to obtain its quasi-static properties, since those of the AA6082-T651 are given by the supplier certificate. Every fracture specimen, quasi-static and dynamic, was fatigue pre-cracked before testing. Table 3.1 lists the specimens.

Table 3.1: Test matrix of the experimental program.

	Tensile	Quasi-static fracture	Dynamic fracture
AA2024	9	4	4
AA6082-T651	–	4	4

3.2 Aluminium Alloys

Two aluminium alloys are studied in this work. AA2024 is the alloy of interest for the strain-rate effects. AA6082-T651 is the reference used to validate the dynamic setup. Their alloying systems, microstructure, and fracture mechanisms are described in Section 2.2. This section reports only the as-received condition of the material used in the experimental campaign.

The AA2024 specimens were supplied by Tornitrofa, having been produced for an earlier project and kept in stock at INEGI. No material certificate was available, so neither the temper nor the batch composition is documented. The alloy is confirmed as AA2024, of the Al–Cu–Mg system, but the temper is unknown. The mechanical properties needed for the fracture toughness calculations were therefore measured directly, through the tensile tests of Section 3.5. With no batch analysis available, the nominal composition of Section 2.2.1.1 is used as representative.

The AA6082-T651 came as a hot-rolled plate of $3020 \times 1520 \times 12$ mm, with an EN 10204-3.1 inspection certificate issued by Status Alumínio. The T651 temper denotes solution heat treatment, stress relief by stretching, and artificial ageing. The certified batch composition is given in Table 3.2 and falls within the EN 573-3 limits for this alloy. The provenance and condition of this material are fully documented, unlike those of the AA2024.

Table 3.2: Chemical composition of the AA6082-T651 batch (wt.%), from the EN 10204-3.1 inspection certificate.

Element	Al	Si	Fe	Cu	Mn	Mg	Cr	Ni	Zn	Ti	Ga
wt.%	Rem.	1.2	0.33	0.09	0.7	1.0	0.12	0.01	0.09	0.03	0.02

The certificate also reports the mechanical properties of the batch, listed in Table 3.3.

Table 3.3: Mechanical properties of the AA6082-T651 batch, from the EN 10204-3.1 inspection certificate.

Property	Value
Tensile strength, R_{m} (MPa)	339
Yield strength, $R_{\mathrm{p0.2}}$ (MPa)	321
Elongation, A_{50} (%)	9.5
Hardness (HB)	107

3.3 Specimen Design and Manufacturing

3.3.1 Geometry and Dimensioning

The fracture tests use single-edge notched bend (SENB) specimens loaded in three-point bending, following ASTM E1820 [9]. The same geometry is used for both alloys and both loading regimes, so that any difference in the measured toughness reflects the material or the loading rate, not a change in specimen design.

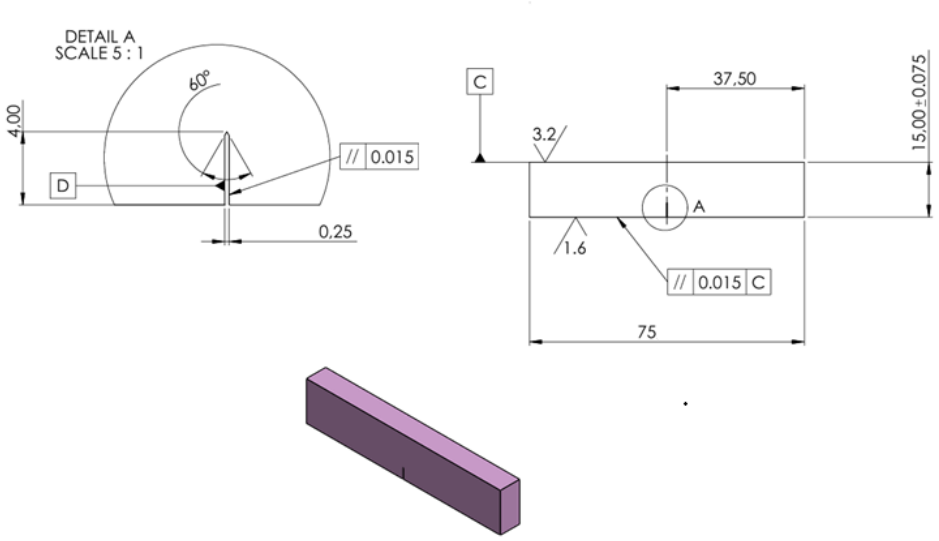


Figure 3.2: SENB specimen geometry and dimensions (mm), showing the machined V-notch before fatigue pre-cracking.

Figure 3.2 gives the specimen dimensions. The width is $W = 15$ mm and the thickness $B = 7.5$ mm, giving $W = 2B$ as required by the standard. The total length is 75 mm and the support span is $S = 60$ mm, equal to $4W$. A V-notch is machined at mid-length, with a 60° flank angle, a depth of 4 mm, and a root radius of 0.25 mm.

The notch alone gives $a/W \approx 0.27$, below the range admitted for a toughness test. The crack is extended to the target $a/W = 0.5$ by a fatigue pre-crack grown from the notch root, described in Section 3.6. The standard admits a/W between 0.45 and 0.70. The pre-crack was aimed at

0.5, and the value reached on each specimen was measured after pre-cracking and used in the individual data reduction. These measured values are reported in Chapter 4.

After pre-cracking, side grooves are machined into both faces along the crack plane, reducing the thickness from $B = 7.5$ mm to a net thickness $B_N = 6.0$ mm, a total reduction of 20%. Without side grooves, the triaxiality varies through the thickness. The interior is confined and stays at high triaxiality, while the free side faces relax towards plane stress and lose triaxiality, in the sense defined in Section 2.3.6. The crack then advances faster at the centre than at the faces and its front curves. The grooves remove the low-triaxiality material at the faces and restore confinement across the full net thickness, so the front stays straight as the crack grows. ASTM E1820 [9] recommends side grooves. A straight front makes the optical crack-length measurement on the specimen surface representative of the average advance through the thickness, since crack growth here is tracked by DIC on the surface. In the data reduction, B_N replaces B in the plastic term of J given in Equation 2.17.

The thickness was set by the available stock rather than chosen to satisfy the plane-strain requirement of linear elastic fracture mechanics. As shown in Section 2.3.4, a valid K_{Ic} measurement in these alloys would need a thicker specimen, . The chosen specimens were 7.5 mm thick. The specimens therefore fall outside the LEFM validity window, and the characterisation follows the elastic-plastic route based on the J-integral. The deep notch and the side grooves together keep the crack tip under high constraint, which preserves J as a single-parameter description of the crack tip field, for the reasons given in Section 2.3.6.

3.3.2 Crack-Plane Orientation

Fracture toughness in wrought aluminium plate is anisotropic. As described in Section 2.2.1.2, rolling aligns the grains and the intermetallic particles with the rolling direction, and the toughness depends on the orientation of the crack plane relative to it. For the same temper, the T-L orientation is typically 10 to 15% lower than L-T as previously documented in Table 2.2.

The orientation of the specimens relative to the rolling direction of the plate was not recorded by the supplier and could not be recovered. The specimen geometry does, however, constrain the possible orientations. The plate is 12 mm thick, which is the short-transverse (S) direction. The specimen width ($W = 15$ mm) and length (75 mm) exceed this thickness, so neither can be aligned with S. The only specimen dimension that fits within the plate thickness is $B = 7.5$ mm. The crack plane and the propagation direction therefore lie in the L–T plane of the plate, which restricts the orientation to either L-T or T-L. Which of the two applies is not known.

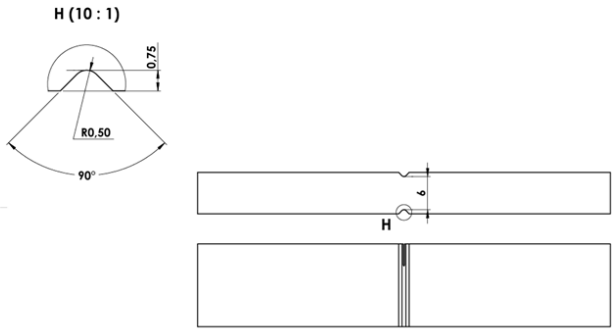
This is a limitation on the absolute toughness values, since L-T and T-L can differ by the 10 to 15% noted above. It does not affect the main objective of this work. The strain-rate effect is measured by comparing the quasi-static and dynamic response of specimens cut the same way from the same stock, so the orientation, whatever it is, is common to both regimes and cancels in the comparison.

3.3.3 Specimen Manufacturing

The specimens were machined by Tornitrofa for both alloys, from the AA2024 already in stock and from the newly acquired AA6082, to the geometry of Figure 3.2. The specimen shape was produced by CNC milling and the V-notch was cut by electrical discharge machining (EDM). They were delivered with the machined notch but without side grooves and without a sharp crack. The fatigue pre-crack and the side grooves were introduced afterwards at INEGI, in that order.

The fatigue pre-crack is grown from the notch root on the full-thickness specimen, before any side groove is cut, by the procedure of Section 3.6. ASTM E1820 specifies this order so that the fatigue crack front grows nearly straight. Cutting the grooves into a flat specimen first would leave a less uniform pre-crack front.

The side grooves were then cut by electrical discharge at INEGI. The groove profile, with a 90° included angle, a 0.50 mm root radius, and 0.75 mm depth per face, is shown in Figure 3.3. EDM was used because it cuts the groove without imposing mechanical load on the pre-cracked specimen and holds the profile and alignment with the crack plane to close tolerance.



(a)



(b)

Figure 3.3: Side groove geometry. (a) groove profile (90° angle, 0.50 mm root radius, 0.75 mm depth per face); (b) machined specimen after EDM grooving.

3.4 Digital Image Correlation Methodology

3.4.1 Speckle Pattern Design

Digital image correlation tracks the motion of a random speckle pattern applied to the specimen surface. The correlation works on subsets of pixels, so the speckle size has to match the imaging resolution. A common rule is that each speckle should span 3 to 5 pixels. Smaller features fall below the resolution of the camera and cannot be resolved, while larger ones reduce the spatial density of the pattern and coarsen the measurement.

The speckle size in object space follows from the imaging geometry. The spatial resolution at the target is

$$r = \frac{FOV}{N}, \tag{3.1}$$

where r is the resolution in mm per pixel, FOV the field of view at the specimen plane, and N the number of pixels across it. The field of view depends on the sensor size, the lens focal length, and the camera-to-specimen distance, through the angle of view of the lens. These values are given for each setup in Section 3.4.3. The target speckle size is 3 to 5 times r, so that each speckle spans 3 to 5 pixels in the image.

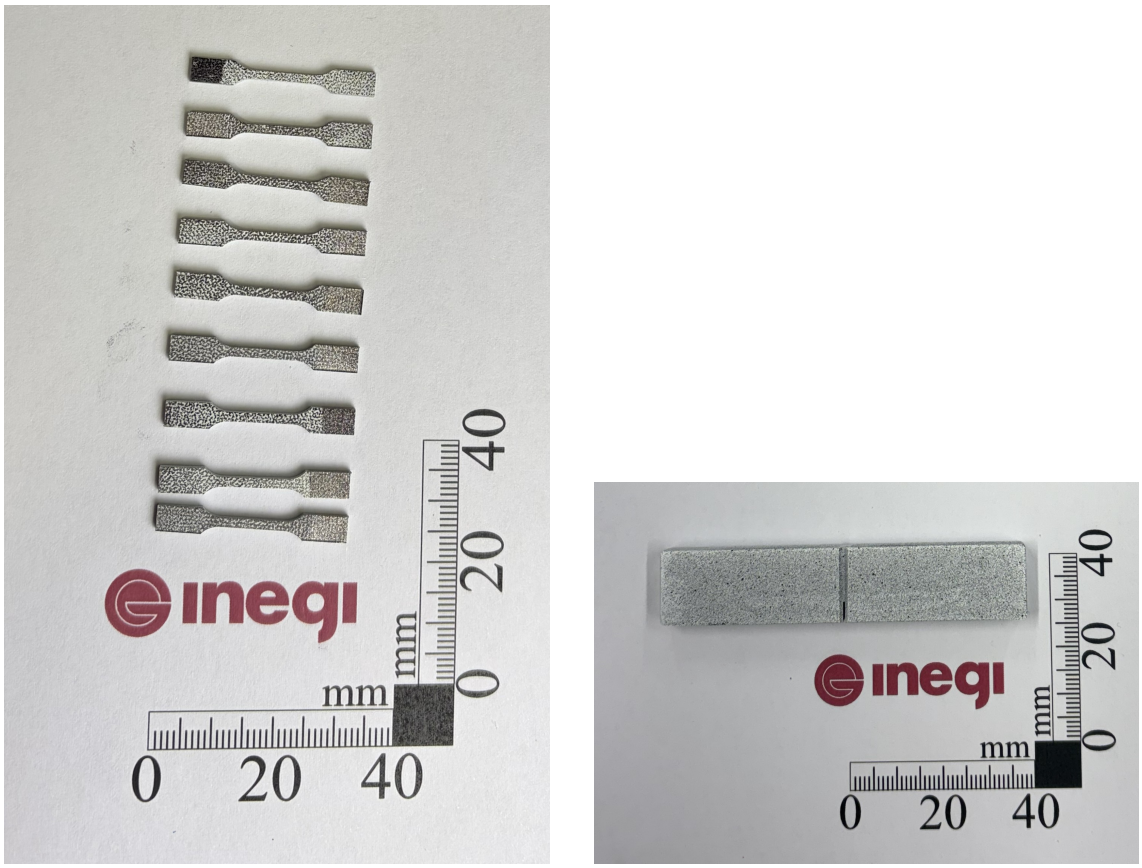
For the tensile setup, the speckle size was computed from this relation. With the camera, lens, and working distance used in those tests, the resolution gave a target speckle of 0.18 mm, near the centre of the 3–5 pixel range. The pattern was applied with a stamp to hold this size, and is shown in Figure 3.4a.

For the fracture setups, the speckle was applied by spray instead, which gives a finer and more random pattern than the stamp. With the same camera and lens as the tensile setup, the smaller sprayed speckle would fall below the 3 to 5 pixel range at the same distance. The camera was therefore moved closer to the specimen, from 320 mm in tension to 230 mm in the quasi-static fracture tests, raising the spatial resolution so that the sprayed speckle again spanned 3 to 5 pixels. The dynamic fracture tests used a sprayed pattern for the same reason, at a working distance of 210 mm. The imaging hardware and working distances are given in Section 3.4.3.

3.4.2 Speckle Application

The pattern was applied in two steps, the same for all specimens. The surface was first sprayed with a white base coat, using a radiator white paint, applied in successive thin layers about two minutes apart until the surface was matt and free of reflections. The white base gives the contrast needed for correlation and removes the specular glare of the bare metal.

The black speckle was then applied over the white base, by two methods. For the tensile specimens, a stamp was used, which holds the controlled 0.18 mm speckle designed in Section 3.4.1, represented in Figure 3.4a. For the fracture specimens, a black spray was used, giving the finer random pattern of Figure 3.4b.



(a) (b)

Figure 3.4: Speckle patterns used in this work. (a) stamped pattern on a miniaturised tensile specimen; (b) sprayed pattern on a SENB fracture specimen.

3.4.3 Imaging Hardware

Three DIC setups were used, one for the tensile tests, one for the quasi-static fracture tests, and one for the dynamic tests, each matched to the timescale of its event. All use the same 2D DIC principle and differ in the camera, the lens, the illumination, and the working distance. The parameters are listed in Table 3.4.

The tensile tests used a Baumer VCXU-123M with a Sony IMX253 1.1″ global-shutter CMOS sensor, 4096×3000 pixels of 3.45 µm, at a working distance of 320 mm, with acquisition through the Dantec Istra4D software [21]. The quasi-static fracture tests used a Basler a2A1920-160umBAS with a Sony IMX392 CMOS sensor, 1920×1200 pixels of 3.45 µm, at a working distance of 230 mm. Both used the same VS-HVA2524 lens of 25 mm focal length at f/2.4, and both ran at 10 frames per second, which resolves the quasi-static event.

The dynamic tests need a much higher frame rate, since the event lasts a few hundred microseconds. They used a Photron FASTCAM Nova S6, a high-speed CMOS camera with a 1024×1024 pixel sensor of 20 µm pixels at full resolution, at a working distance of 210 mm. The camera ran at 80 000 frames per second, which requires a reduced sensor window of 512×128 pixels, so the

image resolution is below the full sensor format. The lens was a Nikon AF-S NIKKOR 50 mm f/1.4G with a PK-11A extension ring.

DIC requires strong and uniform illumination, free of specular glare. The dynamic tests used two GSVITEC MultiLED QX high-intensity units, chosen for the very short exposure of the high-speed camera, where the 1/300 000 s shutter leaves little time to collect light.

Table 3.4: Imaging hardware for the three DIC setups.

	Tensile	Quasi-static fracture	Dynamic fracture
Camera	Baumer VCXU-123M	Basler a2A1920-160umBAS	Photron FASTCAM Nova S6
Sensor	Sony IMX253, 1.1″ CMOS	Sony IMX392 CMOS	CMOS
Resolution (px)	4096×3000	1920×1200	512×128
Pixel size (µm)	3.45	3.45	20
Lens	VS-HVA2524, 25 mm, f/2.4	VS-HVA2524, 25 mm, f/2.4	Nikon AF-S 50 mm f/1.4G + PK-11A
Frame rate (fps)	10	10	80 000
Shutter speed (s)	—	—	1/300 000
Illumination	Walimex Pro Niova 150-F Pro, HEDLER DF-15	Auxiliary lights of the travelling microscope setup	2× GSVITEC MultiLED QX
Working distance (mm)	320	230	210

3.4.4 Calibration and Correlation Parameters

The displacement fields were computed with VIC-2D 7 [19]. Each setup was calibrated independently, since the working distance and the framing differed between them.

Each scale was set from a known length in the object plane. A fixture of known diagonal was placed in the field of view, in the plane of the specimen surface, and its diagonal gave the pixel-to-millimetre conversion in VIC-2D. The resulting scale factors were 0.0531 mm/pixel for the tensile setup, 0.0619 mm/pixel for the quasi-static fracture setup, and 0.0596 mm/pixel for the dynamic setup. These factors convert the measured displacements, including the crack mouth opening, directly into millimetres, which is the input required for the J calculation described in Section 2.3.7.

The correlation parameters are listed in Table 3.5. The subset sets the area of pixels matched between images. It was chosen as a trade-off between noise and resolution: a larger subset lowers the correlation uncertainty but reduces the number of independent points across the region of interest. For each setup, the subset was set to keep the mean correlation uncertainty below 0.02 pixels while still fitting at least three subsets across the smallest dimension of the region of interest, the dimension that limits how many subsets fit. For the tensile specimens this is the width of the gauge

section; for the bend specimens, where the region of interest runs along the crack path, it is the dimension perpendicular to it. The step, the spacing between computed points, was 7 pixels in all three setups. Matching used an optimised 8-tap interpolation with exhaustive search, and the correlation was run incrementally, each image referenced to the previous one rather than to the initial reference. Incremental correlation suits the fracture tests, where the crack opening introduces large local displacements between frames. Strains were computed from the displacement field using the engineering strain tensor.

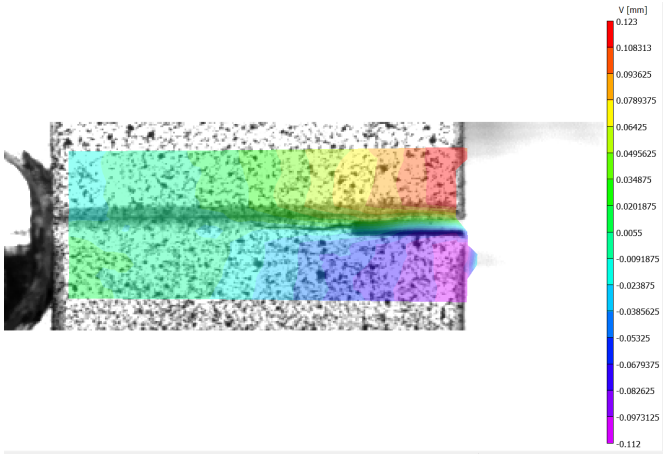
Table 3.5: DIC correlation parameters for the three setups.

	Tensile	Quasi-static	Dynamic
Subset (px)	29	47	17
Step (px)	7	7	7
Scale (mm/px)	0.0531	0.0619	0.0596
Interpolation		Optimised 8-tap	
Search		Exhaustive	
Correlation		Incremental	
Strain tensor		Engineering	

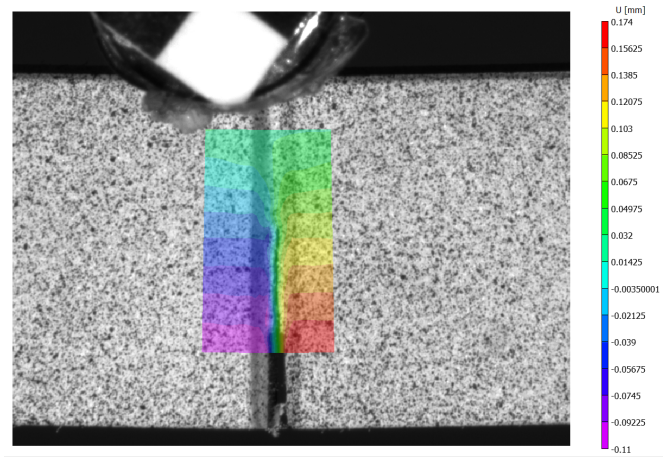
3.4.5 Crack-Length Determination by DIC

The crack length through the test was measured from the DIC fields rather than by mechanical means such as unloading compliance. The same method was used for the quasi-static and the dynamic tests. Only the specimen orientation and a few test-specific details differ, and these are given in the sections of each test.

The method rests on two field quantities. The strain locates the crack plane, and the displacement measures the opening. The strain normal to the crack concentrates in a narrow band along the crack path, and the crack line is taken as the median position of that band. The normal component is used, ε_{yy} in the dynamic tests, where the crack runs along x, and ε_{xx} in the quasi-static tests, where the specimen is rotated and the crack runs along y. The crack line is fixed once, from the first loaded stages, and held constant through the test. This keeps it from jumping between frames, since the crack plane does not move.



(a)



(b)

Figure 3.5: Displacement field across the crack. (a) Vertical displacement v in a dynamic test, where the crack opens vertically. (b) Horizontal displacement u in a quasi-static test, where the specimen is rotated and the crack opens horizontally. The discontinuity along the crack separates the two halves, and the crack opening displacement is the jump across it.

The crack opening displacement (COD) is the separation between the two crack faces, measured perpendicular to the crack. It is taken from the displacement field, as the difference in the opening-direction displacement between the two sides of the crack line. This is the displacement v in the dynamic tests, where the crack opens vertically, and u in the quasi-static tests, where it opens horizontally. Figure 3.5 shows the discontinuity along the crack, with the two halves displaced in opposite directions, and the COD is the jump across that discontinuity. A narrow strip next to the crack faces is skipped when sampling the displacement, because the correlation degrades there.

The crack tip is the point along the path where the opening closes. From the mouth towards the ligament, the COD decreases and reaches zero at the tip. Ahead of the tip the faces are still joined and there is no opening. The tip is located as the position where the COD drops to the noise level of the closed side, which defines the current crack length.

The crack lengths measured on the fracture surface, a_0 and a_f, anchor and validate this record.

The initial value a_0 fixes the starting point of the DIC crack length. The final value a_f is compared with the length reached by the DIC, as an independent check. The fracture-surface measurement is described in Section 3.7.2.

3.5 Tensile Characterisation of AA2024

3.5.1 Miniaturised Specimen Geometry

The temper of the AA2024 was unknown, so its quasi-static properties were measured in tension before the fracture tests. These properties feed the flow stress used in the J calculations.

The tensile specimens were cut from the same AA2024 SENB stock used for the fracture tests. The material available was limited to the offcuts of these specimens, which set the specimen size. A miniature flat geometry was used, following the miniature specimen annex of ASTM E8 [11], with the dimensions in Figure 3.6. The gauge section is 10 mm long with a 1.5×1.5 mm cross-section, and the total length is 30 mm.

The specimens were cut by electrical discharge machining at INEGI, then polished on a rotating polisher with progressively finer grit up to P2500 to remove the recast layer left by EDM and produce a smooth gauge surface.

Because the specimens come from the same stock as the fracture specimens, their orientation relative to the rolling direction is the same, and equally undocumented (Section 3.3.2). The measured properties therefore correspond to an unspecified orientation. Tensile properties are far less sensitive to orientation than toughness, varying by a few percent rather than the 10 to 15% seen previously for toughness, so this has a minor effect on the tensile results.

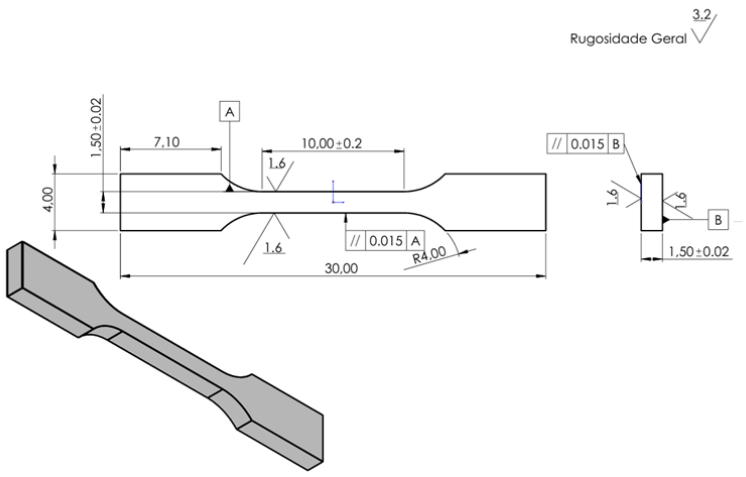


Figure 3.6: Miniaturised tensile specimen geometry and dimensions (mm).

3.5.2 Test Setup and Procedure

The tests were run on a Shimadzu AGX-V universal testing machine of 300 kN nominal capacity, fitted with a 5 kN load cell. The setup is shown in Figure. 3.7. The cell was selected from the recommendation that the expected maximum force should fall between 10 and 80% of its capacity, with the smallest qualifying cell preferred to keep the resolution high. The force expected for these specimens was about 1 kN, which places the test near 20% of the 5 kN cell.

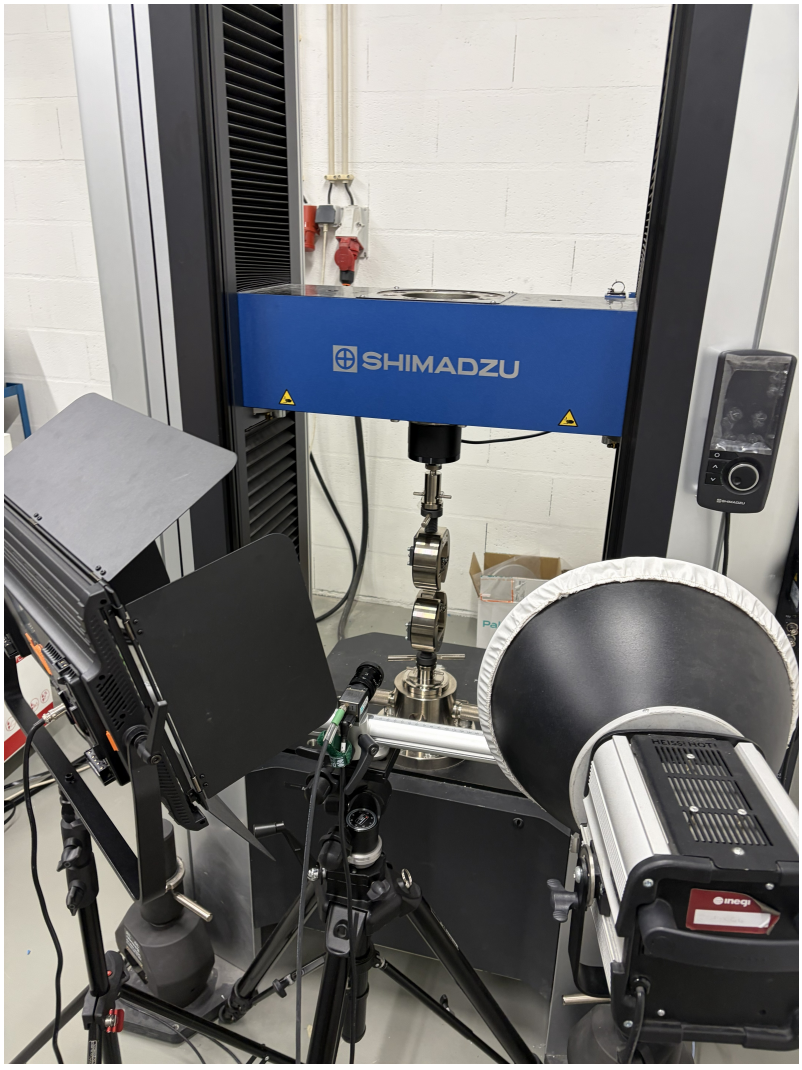


Figure 3.7: Tensile test setup, showing the Shimadzu AGX-V, the DIC camera, and the two LED lights.

The tests were run in displacement control at a constant crosshead speed throughout. ASTM E8 [11] sets the test speed through the strain rate over the parallel section of the specimen. For the determination of yield properties under Control Method C, the standard specifies a crosshead rate of 0.015 ± 0.003 mm per mm of parallel length per minute. With a parallel section of 10 mm, this gives a crosshead speed of 0.15 mm/min, which was held constant for the whole test. Keeping the lower yield-region rate for the entire test is conservative. The standard allows a higher rate once

the yield properties have been recorded, but the slower rate was kept throughout, at the cost only of test duration.

Strain was measured by digital image correlation rather than by a contact extensometer, using the quasi-static setup of Section 3.4. A virtual extensometer of 8.5 mm gauge length was defined on the gauge section in VIC-2D, and the strain was taken from its elongation. Figure 3.8 shows the specimen in VIC-2D with the region of interest and the virtual extensometer. The stress was computed from the load and the initial cross-sectional area of the gauge section.

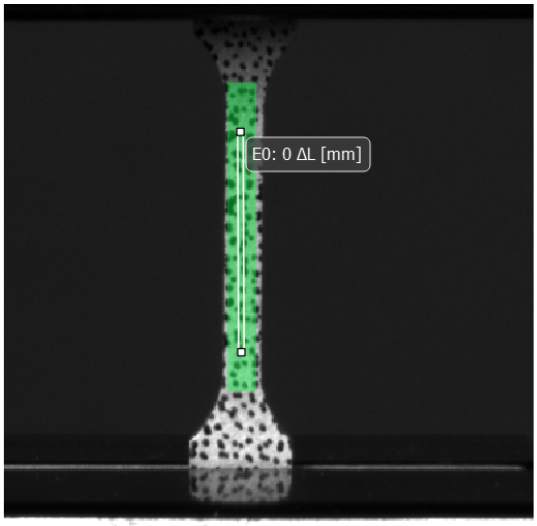


Figure 3.8: Miniaturised tensile specimen in VIC-2D, showing the region of interest and the virtual extensometer used to measure strain.

Force and images were synchronised through an analogue signal. The Shimadzu machine outputs a voltage proportional to the load, recorded by the Dantec acquisition system alongside the images, so that each frame carries an associated voltage. The two records were then aligned by matching the instant of maximum force in the machine data with the maximum of the analogue voltage signal. Image acquisition and the analogue recording were handled by the Dantec Istra4D software [21]; the correlation was processed separately in VIC-2D [19], as described in Section 3.4.

The stress was computed from the load and the initial cross-sectional area of the gauge section, and the strain from the virtual extensometer in VIC-2D. The two give the stress–strain curve used for the data reduction in Section 3.5.3.

3.5.3 Data Reduction

The cross-section of each specimen was measured before testing, and the initial area was taken from these measurements rather than from the nominal drawing value. The engineering stress was computed as the load divided by this initial area, and plotted against the strain from the virtual extensometer. Three properties were taken from the resulting curve, following ASTM E8 [11].

The Young's modulus was taken from the slope of the linear elastic region. The yield strength was taken at a 0.2% offset, as the intersection between the stress–strain curve and a line parallel to the elastic slope shifted by 0.2% strain. The ultimate tensile strength was taken as the maximum stress reached during the test.

These properties feed the fracture analysis. The flow stress used in the validity checks of ASTM E1820 [9], taken as the average of the yield and ultimate strengths, comes from the values measured here. The properties are reported in Chapter 4.

3.6 Fatigue Pre-Cracking

A sharp fatigue crack was grown from the machined notch before testing, as required by ASTM E1820 [9]. The pre-cracking was done on the same Step Lab machine used for the quasi-static fracture tests, in three-point bending under force control. It was carried out before the side grooves were cut, so the specimen was at its full thickness B throughout. The crack was followed optically during pre-cracking, with travelling microscopes on both faces of the specimen. The specimens were polished again beforehand so that the crack could be seen propagating. Watching both faces checks that the crack grows symmetrically through the thickness, as the standard requires. The setup is shown in Figure 3.9.

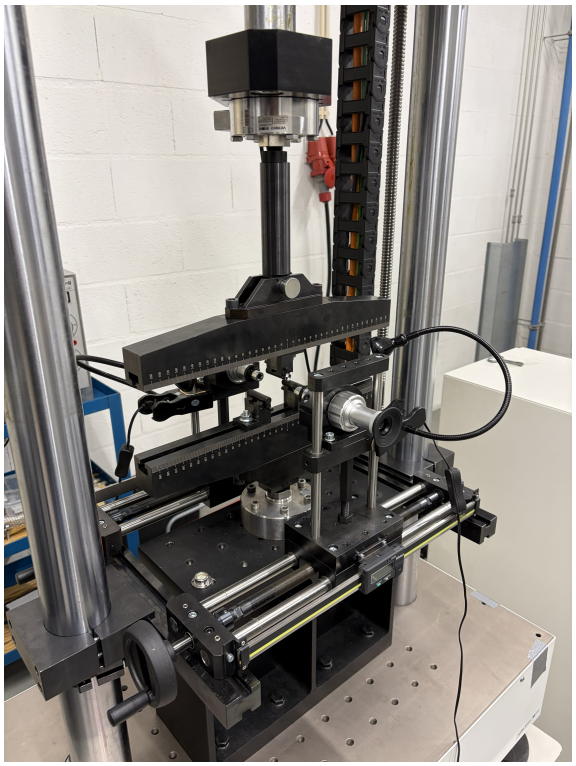


Figure 3.9: Fatigue pre-cracking setup on the Step Lab machine, in three-point bending, with the travelling microscopes used to follow the crack on both faces.

The fatigue loads were set from two limits in ASTM E1820. The first is the limiting force P_m, which keeps the uncracked ligament from yielding during pre-cracking,

$$P_m = \frac{0.5\, B\, b_0^2\, \sigma_Y}{S}, \tag{3.2}$$

where B is the thickness, $b_0 = W - a_0$ the initial ligament, S the span, and σ_Y the effective yield strength, taken as the average of the yield and ultimate strengths. The applied maximum force was kept below P_m for both alloys.

The second limit is on the maximum stress intensity factor during pre-cracking, $K_{\max}$, kept well below the fracture toughness of the material so that the crack tip is not damaged. For the bend specimen, $K_{\max}$ comes from the maximum fatigue force through the stress intensity expression already given for this geometry in Equation 2.6, evaluated at $P_{\max}$. A load ratio of $R = P_{\min}/P_{\max} = 0.1$ was used, as recommended by the standard. Pre-cracking was done in two steps, the final one covering at least the last half of the pre-crack at a lower $K_{\max}$ to leave a sharp tip.

The flow stress came from the certificate for the AA6082-T651 and from the tensile tests of Section 3.5 for the AA2024. The maximum force was 1100 N for both alloys, both below the respective P_m, giving a $K_{\max}$ near 12 MPa $\sqrt{\text{m}}$, well under the toughness of either alloy. Table 3.6 gives the parameters for each alloy.

Table 3.6: Fatigue pre-cracking parameters for the two alloys.

	AA2024	AA6082-T651
Effective yield strength, σ_Y (MPa)	338	330
Limiting force, P_m (N)	1189	1160
Load ratio, R	0.1	0.1
Maximum force, $P_{\max}$ (N)	1100	1100
Minimum force, $P_{\min}$ (N)	110	110
Target a_0/W	0.5	0.5
Resulting $K_{\max}$ (MPa $\sqrt{\text{m}}$)	12.7	12.8

Crack growth was followed optically. The crack was monitored on both faces with travelling microscopes. Pre-cracking was stopped when the crack reached the target length, giving $a_0/W \approx 0.5$. Figure 3.10 shows a specimen after pre-cracking. The crack length on each specimen was measured afterwards and used in the individual data reduction.

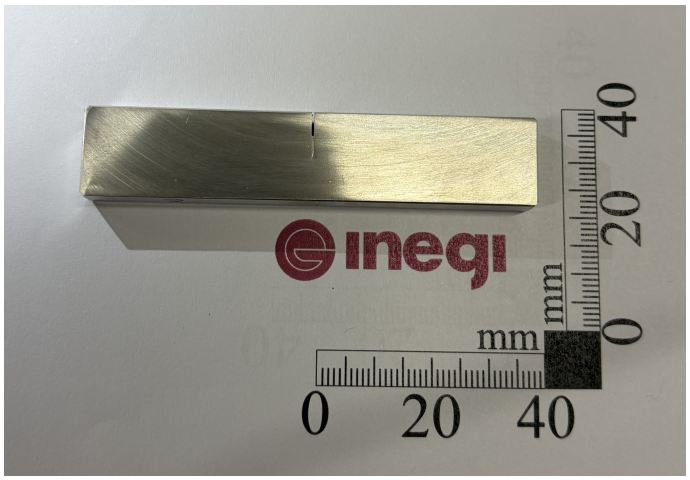


Figure 3.10: Specimen after fatigue pre-cracking, showing the sharp crack extending from the machined notch.

3.7 Quasi-Static Fracture Testing

3.7.1 Apparatus and Fixtures

The quasi-static fracture tests were run on a STEPLab EA050 machine with a BV020 controller and a 50 kN load cell, in three-point bending. The specimen rested on two support rollers spanning $S = 60$ mm ($4W$), with the load applied at mid-span by a third roller. All three rollers are free to rotate, which reduces friction at the contact points, as required by ASTM E1820 [9]. Force came from the machine load cell, recorded by the STEPLab software. The setup is shown in Figure 3.11.

Surface deformation was measured by digital image correlation, using a Basler a2A1920-160umBAS camera with a Sony IMX392 CMOS sensor, at the working distance and correlation settings given in Section 3.4. Images were recorded at 10 frames per second over a region of interest cropped to the crack-tip zone. The calibration used a fixture of known diagonal placed in the specimen plane, under the same distance and illumination as the test.

Force and images were synchronised by absolute time. A script recorded each image with an absolute timestamp, written to a log together with the frame, and the force record from the STEPLab was aligned to the images through this timestamp. This replaces the manual synchronisation used in the tensile tests, where no single load peak is available to anchor the two records.

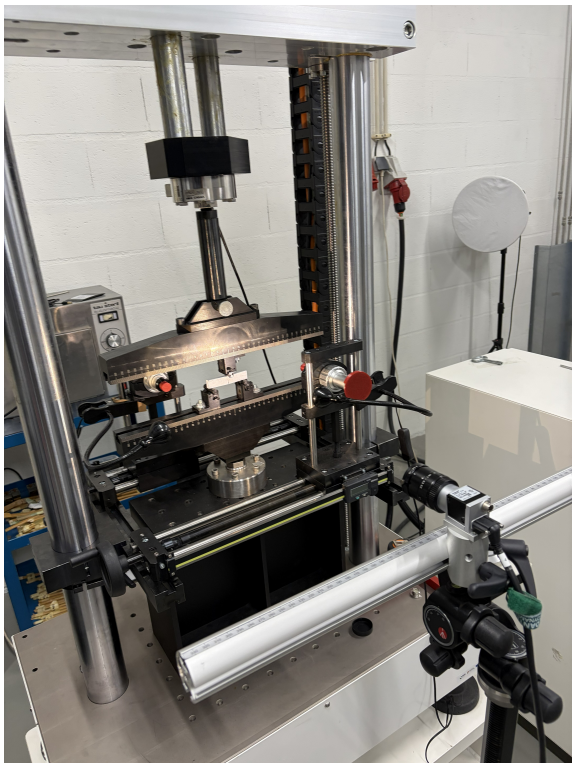


Figure 3.11: Quasi-static fracture test setup on the STEPLab machine, in three-point bending, with the DIC camera and illumination.

Figure 3.12 shows the loading protocol. The test begins with three unload–reload cycles between 800 and 600 N, a level low enough not to extend the crack, used to estimate the initial elastic compliance. The specimen is then loaded in stroke increments, each followed by a partial unloading of about 200 N. The increments are reduced from 0.02 to 0.01 mm at the higher loads, where the crack propagates, to place more points in that region. The force rises to a maximum and then falls as the crack grows and the ligament is consumed. About 40 cycles were run per specimen.

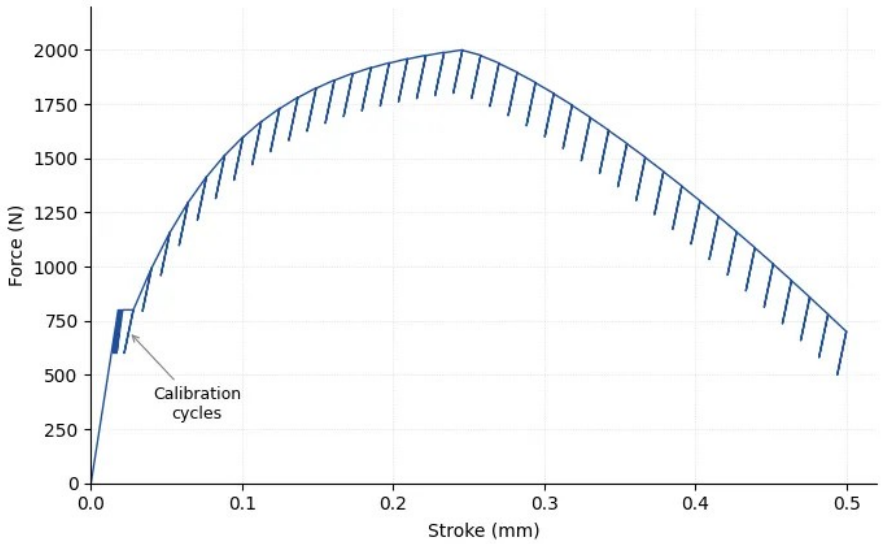


Figure 3.12: Schematic of the quasi-static loading protocol, showing the calibration cycles, the incremental loading with partial unloadings, and the rise and fall of the force as the crack grows. The values are representative and vary between specimens and alloys.

This protocol was designed for the unloading-compliance method of ASTM E1820, in which the crack length is inferred from the elastic compliance measured at each unloading. During data processing, the direct DIC measurement of the crack tip, described in Section 3.4.5, proved more effective than inferring the crack length from the compliance, and was adopted instead. The change also strengthens the measurement: the crack length is read from the specimen surface rather than reconstructed from the stiffness. The unloading cycles were kept in the analysis with two roles. Each cycle provides one point of the J-R curve, and the compliance computed from its force and CMOD records serves as an independent check on the DIC crack length.

The data reduction follows from this. At the peak load of each cycle, J is evaluated through the incremental formulation of Annex A9 given in Section 2.3.5.3, with the plastic area integrated from the force–CMOD record up to that point, and the crack extension Δa taken from the DIC crack length at the same instant. Each cycle therefore contributes one $(J, \Delta a)$ point, and the roughly 40 cycles per specimen set the resolution of the quasi-static J-R curve.

3.7.2 Crack-Length Measurement on the Fracture Surface

The crack lengths were measured on the fracture surface after testing, to anchor and validate the DIC record of Section 3.4.5. The measurement follows the optical procedure of ASTM E1820 [9]. The fracture surface was imaged on an AmScope microscope with its camera and measurement software, and the crack front was measured at nine positions equally spaced across the thickness.

The crack length was taken as the average of the nine readings, following the weighting of ASTM E1820. The two surface positions are averaged together and counted as one, and this value is averaged with the seven interior positions. The standard requires the crack front to be reasonably

straight, so no individual reading may differ from the average by more than a set tolerance. The readings give the crack extension measured from the root of the machined notch, so the crack length a used in the analysis is this value plus the 4 mm notch depth, measured from the loaded surface as the standard defines.

Two crack lengths were measured this way. The initial length a_0 is the front of the fatigue pre-crack, and the final length a_f is the front reached at the end of the test. The fracture surface was exposed by fatiguing the specimen after the test and breaking it open, which marks the final front and separates it from the pre-crack front. The initial length a_0 fixes the starting point of the DIC crack length, and a_f gives an independent check on the length reached by the DIC at the end of the test.

3.8 Dynamic Fracture Testing

3.8.1 SHPB Apparatus and Three-Point Bending Fixtures

The dynamic fracture tests were carried out on the split Hopkinson bar of the Advanced Monitoring and Structural Integrity (UMAI) laboratory at INEGI. The original system was designed and built by Ferreira [31] in the early 2000s, and later renovated by Shamchi [60], who replaced the bars with titanium and built the dynamic three-point bending configuration used in this work. The wave-propagation theory behind the technique is given in Section 2.6.1; this section describes the apparatus and the bending fixture. Figure 3.13 shows the layout of the system.

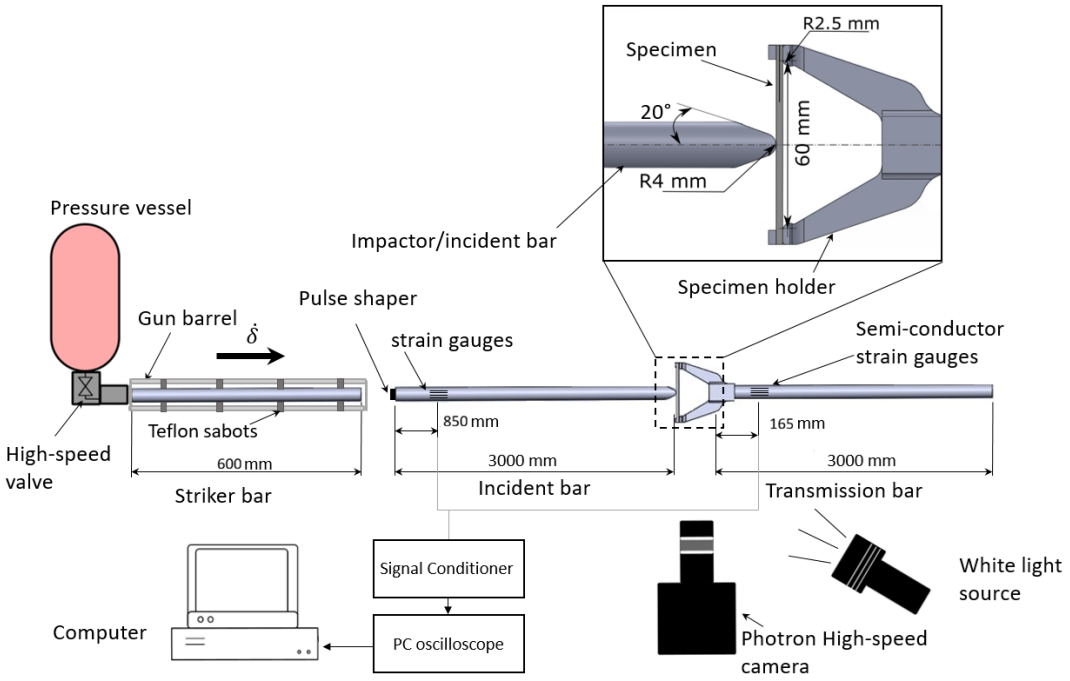


Figure 3.13: Schematic of the dynamic three-point bending split Hopkinson bar, showing the gas gun, the striker, the incident and transmitted bars with their strain gauges, and the specimen held in the three-point bending fixture. Adapted from Shamchi [60].

The incident and transmitted bars are titanium Grade 5 (Ti-6Al-4V), each 3000 mm long and 16 mm in diameter. Titanium lowers the impedance mismatch between the bars and the aluminium specimen, which raises the amplitude of the transmitted signal and improves the resolution of the measured force. The one-dimensional elastic wave speed in the bars is $C_0 \approx 5060$ m/s.

In the three-point bending configuration, the specimen is not placed between the bars as in a compression test. The single-edge notched bend specimen rests on a V-shaped holder mounted on the transmitted bar, and the incident bar strikes its mid-span, applying the central load of a three-point bend test. The load is delivered by a striker launched by a gas gun against the free end of the incident bar, fired at a nominal reservoir pressure of 2 bar. This pressure is read on an analogue gauge with half-bar divisions, so it carries a reading uncertainty of about ± 0.25 bar, half the smallest division. The striker is 600 mm long. Its length sets the duration of the incident pulse, since the pulse lasts for the time the stress wave takes to travel up the striker and back,

$$\tau = \frac{2L_{\text{striker}}}{C_0}, \tag{3.3}$$

where L_{striker} is the striker length and C_0 the elastic wave speed in the bar material. For the 600 mm titanium striker, this gives a pulse of about 237 µs.

A pulse shaper is placed on the impact face of the incident bar, between the striker and the bar. It is a copper disk 1.5 mm thick, shown in Figure 3.14. On impact, the shaper deforms plastically and damps the initial impact, which increases the rise time of the incident pulse and produces a gradual loading instead of a sharp step. This lengthened rise smooths the loading, attenuates the high-frequency oscillations that cause wave dispersion along the bars, and gives the specimen time to reach dynamic equilibrium before the peak load, as discussed in Section 3.8.3. Copper is a standard shaper material for specimens of lower yield strength, where a longer rise time is needed [60]. It deforms plastically in a repeatable way and withstands repeated impacts without appreciable degradation, which keeps the shaping of the incident pulse consistent between tests.

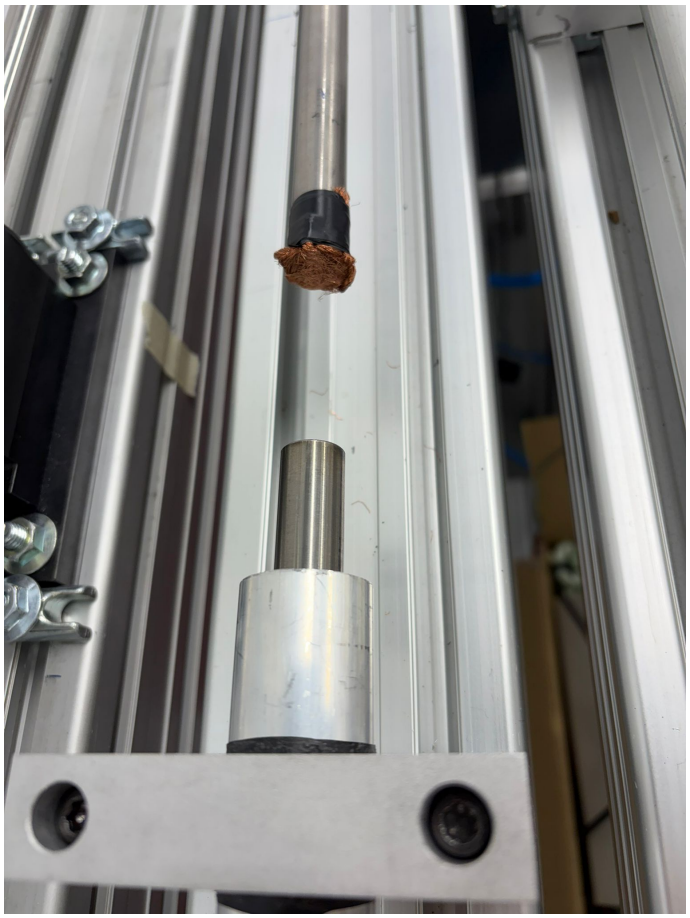


Figure 3.14: Copper pulse shaper mounted on the impact face of the incident bar.

The incident bar carries a metallic foil gauge (HBM 1-LY43-3/350, 350 Ω, gauge factor 2.06), bonded 2150 mm from the specimen. The transmitted bar carries a semiconductor gauge (Kyowa KSPB-1-350-E4, 350 Ω, gauge factor 164), bonded 165 mm from the specimen. The semiconductor gauge has a gauge factor about eighty times that of the foil gauge, which is needed on the transmitted bar because the wave transmitted through the aluminium specimen is weak and would otherwise be poorly resolved. The choice of gauge positions follows from the need to separate the incident and reflected pulses in time, discussed in Section 4.3.2.

Surface deformation was recorded by high-speed imaging for the digital image correlation analysis. The Photron camera and the two GSVITEC LED units were aligned with the specimen at mid-span, as shown in Figure 3.15. The imaging settings and the crack-length measurement are described in Section 3.4.

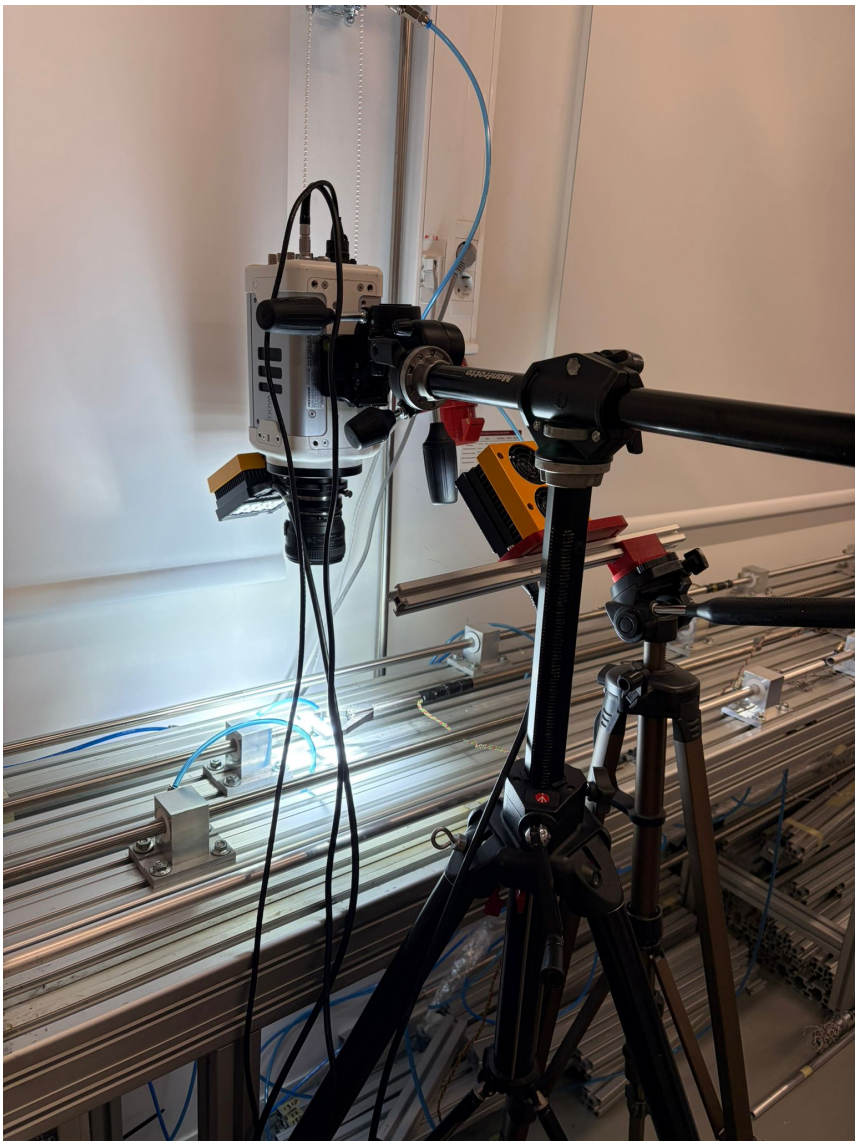


Figure 3.15: High-speed imaging setup for the dynamic tests, with the Photron camera and the two GSVITEC LED units.

3.8.2 Force Determination from the Transmitted Bar

Once dynamic equilibrium is reached, the load applied to the specimen is taken from the transmitted-bar signal through Equation 3.4, rather than from the incident bar. The transmitted signal is free of the high-frequency inertial oscillations that contaminate the incident bar during the early part of the event, so it gives a cleaner measure of the force on the cracked ligament.

The strain in each bar was obtained from its strain gauge, and the signals were recorded on a PicoScope at a sampling rate of 20 MHz. The gauge signal is a voltage, converted to strain through a calibration coefficient determined for each bar before the tests. The strain was then converted to force using the bar properties,

$$P(t) = E_b A_b \, \varepsilon_T(t), \tag{3.4}$$

where $E_b = 114$ GPa is the Young's modulus of the titanium bars, A_b the cross-sectional area of the 16 mm bar, and ε_T the strain measured on the transmitted bar.

The voltage-to-strain coefficient of each bar was found by direct calibration against a reference load cell. The bar was loaded in tension in several steps by tightening a bolt, from no load up to a set tightening level. At each step, the force was read from the calibrated reference cell and the corresponding voltage from the strain gauge. The strain produced by each force follows from the bar properties, $\varepsilon = F/(E_b A_b)$, so each step gives a pair of voltage and strain values. A line fitted through these pairs gives the coefficient that relates the gauge voltage to the bar strain. The calibration was repeated over four runs for each bar. Because the bars remain elastic and the gauges respond linearly to axial strain, the coefficient obtained in static tension applies to the compressive waves of the dynamic test.

3.8.3 Dynamic Equilibrium Verification

The quasi-static fracture formulae apply only when the specimen is in dynamic equilibrium, with the force on the loaded face equal to the force on the supports. At the start of the event the specimen is not in equilibrium. The incident pulse reaches the loaded face while the support side has not yet responded, and the specimen rings up through a few internal wave reflections before the two forces equalise. The load measured on the bars represents the force on the ligament only after this point, so the equilibrium has to be verified for each test.

Equilibrium is checked by comparing the two forces acting on the specimen, computed from the bar signals as set out in Section 2.6.2. The force on the loaded face follows from the incident and reflected waves, $F_1 = E_b A_b(\varepsilon_I + \varepsilon_R)$, and the force on the support side from the transmitted wave, $F_2 = E_b A_b \, \varepsilon_T$. The first is the two-wave estimate and the second the one-wave estimate. While the specimen rings up, the two differ. Once it reaches equilibrium, they coincide, and from that point $F_1 \approx F_2$ holds.

The two forces are compared directly, by plotting F_1 and F_2 on the same time axis and checking that they overlap through the analysis window; the results are in Section 4.3.1. In compression testing the usual criterion is a normalised difference between the two forces, accepted below a fixed tolerance. That criterion does not apply here. In three-point bending the incident and reflected pulses nearly cancel on the loaded face and the transmitted pulse is small, so the ratio is dominated by signal noise. Equilibrium is instead ensured by the timing conditions of Section 4.3.2, which require crack initiation to occur well after the specimen has rung up.

3.8.4 Synchronisation of Force and Crack Length

The crack front through the test was measured from the DIC fields by the method of Section 3.4.5, the same as in the quasi-static tests. The initial crack length a_0 was measured on the fracture surface by the procedure of Section 3.7.2. In the dynamic tests the specimen fractured completely,

so the crack ran through the full ligament and the final crack length is the specimen width, $a_f = W$. The crack growth between a_0 and final fracture is the part measured by the DIC, which gives the crack length at each frame.

The crack length and the CMOD therefore come from the high-speed images, indexed by frame number, while the force comes from the bar strain gauges, digitised by the PicoScope at 20 MHz. The two share no common time base. Building the *J*-*R* curve requires the force, the crack length, and the CMOD together at each instant. The crack length and the CMOD are already synchronised with each other, since both are extracted from the same images and share the frame index. What remains is to bring the force onto the same time base. Each frame is converted to a time through

$$t = T_0 + \frac{i}{\mathrm{FPS}}, \tag{3.5}$$

where i is the frame number, FPS is the frame rate of the camera, and T_0 is the origin, the instant on the PicoScope time base that corresponds to frame zero. The frame rate sets the spacing between frames, 12.5 µs at 80 000 fps. The two systems do not share a common trigger, so T_0 has to be determined.

The anchor for T_0 is the instant the incident bar contacts the specimen, identified directly in the images. In the frames before loading the notch is closed and the specimen has not bent. In the frame where the striker touches the specimen, the contact and the start of bending are visible. That frame marks the physical instant at which load begins to enter the specimen. The frame is identified by eye, test by test, which avoids relying on a threshold applied to a noisy signal.

This contact corresponds to the arrival of the incident pulse at the specimen. The incident wave carries the load into the specimen, so its onset is the natural reference for the start of loading, unlike the reflected wave, which returns later. The contact frame is aligned with the onset of the incident wave. A transit-time correction is required here. The incident wave is measured at the gauge on the incident bar, 2150 mm from the specimen, and the wave passes the gauge before it reaches the specimen. This travel time, about 425 µs at the wave speed of 5060 m/s, is subtracted from the incident signal so that its onset falls at the instant the wave reaches the specimen, the same instant as the contact seen in the image. Without this correction the alignment would be off by hundreds of microseconds.

With T_0 fixed, the time of each frame is computed and the force interpolated at that instant. The force used for the J calculation is the transmitted force, itself referred to the specimen by subtracting the travel time over the 165 mm between the specimen and the transmitted-bar gauge, about 33 µs. The result is a table in which each frame carries its crack length, its CMOD, and the corresponding force.

Synchronisation fixes the correspondence between the force time base and the frames, that is T_0. It does not determine when the crack begins to grow. The onset of crack growth is not read from the images by eye, because the initial opening can be hidden under the speckle paint and only becomes visible once it is large. Crack growth is measured from the DIC displacement field,

which detects the motion by correlation before it is visible, as described in Section 3.4.5.

The synchronisation is checked against the expected physical sequence, in which the force rises, the crack then grows, and the force falls. A crack growing before the force rises points to an error in T_0. The identification of the contact frame is accurate to within one frame spacing, 12.5 µs.

3.8.5 Validity Window

The quasi-static fracture formulae of ASTM E1820 apply to the dynamic test only within a valid time window. The conditions required to define this window are set out in Section 2.6.2. The lower bound is dynamic equilibrium, since the load measured on the bars represents the force on the ligament only after the specimen has rung up to equilibrium, verified as described in Section 3.8.3. Crack initiation must occur after this transition for the static formulation to hold.

The strain-gauge positions were set so that the incident and reflected pulses can be read without overlapping. As the incident wave travels along the bar, reaches the specimen, and returns as the reflected wave, the two pass the gauge at different times. If the gauge is badly placed, the tail of the incident pulse and the front of the reflected pulse arrive together and cannot be separated. The Lagrange diagram in Figure 3.16 traces the wave paths in the position-time plane and shows the window at each gauge in which the incident and reflected pulses are clear of each other.

The wave paths were built from the bar geometry and the wave speed. Each pulse travels at the bar wave speed $C_0 = 5060$ m/s, so its path in the position-time plane is a straight line of slope $1/C_0$. The incident pulse starts at the impact face and reaches the specimen after travelling the 3000 mm of the incident bar, about 593 µs. At the specimen it splits into a reflected pulse, which returns along the incident bar, and a transmitted pulse, which continues along the transmitted bar. The duration of each pulse is set by the striker length through Equation 3.3, about 237 µs for the 600 mm striker, and is marked at the impact face. The gauge on the incident bar sits 2150 mm from the specimen. There the incident pulse passes first, and the reflected pulse arrives later, after travelling to the specimen and back, leaving a clean window in which the incident pulse is read without overlap. The transmitted pulse reaches the transmitted-bar gauge, 165 mm from the specimen, shortly after the split, and is read there.

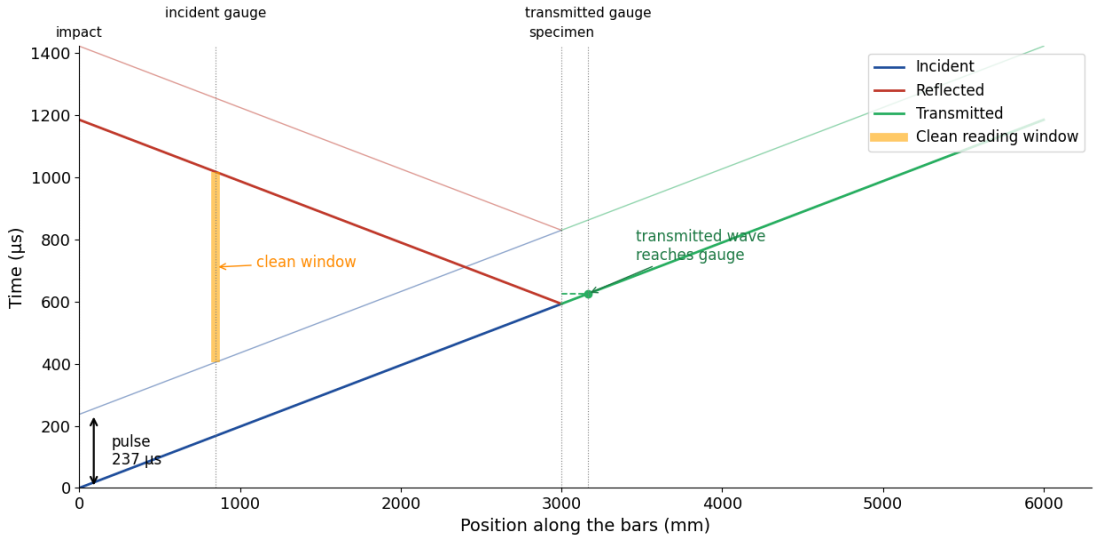


Figure 3.16: Lagrange diagram of the wave propagation in the bars, showing the incident, reflected, and transmitted pulses in the position-time plane, the pulse duration at the impact face, and the clean window in which the incident pulse is read at its gauge.

Three further criteria, set out in Section 2.6.2, bound the validity of the static formulation. The first is the ring-up time, the interval the specimen needs to equalise the forces on its two faces through internal wave reflections. It follows from three reflections across the specimen width W at the bar wave speed of the aluminium [60]:

$$t_{\text{ring}} \approx \frac{3W}{c_0}, \tag{3.6}$$

with $c_0 \approx 5093$ m/s, which gives $t_{\text{ring}} \approx 9$ µs. The copper pulse shaper lengthens the incident pulse so that its rise time is much greater than this, giving the specimen time to reach equilibrium well before the peak load. The second is the transition time of Nakamura, Shih and Freund [46], the instant beyond which the kinetic energy of the specimen falls below its deformation energy and the crack-tip field becomes indistinguishable from the quasi-static one. For a standard three-point bend specimen, Equation 2.35 with $DS \approx 24$ gives $t_T \approx 71$ µs, with $H = W = 15$ mm and $c_0 \approx 5093$ m/s. This longitudinal bar wave speed of the aluminium is distinct from the Rayleigh wave speed, about 2900 m/s. The transition time is the more demanding of the two conditions and sets the lower bound of the window. Only tests in which crack initiation occurs after t_T are treated as valid, and the static formulation is then applied without inertial correction. Tests that do not meet this condition are discarded rather than corrected. A separate condition bounds the inertia of the propagating crack, which the transition time does not cover. The transition time bounds the inertia of the specimen under load, while the crack speed bounds the inertia of the growing crack. These are separate conditions. The inertial contribution to J stays small while the crack runs well below an appreciable fraction of the Rayleigh wave speed, about 2900 m/s. The initiation times and crack speeds measured for each test are reported in Chapter 4.

Chapter 4

Results and Discussion

4.1 Tensile Properties of AA2024

The temper of the AA2024 was unknown, so its quasi-static properties were measured in tension to obtain the flow stress used in the fracture analysis. Nine specimens were tested and five gave valid results; the other four were discarded for poor correlation or misalignment in the grips. The stress–strain curves of the five valid specimens are shown in Figure 4.1, and the measured properties in Table 4.1.

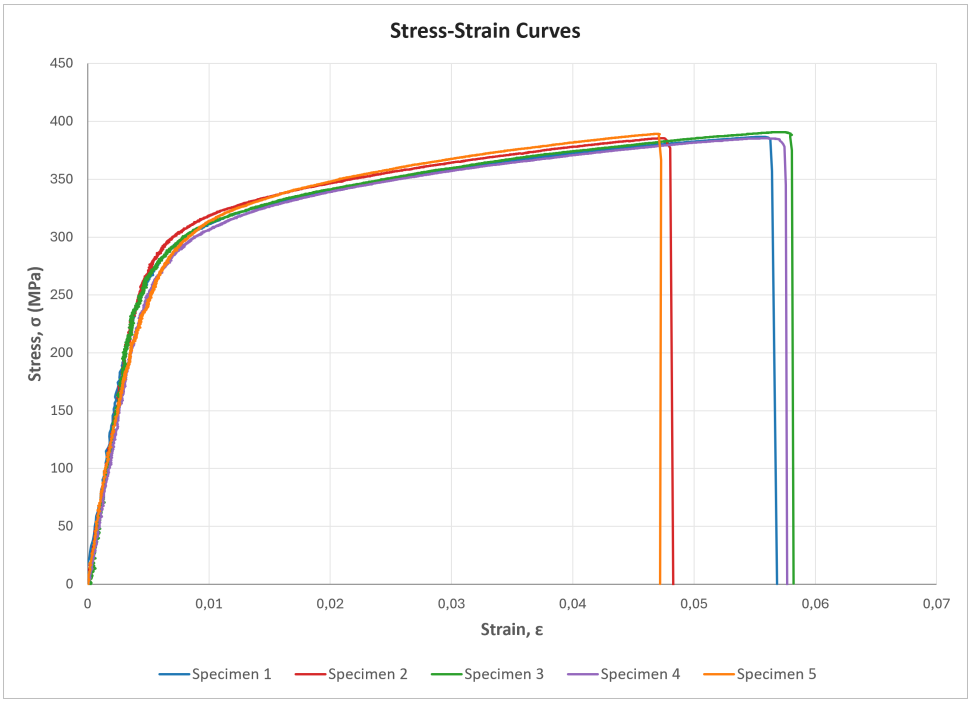


Figure 4.1: Engineering stress–strain curves of the five valid AA2024 tensile specimens.

Table 4.1: Tensile properties of the AA2024, measured on five valid specimens.

Specimen	$R_{p0.2}$ (MPa)	R_m (MPa)	E (GPa)
1	291.4	386.7	53.6
2	295.4	395.6	62.9
3	284.1	390.8	65.9
4	279.8	385.4	58.6
7	283.9	389.2	54.7
Mean	286.9	389.6	59.1
SD	5.2	3.3	4.3

The five curves group closely, which shows good repeatability. The yield strength averages 287 ± 5 MPa and the ultimate tensile strength 390 ± 4 MPa. The specimens fail between 4.7 and 5.8% strain. These values are consistent with AA2024 in a hardened condition.

The curves show no sharp yield point. The stress rises smoothly from the elastic region into a long, gently hardening plastic range, the response expected from a precipitation-hardened Al–Cu–Mg alloy, where the precipitates raise the yield strength but leave room for continued hardening as dislocations accumulate. The yield-to-tensile ratio is $287/390 \approx 0.74$, so the material keeps an appreciable hardening reserve above yield. This reserve matters for fracture, because the hardening ahead of the crack tip redistributes stress and resists the early growth of the crack. The failure strain, near 5%, is moderate. It places the material in a hardened rather than an annealed condition, and is lower than the elongation of soft tempers of the same alloy.

The stresses in Figure 4.1 and Table 4.1 are engineering values, computed from the load and the initial cross-section of the gauge length. Necking after the maximum load is not accounted for, so the final portion of each curve underestimates the true stress in the neck, and the failure strain is an average over the gauge length rather than a local value. The effect on the fracture analysis is small. The yield strength is measured before any necking occurs and is unaffected. The ultimate strength marks the onset of necking, where the true stress exceeds the engineering value by about the uniform strain, a few percent for this material. The effective yield stress therefore carries a slight underestimate of the true flow stress, of the same order. This is accepted rather than corrected: ASTM E1820 [9] defines the effective yield stress from the engineering yield and tensile strengths, so the values used in the J calculations and in the validity checks follow the standard as written.

The Young's modulus is the exception. It averages 59 GPa, well below the 70 GPa expected for aluminium, and scatters more than the strength values. This is not read as a material property. The modulus is taken from the slope of the elastic region, where the strain is small, below about 0.4%, and the DIC noise is a large fraction of the strain being measured. DIC is known to be unreliable in this small-strain range, where the signal-to-noise ratio of the strain field is poor [41, 49, 61]. The effect is worse here because the specimens are small, 1.5×1.5 mm in section, so

any misalignment in the grips adds parasitic bending that distorts the elastic slope further. The modulus is reported for completeness but not used; the reference value for aluminium is used where the modulus enters the fracture calculations.

The modulus does not affect the effective yield stress, which is the quantity the fracture analysis needs. The effective yield stress is the average of the yield and ultimate strengths, and comes from the plateau of the curve rather than its elastic slope, so it is unaffected by the poorly resolved modulus. For the AA2024 it is $(287 + 390)/2 = 338$ MPa. This is the value used in the J calculations and in the validity checks of ASTM E1820, and it replaces the provisional value used to size the fatigue loads in Section 3.6.

4.2 Quasi-Static Fracture

4.2.1 *J-R* Curves and Initiation Toughness

Three specimens of each alloy gave valid results; the remaining specimens were rejected: the AA6082-T651 ones for failing the final crack-front straightness requirement and the AA2024 ones because the final crack length did not match between the direct measurement and DIC. The J-resistance curves were built following Annex A9 of ASTM E1820, shown in Figures 4.2 and 4.3. Each plot shows the experimental points, the power-law fit through the qualified data, the blunting line, the 0.2 mm offset line, and the exclusion lines at 0.15 and 1.5 mm. The initiation toughness J_{Ic} is read where the offset line meets the fit, and the values are listed in Table 4.2.

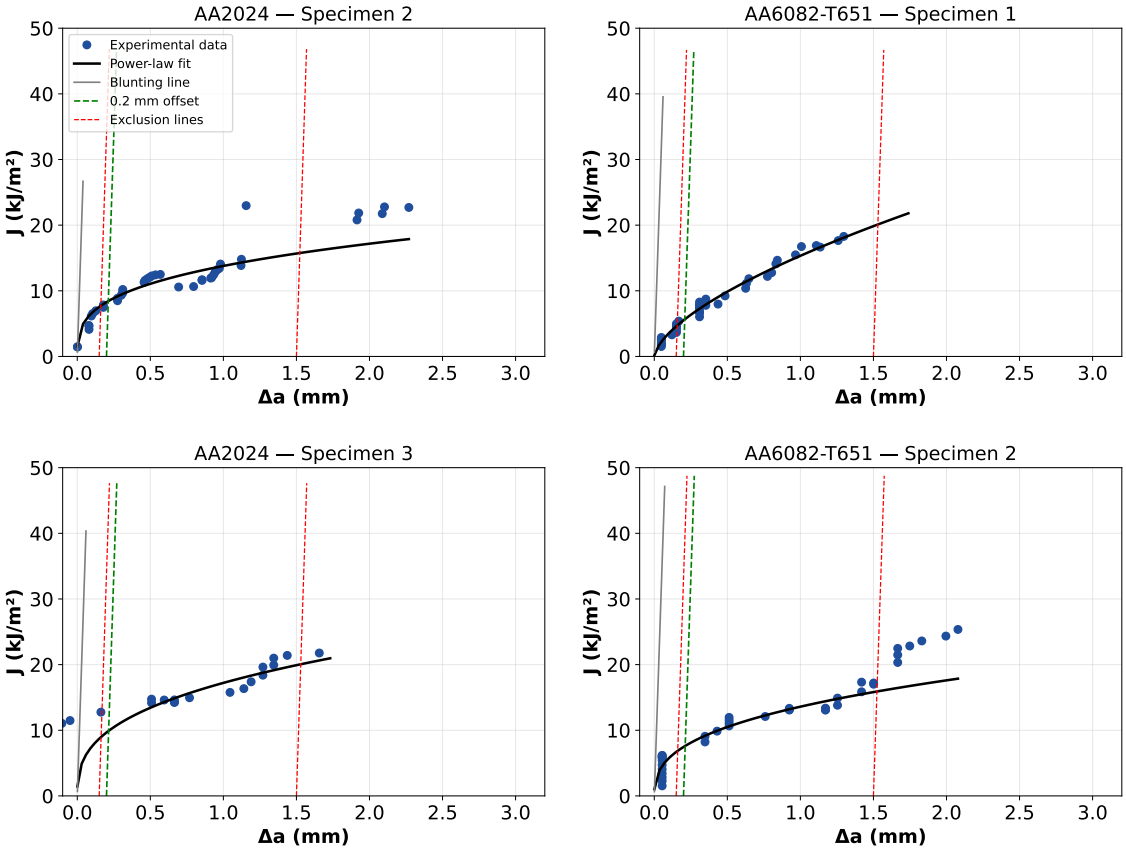


Figure 4.2: *J-R* construction for four of the valid quasi-static specimens, following ASTM E1820 Annex A9. Left column AA2024, right column AA6082-T651. Each plot shows the experimental points, the power-law fit, the blunting line, the 0.2 mm offset line, and the exclusion lines at 0.15 and 1.5 mm.

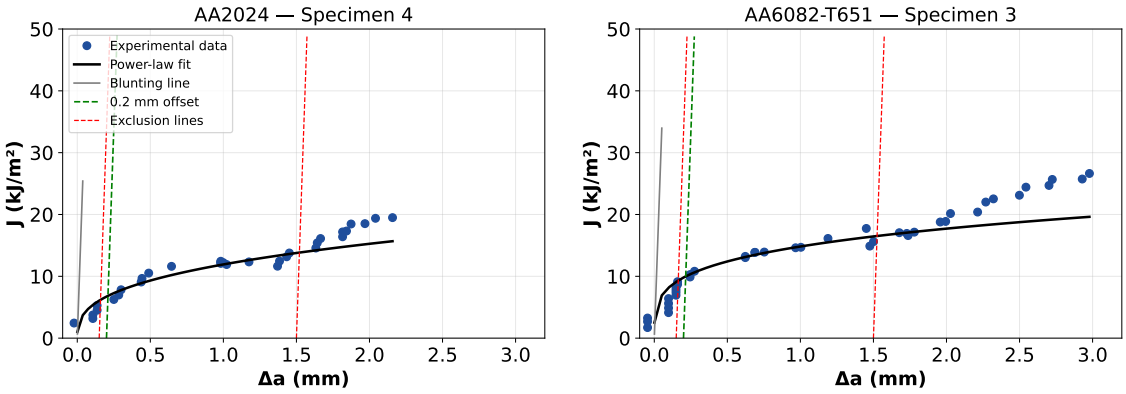


Figure 4.3: *J-R* construction for the remaining two quasi-static specimens, AA2024 (left) and AA6082-T651 (right), following the same procedure as Figure 4.2.

Table 4.2: Quasi-static initiation toughness. K_{JIc} is converted from J_{Ic} with $E = 70$ GPa and $\nu = 0.33$.

Alloy	Specimen	J_{Ic} (kJ/m²)	K_{JIc} (MPa$\sqrt{\text{m}}$)
AA2024	2	8.4	25.7
	3	9.9	27.9
	4	6.8	23.2
	Mean	8.4 ± 1.3	25.6 ± 2.4
AA6082-T651	1	5.7	21.1
	2	7.6	24.5
	3	10.0	28.0
	Mean	7.8 ± 1.8	24.5 ± 3.5

The two alloys give similar initiation toughness, 8.4 against 7.8 kJ/m², a difference smaller than the scatter within each alloy. The scatter is appreciable, with J_{Ic} from 6.8 to 9.9 kJ/m² for the AA2024 and 5.7 to 10.0 kJ/m² for the AA6082-T651. Three specimens is a small sample, and the spread reflects both the natural variability of ductile initiation and the resolution of the optical crack-length method.

4.2.2 Validity Assessment

The qualification of each curve was checked against the requirements of ASTM E1820. The criteria, grouped by type, and the outcome across the six specimens are listed in Table 4.3. Every criterion required for a valid J_{Ic} is met by all specimens.

Table 4.3: ASTM E1820 validity criteria and outcome across the six specimens. The qualification criteria are met by all. The crack-extension capacity is exceeded in most specimens, which limits the valid range of the curve but not the initiation value. The criteria tied to a_{0q} apply only to the unloading-compliance method and are not required here.

Criterion	Clause	Result
Crack front and initial size		
a_0/W within 0.45–0.70	8.5	all pass
Crack-front straightness, a_0 (9 points)	8.5	all pass
Crack-front straightness, a_f (9 points)	8.5	all pass
Extension at each point $\geq 50\%$ of mean	9.1.5.1	all pass
Δa (DIC) agrees with physical a_f	9.1.5.2	all pass
Curve fit		
Number of qualified points ≥ 5	A9.6.6.7	all pass
Point spacing within the exclusion lines	A9.6.4	all pass
Fit exponent $C_2 < 1.0$	A9.9.1	all pass
Size		
Thickness $B > 10 J_Q/\sigma_Y$	A9.10.1	all pass
Ligament $b_0 > 10 J_Q/\sigma_Y$	A9.10.2	all pass
Capacity		
J capacity, $J_{\max} \leq \min(b_0, B)\,\sigma_Y/10$	A9.10	all pass
Δa capacity, $\Delta a_{\max} \leq 0.25\,b_0$	A9.10	5 of 6 exceed
Not required by the direct method (compliance only)		
$\lvert a_0 - a_{0q}\rvert \leq \max(0.01W, 0.5\,\text{mm})$	A9.9.2.1	n/a
Points used for $a_{0q} \geq 8$	A9.9.2.2	n/a
Points between $0.4J_Q$ and $J_Q \geq 3$	A9.9.2.2	n/a
Correlation of a_{0q} fit > 0.96	A9.9.2.2	n/a

The only qualification-independent requirement not met is the crack-extension capacity, $\Delta a_{\max} \leq 0.25\,b_0$, exceeded in five of the six specimens. This is a limit on how far the resistance curve remains valid, not a condition on the initiation toughness. The crack was tracked beyond the capacity of the specimen, so the points at large extension, those climbing above the fit in Figures 4.2 and 4.3, fall outside the valid range and are not used. The initiation J_{Ic}, read at small extension where every criterion is met, is unaffected. The one specimen that stays within capacity, AA6082-T651 specimen 1, gives the cleanest curve, with no points departing from the fit.

A group of criteria in the standard applies only to the unloading-compliance method and is not required here. In compliance testing the crack length is inferred from the specimen stiffness, not measured, so the initial crack length is recovered by regression of the early J-Δa data as a_{0q}. The standard then requires this inferred value to agree with the physically measured a_0 (clause A9.9.2.1), and sets conditions on the regression itself: at least eight points to compute a_{0q}, at least three between $0.4J_Q$ and J_Q, and a correlation coefficient above 0.96 (clause A9.9.2.2). Each of these is conditioned in the standard on the use of an elastic-compliance method, as is the compliance correction of clause A9.3.2, which adjusts the estimated Δa values to obtain an

improved a_{0q}.

In this work the crack length is measured directly from the DIC field, so there is no inferred a_{0q} to validate and no estimated Δa to correct. The role these criteria play in compliance testing, confirming that the crack length recovered from stiffness is sound, is taken here by the direct comparison between the final DIC crack length and the a_f measured on the fracture surface (clause 9.1.5.2), which was within tolerance for all specimens. This is the stronger check, since it validates the measured crack length against the fracture surface itself rather than against a regression of the compliance. The a_{0q} quantities were computed for completeness and meet the limits, but they are not required by the direct method and are not used to qualify the results.

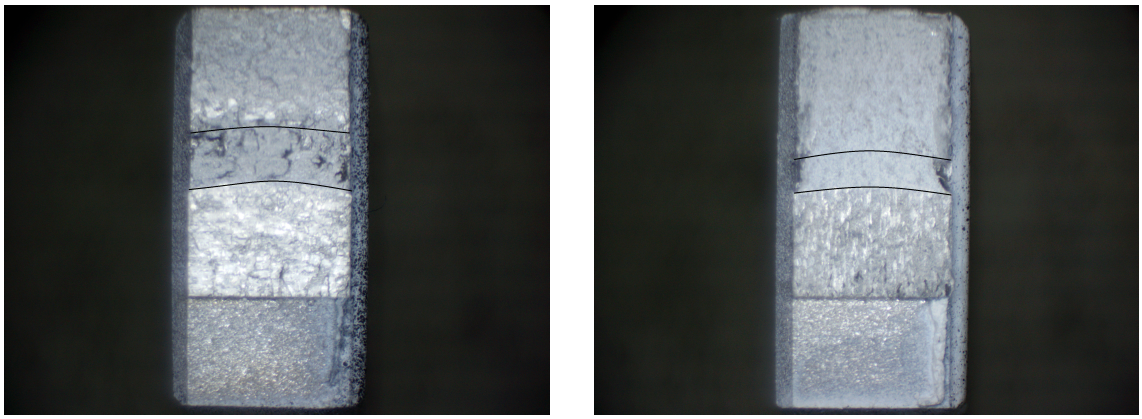
4.2.3 Comparison and Fracture Behaviour

The same specimens could not have given a valid K_{Ic}. As shown in Section 2.3.4, the plane-strain thickness required for a valid LEFM measurement in these alloys is greater than the $B = 7.5$ mm of the SENB specimens. The elastic-plastic J-integral is therefore the correct parameter, and the conversion to $K_{J_{Ic}}$ is reported only to place the results alongside the published K_{Ic} data, not as a valid plane-strain toughness.

The converted values, $K_{J_{Ic}} \approx 26$ MPa$\sqrt{\text{m}}$ for the AA2024 and 25 MPa$\sqrt{\text{m}}$ for the AA6082-T651, sit within the ranges collected in the State of the Art. For AA2024 the naturally aged tempers fall between 22 and 28 MPa$\sqrt{\text{m}}$ (Table 2.2), and for AA6082-T651 the reported values cluster around 23 to 26 MPa$\sqrt{\text{m}}$ [44]. The measured toughness lands in the upper part of the AA2024 range, alongside the naturally aged conditions rather than the peak-aged T6 and T8. The initiation J_{Ic} of the AA2024, 8.4 kJ/m^2, sits within the 5 to 10 kJ/m^2 obtained by converting the plane-strain K_{Ic} values of Table 2.2.

The closeness of the two alloys is consistent with their tensile behaviour, since the effective yield strengths, 338 and 330 MPa, are almost equal. The similarity is less obvious than it looks, because the two fail by the same mechanism acting on different particles. In both alloys the crack advances by void nucleation at coarse intermetallics, followed by growth and coalescence. In the AA2024 the voids nucleate at Al–Cu–Fe and Al–Cu–Mg particles, in the AA6082-T651 at the iron-rich β-Al_5FeSi and α-Al(FeMn)Si phases. With similar strength and similar quasi-static toughness, the rate sensitivity examined in the dynamic tests is what separates the two materials.

Figure 4.4 shows the fracture surface of a representative specimen of each alloy. Two curved lines mark the fatigue pre-crack front a_0 and the final crack front a_f.



(a) (b)

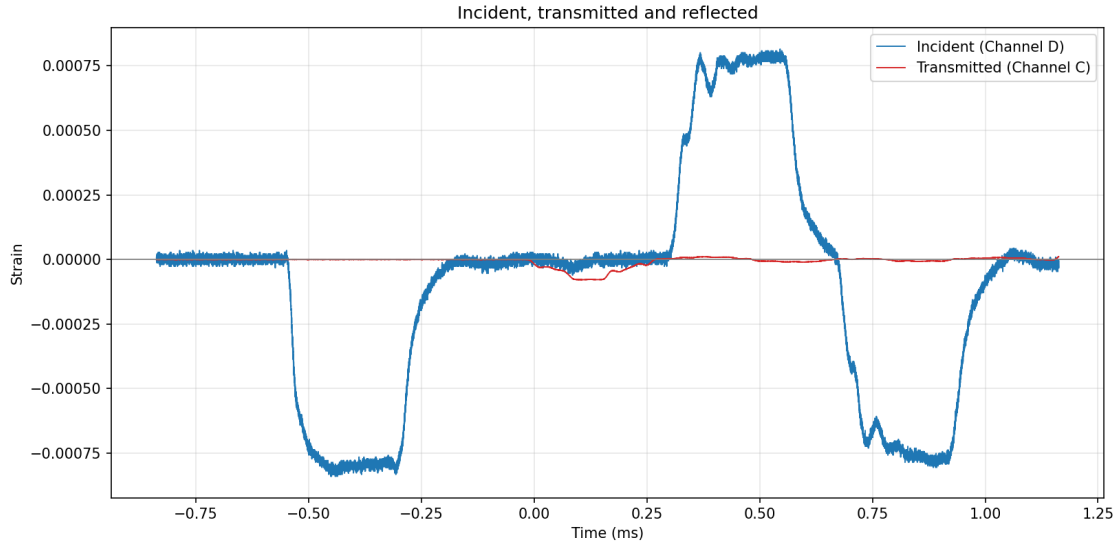
Figure 4.4: Fracture surface of a representative specimen of (a) AA2024 and (b) AA6082-T651. The two curved lines mark the fatigue pre-crack front (a_0) and the final crack front (a_f). Each length was measured at nine equally spaced points along these lines, following ASTM E1820.

4.3 Dynamic Fracture Behaviour

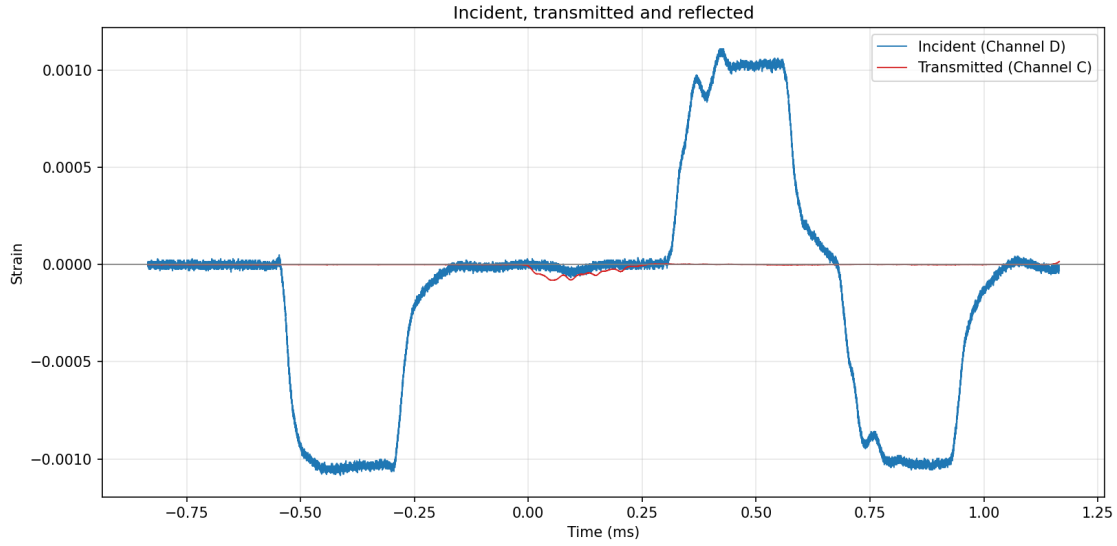
Four specimens of each alloy were tested on the modified split-Hopkinson bar in three-point bending. Unlike the quasi-static tests, where the load is measured directly at the loading point, the load on a dynamic specimen is reconstructed from the bar signals and is only meaningful once the specimen is in force equilibrium. The results are therefore presented in the order that establishes this, with the bar signals and the force balance examined before the toughness is read. The validity window follows, where the measured initiation times are compared against the transition time of Section 2.6.2. The crack-length and CMOD histories, measured from the high-speed images, give the dynamic *J*-*R* curves and the initiation toughness of each specimen.

4.3.1 SHPB Signals and Dynamic Equilibrium

The strain signals recorded on the two bars are shown in Figure 4.5 for one specimen of each alloy, over the full duration of the event. The incident pulse appears first as a compressive wave travelling towards the specimen, followed by the reflected wave returning along the incident bar and the transmitted wave on the support side. The setup is the three-point bending configuration built by Shamchi [60], and the signals follow the pattern expected from it.



(a) AA2024, specimen 1



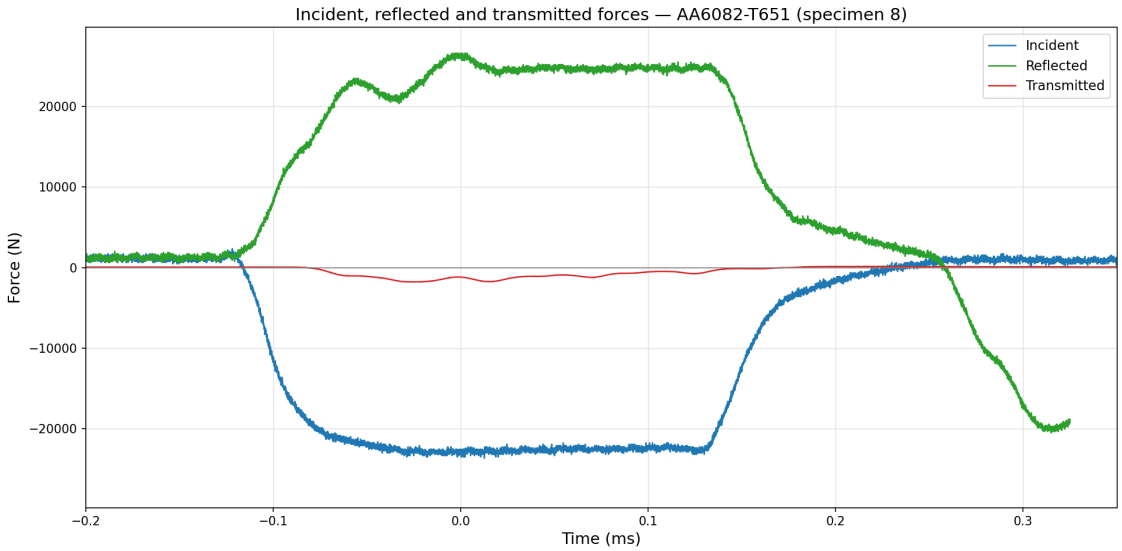
(b) AA6082-T651, specimen 8

Figure 4.5: Incident, reflected and transmitted strain signals over the full event, for one specimen of each alloy.

The same signals, converted to forces and brought to the specimen by the synchronisation of Section 3.8.4, are shown in Figure 4.6 over a window around the loading event. The incident and reflected forces are almost mirror images, one compressive and the other tensile, both of the order of 18 kN, while the transmitted force is far smaller, around 1.5 kN. The specimen reflects most of the incident wave and transmits little, which is the behaviour of a slender bend specimen that offers low resistance to the bar. The load that acts on the cracked ligament is the transmitted force, and it is this force that is taken as P in the J calculation.



(a) AA2024, specimen 1



(b) AA6082-T651, specimen 8

Figure 4.6: Incident, reflected and transmitted forces around the loading event, referred to the specimen.

This relation between the three waves is also why the force balance is judged from the overlap of the signals rather than from a numerical tolerance. The force on the loaded face, $F_1 = F_I + F_R$, is the sum of two large quantities of opposite sign that nearly cancel, and the force on the support side, $F_2 = F_T$, is small. A ratio formed from these two small numbers, each the residue of much larger ones, is dominated by noise and does not give a meaningful measure of equilibrium. Equilibrium is instead ensured by the timing conditions examined in Section 4.3.2.

4.3.2 Validity Window Assessment

The quasi-static formulation applies only if the test meets the conditions set out in Section 3.8.5. Two of them are temporal and concern the loading. Crack initiation must occur after the ring-up time, the interval the specimen needs to reach force equilibrium through internal wave reflections, about 9 µs for the present geometry, and after the transition time of Nakamura, Shih and Freund [46], beyond which the crack-tip field becomes indistinguishable from the quasi-static one, about 71 µs. The transition time is the more demanding of the two, so it sets the temporal limit. The third condition concerns the propagation. The crack speed must stay well below the elastic wave speeds of the material, so that the kinetic energy of the running crack does not add a term the quasi-static J leaves out. The three are checked for every test.

The initiation time is measured as the interval between the contact frame and the initiation frame, taken as the last frame in which the crack is still at a_0, the frame before the crack is first measured beyond a_0. The crack passes a_0 somewhere between this frame and the next, so assigning initiation to the earlier of the two makes the measured interval a lower bound on the true initiation time, which can only be equal to or greater than it. The frame spacing of 12.5 µs sets the resolution, and the uncertainty is one-sided, towards longer times.

The crack speed is measured from the crack-length history, as the advance between successive frames. The Rayleigh wave speed of aluminium, about 2900 m/s, is the upper bound on how fast a crack can run, and the kinetic contribution to J becomes significant only as the crack speed approaches an appreciable fraction of it.

The incident rise time, the measured initiation time, and the peak crack speed of each specimen are listed in Table 4.4. The rise time is the interval over which the incident force climbs from 10% to 90% of its peak. The two cutoffs avoid the slow, noisy ends of the pulse, where the onset and the approach to the peak are poorly defined, and measure the central part of the rise. This interval is much longer than the ring-up time in every test, so the specimen has time to reach equilibrium well before the peak load is applied.

Table 4.4: Incident rise time, measured initiation time, and peak crack speed for the dynamic specimens. The initiation time is compared against the transition time, $t_T \approx 71$ µs, and the peak crack speed against the Rayleigh wave speed of aluminium, $c_R \approx 2900$ m/s.

Specimen	Rise time (µs)	t_{init} (µs)	Peak speed (m/s)	Peak / c_R (%)
AA2024, specimen 1	43.8	75.0	30	1.0
AA2024, specimen 2	42.1	62.5	57	2.0
AA2024, specimen 3	63.2	75.0	48	1.7
AA2024, specimen 4	50.5	75.0	52	1.8
AA6082-T651, specimen 4	96.7	75.0	39	1.3
AA6082-T651, specimen 6	38.3	75.0	35	1.2
AA6082-T651, specimen 7	68.2	75.0	36	1.2
AA6082-T651, specimen 8	51.7	75.0	41	1.4

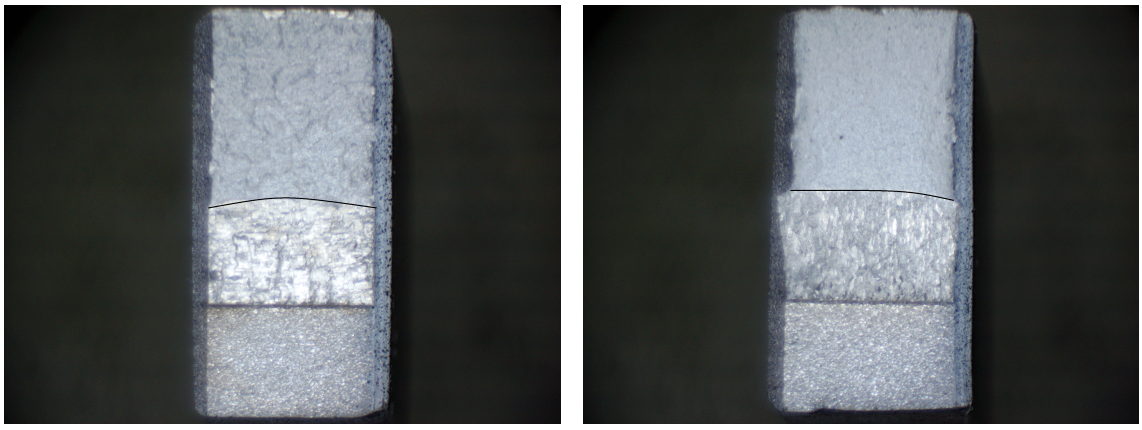
The rise time varies between the two batches, which follows from the state of the copper pulse shaper. It was more worn during the AA2024 tests and damped the pulse less. Seven of the eight specimens initiate at 75 µs, above the transition time, and satisfy the temporal condition. The exception is AA2024 specimen 2 which initiates at a measured 62.5 µs, below the 71 µs limit. Since the measurement is a lower bound with a one-sided uncertainty of one frame, the true initiation time of this specimen can be as high as 75 µs, which would place it above the transition time. The condition can neither be confirmed nor excluded for this specimen, and its result is reported in the following sections with this reservation. The peak crack speed stays below 2% of the Rayleigh wave speed in every specimen, so the kinetic contribution to J is negligible and the load is used without inertial correction.

4.3.3 Crack-Length and CMOD Histories

The initial crack length of each specimen was measured on the fracture surface after the test, following the nine-point method of ASTM E1820, the same procedure used for the quasi-static specimens in Section 3.7.2. The crack front is measured at nine equally spaced positions across the thickness, and the initial crack length is the weighted average of the nine readings, with the two surface points taken at half weight and the seven interior points at full weight. This average is added to the machined notch length to give a_0. The values are listed in Table 4.5, and the fracture surfaces from which they were read are shown in Figure 4.7.

Table 4.5: Initial crack length a_0 of each specimen, from the nine-point method of ASTM E1820.

Specimen	a_0 (mm)
AA2024, specimen 1	7.829
AA2024, specimen 2	7.918
AA2024, specimen 3	8.001
AA2024, specimen 4	8.001
AA6082-T651, specimen 4	8.053
AA6082-T651, specimen 6	7.880
AA6082-T651, specimen 7	7.801
AA6082-T651, specimen 8	8.001

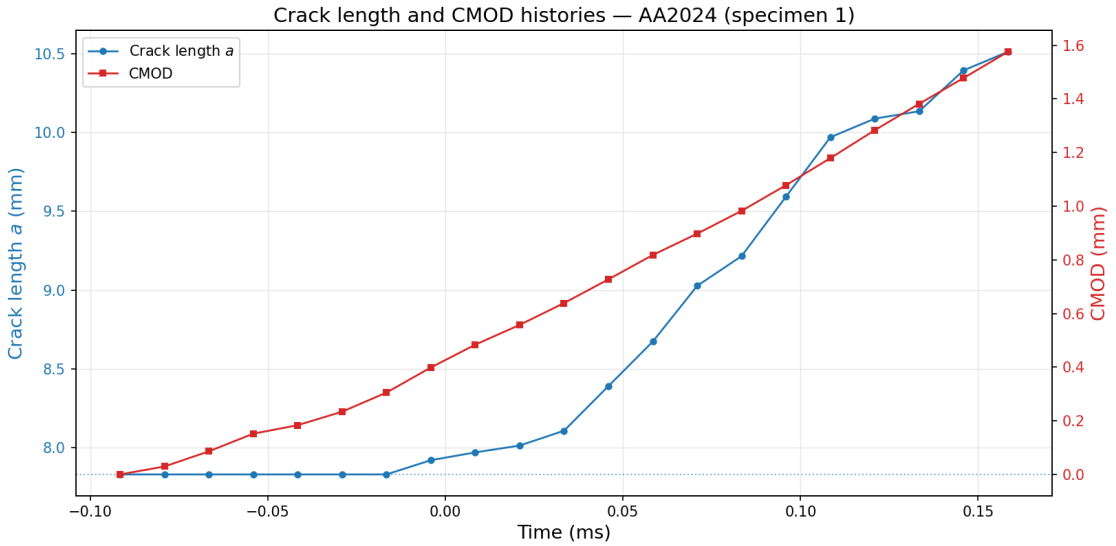


(a) AA2024, specimen 1 (b) AA6082-T651, specimen 8

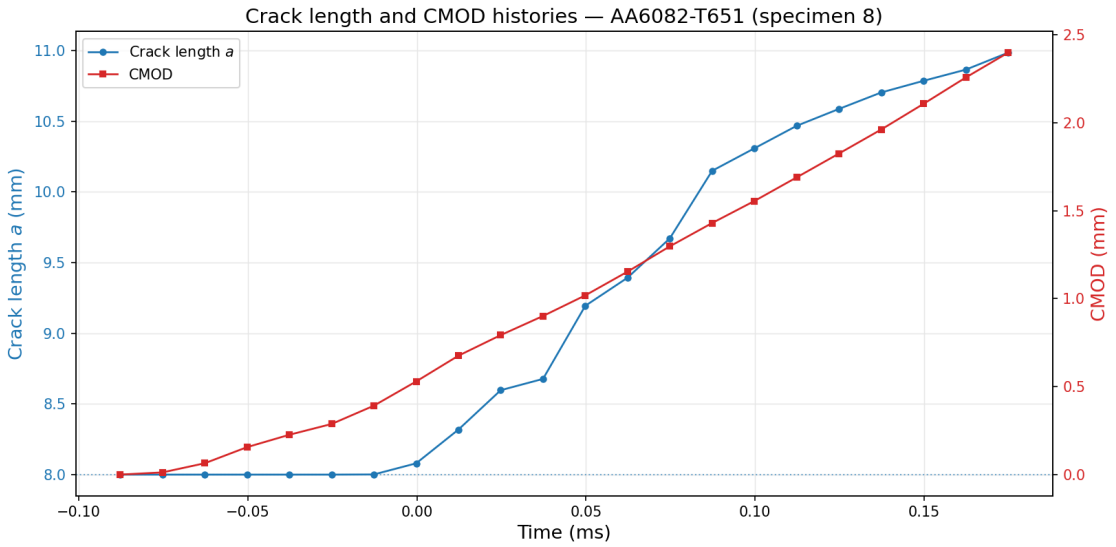
Figure 4.7: Fracture surfaces showing the fatigue pre-crack front, from which the initial crack length was measured by the nine-point method.

The crack length and the CMOD were measured through the test from the DIC fields, as described in Section 3.4.5. Their histories are shown in Figure 4.8 for one specimen of each alloy, over the loading window. The crack growth reported here covers only the incident pulse. After the pulse ends the specimen keeps moving under its own inertia and eventually breaks, but that stage is not analysed, so the final crack length in the figure is the length reached at the end of the pulse and not the full width.

The two histories show the expected sequence. The CMOD opens from the moment the load enters the specimen and rises smoothly through the event. The crack length stays at a_0 through the early part of the loading and begins to grow only later, once the crack initiates, after which it advances steadily to the end of the analysed window.



(a) AA2024, specimen 1



(b) AA6082-T651, specimen 8

Figure 4.8: Crack-length and CMOD histories over the loading window, for one specimen of each alloy.

4.3.4 Dynamic J-R Curves

The dynamic *J*-*R* curves were built by the same method used for the quasi-static tests in Section 4.2.1. The crack length is measured optically through the test, J is computed point by point from the transmitted force and the CMOD following ASTM E1820, and the initiation value is read at the first measured crack growth rather than from a 0.2 mm offset. The offset construction is not used here. It requires a density of points near the origin, in the blunting region, that the frame rate does not provide, so the *J*-*R* curve is reported together with the J at initiation taken directly from the crack measurement.

The dynamic *J*-*R* curves of all eight specimens are shown in Figures 4.9 and 4.10. Each plot shows the loading points at $\Delta a = 0$, where J rises while the crack is still at a_0, the propagation points, the initiation point, and the blunting and exclusion lines. The initiation point sits at $a = a_0$.

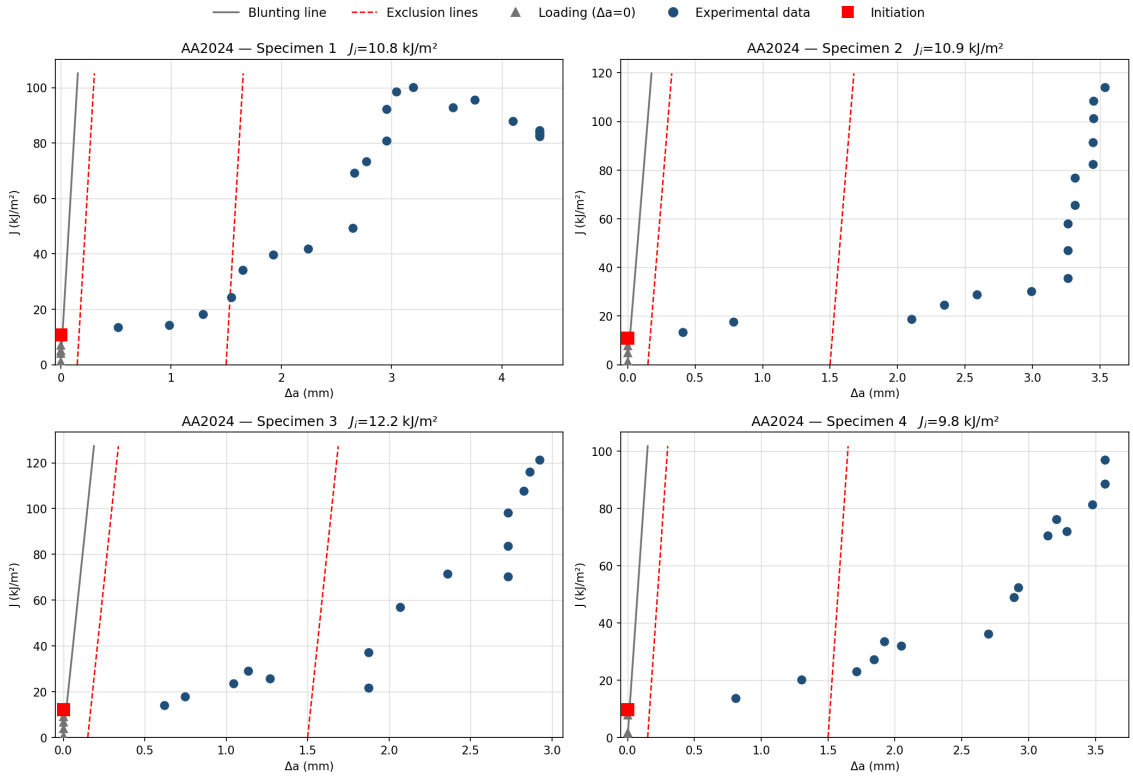


Figure 4.9: Dynamic *J*-*R* curves for the four AA2024 specimens. Each plot shows the loading points at $\Delta a = 0$, the propagation points, the initiation point, and the blunting and exclusion lines. Specimen 2 is marked as marginal, since its initiation time falls within the uncertainty of the transition time, Section 4.3.2.

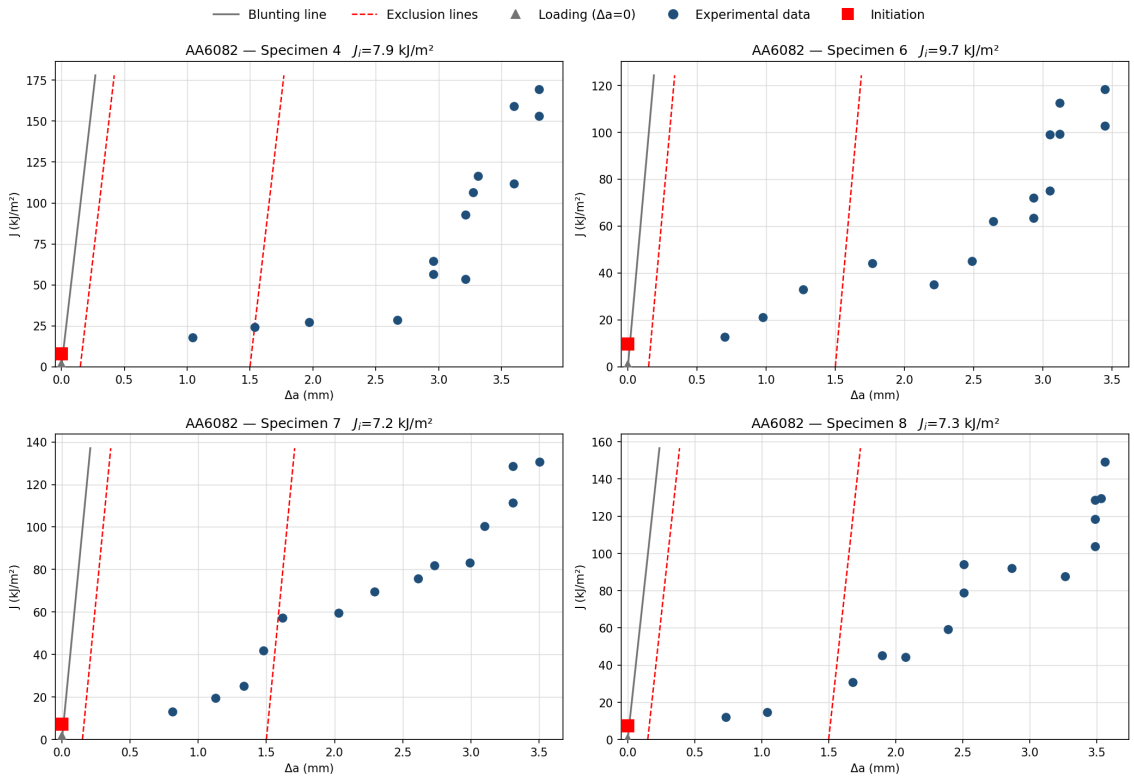


Figure 4.10: Dynamic J-R curves for the four AA6082-T651 specimens, following the same layout as Figure 4.9.

The initiation values of all eight specimens are listed in Table 4.6, with the initiation toughness expressed both as J_i and as the equivalent K_{Ji}. The AA2024 specimens give a mean J_i of 10.9 ± 1.0 kJ/m^2 against 8.0 ± 1.2 kJ/m^2 for the AA6082-T651, and AA2024 is the tougher of the two in every specimen, not only on average. The scatter is comparable in the two alloys, with J_i from 9.8 to 12.2 kJ/m^2 for the AA2024 and from 7.0 to 9.7 kJ/m^2 for the AA6082-T651, where specimen 6 stands above the other three. AA2024 specimen 2 is included with the reservation on its validity noted in Section 4.3.2. The comparison with the quasi-static baseline and the role of loading rate are taken up in Section 4.5.

Table 4.6: Dynamic initiation toughness. K_{Ji} is converted from J_i with $E = 70$ GPa and $\nu = 0.33$.

Alloy	Specimen	J_i (kJ/m²)	K_{Ji} (MPa$\sqrt{\text{m}}$)
AA2024	1	10.8	29.1
	2	10.9	29.3
	3	12.2	31.0
	4	9.8	27.8
	Mean	10.9 ± 1.0	29.3 ± 1.3
AA6082-T651	4	7.9	24.9
	6	9.7	27.6
	7	7.0	23.5
	8	7.3	23.9
	Mean	8.0 ± 1.2	25.0 ± 1.9

4.4 Setup Validation against the Quasi-Static Baseline

The reasoning set out in Section 3.1 makes the AA6082-T651 the reference for checking the setup. Its low strain rate sensitivity, documented by Chen et al. [17], means its dynamic toughness is expected to stay close to the quasi-static value, so a match between the two indicates that the setup and the data reduction are sound before any rate effect is read as material behaviour. This validation is presented in two steps. The commissioning carried out to reach the working configuration is described first, and the dynamic toughness of the AA6082-T651 is then compared against its quasi-static baseline.

4.4.1 Setup Development

The three-point bending SHPB configuration built by Shamchi [60] was used here for fracture testing, which it had not been applied to before, and it was commissioned for this purpose before the reported tests were run. The first experiments did not give the signals expected from the quasi-static behaviour and the literature, and the setup was adjusted iteratively until the signals made sense. About four of these trials used specimens; the rest were run without a specimen, to save material, since the expected shape of the signal was already known.

The main symptom was a tensile spike on the incident signal, before the compressive pulse, where a well-bonded gauge should read only compression. Figure 4.11 shows one such trace. Several causes were considered and addressed in turn. A misalignment between the striker and the incident bar, with off-centre contact, could bend the bar and produce tension at the incident gauge, so the position of the pneumatic supports and the striker travel were adjusted. The end-stop spring of the transmitted bar jammed and behaved rigidly, and was replaced. The teflon guides of the striker rubbed against the surrounding tube, and were polished to reduce friction. The dominant cause was found later to be a debonded strain gauge on the incident bar, which produced

the spurious tensile spike. Once the gauge was replaced, the signal recovered its expected shape. Some of the earlier adjustments refined the setup but were not needed to remove the main artefact.

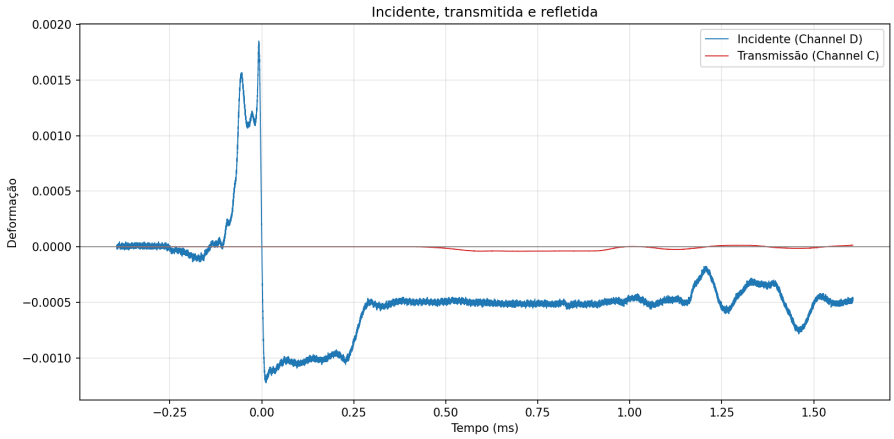


Figure 4.11: Incident and transmitted strains from a commissioning test, showing the spurious tensile spike on the incident signal that was traced to a debonded strain gauge.

The pulse shaper was chosen in the same process. Without a shaper the incident pulse rose too sharply, which is poor for reaching force equilibrium. A rubber shaper degraded too quickly and had to be replaced every test. A copper shaper gave a stable, repeatable pulse and was durable, and was adopted for all reported tests.

Two AA6082-T651 specimens were tested with a larger punch at the end of the incident bar and were discarded. The punch was only fitted into the bar, with no feature to restrain its radial and axial movement relative to it, so it sat with clearance rather than being locked in place. This clearance let it move relative to the bar, and its inertia then kept it moving against the specimen even after the incident bar had stopped, which lengthened the pulse delivered to the specimen. Had it been locked, it would have moved with the bar and stopped with it, without extending the pulse. The load on the specimen was therefore longer than its passage at the incident gauge suggested, and this offset between what the gauge recorded and what the specimen experienced distorted the synchronisation. These tests were not used.

4.4.2 Comparison with the Quasi-Static Baseline

The dynamic initiation toughness of the AA6082-T651 is 8.0 ± 1.2 kJ/m^2, against 7.8 ± 1.8 kJ/m^2 under quasi-static loading, and the equivalent K_{Ji} is 25.0 ± 1.9 MPa$\sqrt{\text{m}}$ against 24.5 ± 3.5 MPa$\sqrt{\text{m}}$. Both measures fall within their scatter bands, and the difference between the two regimes is far smaller than the spread within either set. The dynamic result reproduces the quasi-static one without a systematic shift.

This is the outcome expected for this alloy. Chen et al. [17] tested AA6082-T6 in tension from 10^{-4} to 3400 s^{-1} and, alongside the stress-strain response, characterised the ductile fracture behaviour through the stress triaxiality and the equivalent plastic strain at fracture, which they

used to calibrate a Johnson-Cook fracture model. Both the flow stress and the fracture behaviour were found to be weakly rate dependent, with the slight sensitivity seen at intermediate rates counteracted by adiabatic heating at high rates, so that the dynamic response falls back onto the quasi-static one. A near coincidence of quasi-static and dynamic curves for this alloy has been reported by others on the same basis. The toughness measured here behaves the same way, with the dynamic and quasi-static values falling on top of each other, so the agreement reflects the material rather than a masking effect of the setup.

The comparison therefore serves its purpose. Because the reference alloy is rate-insensitive in both flow and fracture by independent evidence, the match between its dynamic and quasi-static toughness isolates the performance of the setup and the data reduction from any real rate effect. The setup recovers a known value without bias, so the rate effect measured on the AA2024, examined in Section 4.5, can be attributed to the material and not to the method.

4.5 Strain-Rate Effects on Fracture Toughness

With the setup validated on the AA6082-T651, the difference between the quasi-static and dynamic results on the AA2024 can be read as a rate effect. This section compares the two regimes for both alloys, at the point where the comparison is sound, the onset of crack growth.

The two regimes report the initiation toughness through slightly different constructions. In the quasi-static tests J_{Ic} is read at the intersection of the power-law fit with the 0.2 mm offset, as the standard prescribes. In the dynamic tests the offset construction cannot be used, because the frame rate leaves too few points in the blunting region to define the fit, so the initiation value is taken directly as the J at the last frame before the crack grows beyond a_0. The two are therefore not the same quantity by definition, and the comparison is read with that in mind. Both, however, mark the onset of crack growth, which is what makes the comparison meaningful.

The initiation values of the two regimes are shown in Figure 4.12. For the AA2024 the mean rises from 8.4 ± 1.3 kJ/m^2 under quasi-static loading to 10.9 ± 1.0 kJ/m^2 under dynamic loading, an increase of about 30%. The scatter bands overlap slightly, so the result is a clear trend rather than a sharp separation, but every dynamic specimen sits at or above the quasi-static range. For the AA6082-T651 the mean is unchanged within scatter, 7.8 ± 1.8 kJ/m^2 against 8.0 ± 1.2 kJ/m^2. The contrast between the two alloys is the main result. The AA2024 gains toughness with rate while the AA6082-T651 does not.

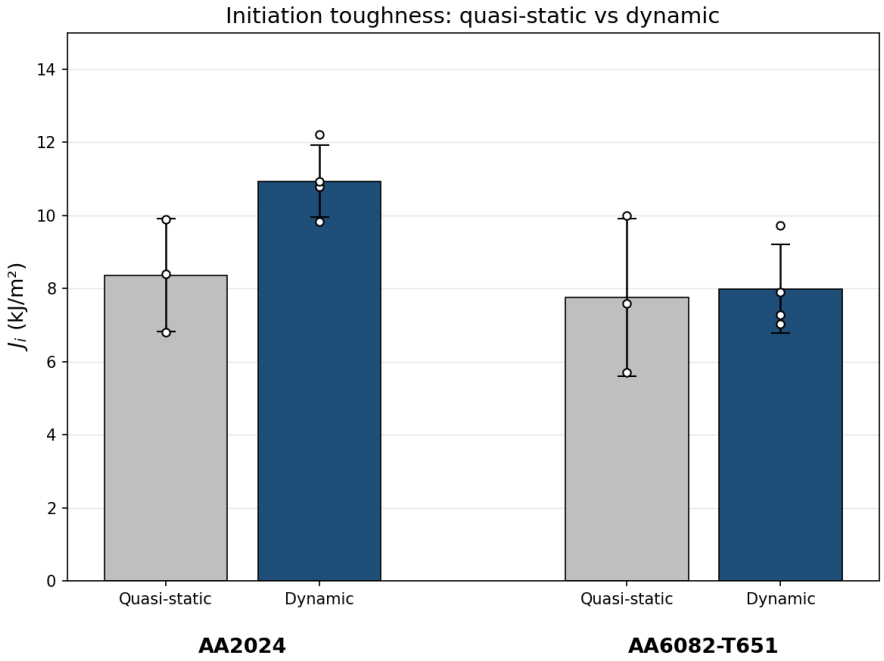


Figure 4.12: Initiation toughness under quasi-static and dynamic loading for the two alloys. Bars are the mean of each set, error bars the standard deviation, and open circles the individual specimens.

The dynamic loading rate is described by $\dot{K}$, the rate at which the stress intensity climbs to initiation, estimated as K_{Ji} divided by the initiation time. With K_{Ji} near 25 to 30 MPa$\sqrt{\text{m}}$ reached in about 75 µs, $\dot{K}$ is of the order of 10^5 MPa$\sqrt{\text{m}}$/s. The rate effect on the AA2024 is measured across this range.

The resistance behaviour of the two regimes is shown in Figures 4.13 and 4.14, with the quasi-static fit drawn over its qualified range and the dynamic points plotted directly. Inside the exclusion lines, where the analysis is valid, the two curves agree closely for the AA6082-T651, and the dynamic points sit slightly above the quasi-static fit for the AA2024, consistent with the initiation values. Beyond the outer exclusion line the dynamic points climb steeply away from the quasi-static curve. This part is outside the qualified range, where the J calculation no longer holds, and it is not read as a rate effect. The exclusion lines mark the limit of the comparison.

The visual comparison of the curves can be made quantitative. For each dynamic specimen, the J at its first measured propagation point is compared with the mean of the three quasi-static power-law fits of the same alloy, evaluated at the same crack extension. This compares like with like, the J at a common Δa inside the qualified range, and avoids the different initiation constructions of the two regimes. The values are listed in Table 4.7.

Table 4.7: Dynamic J at the first propagation point compared with the mean quasi-static J at the same crack extension. The quasi-static value is the mean of the three power-law fits of the alloy, with its standard deviation.

Specimen	Δa (mm)	J_{dyn} (kJ/m^2)	J_{qs} (kJ/m^2)	Ratio
AA2024, specimen 1	0.52	13.5	11.4 ± 2.1	1.18
AA2024, specimen 2	0.41	13.4	10.5 ± 1.9	1.27
AA2024, specimen 3	0.62	14.2	12.1 ± 2.2	1.17
AA2024, specimen 4	0.81	13.7	13.3 ± 2.5	1.03
AA6082-T651, specimen 4	1.04	17.8	14.9 ± 1.0	1.20
AA6082-T651, specimen 6	0.70	12.7	12.6 ± 0.9	1.01
AA6082-T651, specimen 7	0.81	13.2	13.3 ± 0.7	0.99
AA6082-T651, specimen 8	0.73	12.1	12.8 ± 0.8	0.95

The comparison confirms the rate effect seen at initiation. The AA2024 dynamic points lie above the quasi-static mean, by 17 to 27% for three of the four specimens. Specimen 4 is the exception, close to the quasi-static value, and it is also the specimen with the lowest initiation toughness and the largest first crack extension, at 0.81 mm. For the AA6082-T651 the dynamic and quasi-static values coincide, three of the four ratios sitting within 5% of unity. Specimen 4 of this alloy shows a 20% rise, but its first propagation point falls at 1.04 mm, well beyond the others and into the region where the two methods start to diverge, so this value is not read as a rate effect.

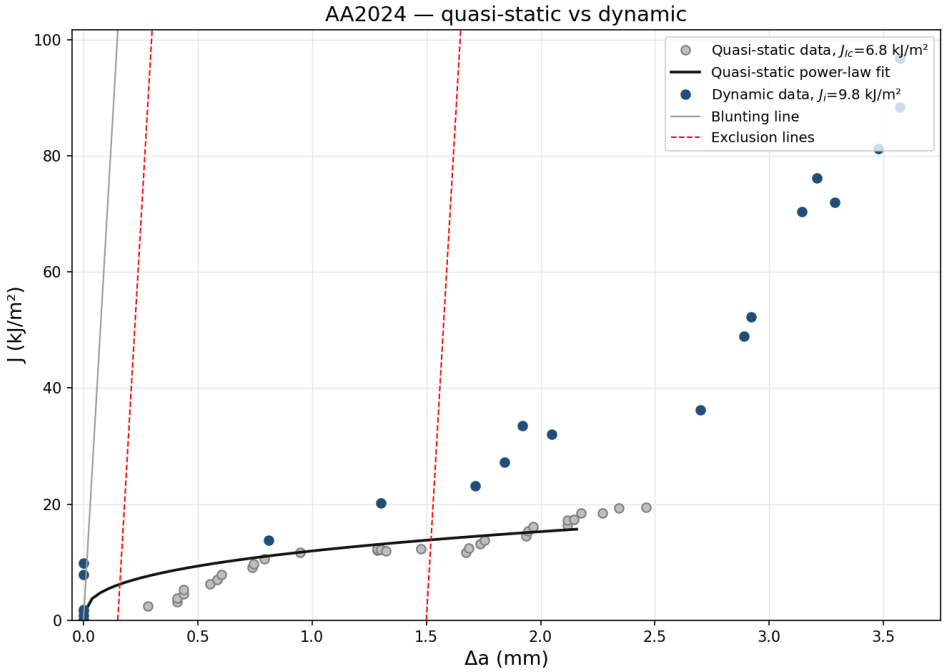


Figure 4.13: AA2024 resistance behaviour under quasi-static and dynamic loading. The quasi-static fit is shown over its qualified range and the dynamic points directly, with the blunting and exclusion lines for reference.

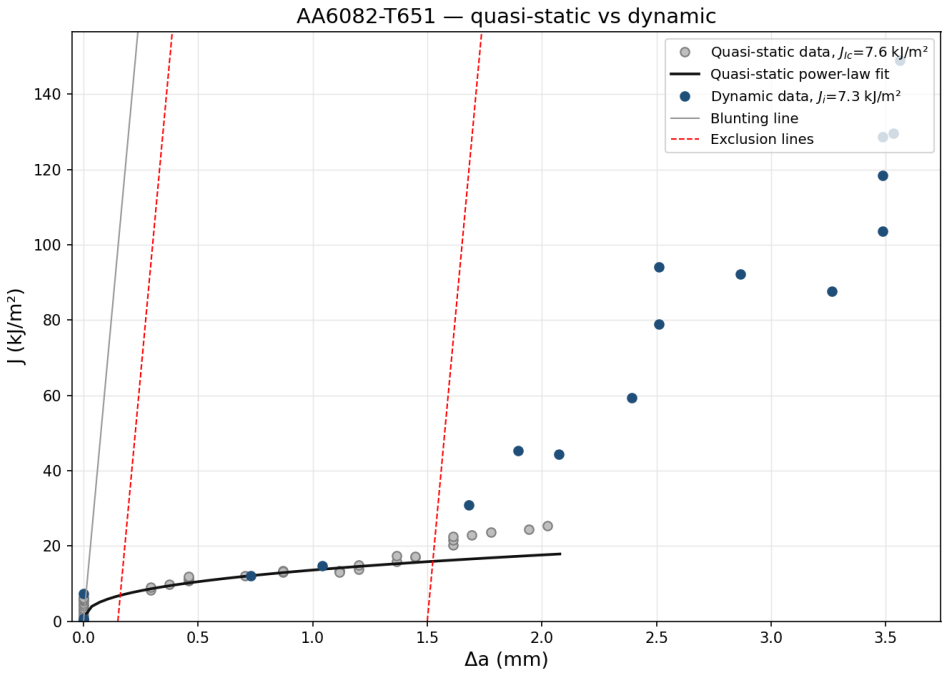


Figure 4.14: AA6082-T651 resistance behaviour under quasi-static and dynamic loading, in the same layout as Figure 4.13.

The contrast between the two alloys is consistent with the picture in the literature and with

the alloy systems. The AA6082-T651 is an Al-Mg-Si alloy whose low rate sensitivity in flow and fracture is documented by Chen et al. [17], and its toughness behaves the same way, unchanged between the two regimes. The AA2024 is an Al-Cu alloy, and the rise in its initiation toughness with rate agrees with Xing et al. [70], who measured an increase in the dynamic toughness of AA2024 in three-point bending with a drop-tower setup. Their loading rates stayed well below those of the Split Hopkinson bar, so the present result extends the same trend to the much higher rates of the SHPB regime. The result supports the view that rate effects on the fracture toughness of aluminium alloys are real but alloy-dependent, so quasi-static data cannot be assumed to hold at crash rates without checking the specific alloy.

The fractographic evidence needed to identify the mechanism behind this contrast was not collected in this work, so the explanation remains at the level of hypothesis, framed by the physics reviewed in Sections 2.2 and 2.4. The rise measured on the AA2024 is consistent with rate hardening of the matrix. The flow stress ahead of the crack tip increases with strain rate, more plastic work is dissipated before the local strain at the intermetallic particles reaches the level needed for void nucleation, and the initiation toughness rises. Enhanced crack-tip blunting from local adiabatic heating, which softens the material in the fracture process zone without destabilising it, would act in the same direction. In the AA6082-T651 the flow stress is nearly rate-insensitive, with the slight sensitivity offset by adiabatic softening [17], so neither term changes appreciably between regimes and the toughness follows the quasi-static value. The opposite outcome, a toughness drop through strain localisation into adiabatic shear bands, Section 2.4.2, is not reflected in the measured values, since neither alloy lost toughness with rate. Distinguishing between these contributions requires fractographic comparison of the quasi-static and dynamic fracture surfaces, which is left to future work.

The magnitude of the rise should be read with the method in mind. The quasi-static value is J_{Ic} from the offset construction and the dynamic value is the J at initiation, and Pandouria and Tiwari [51] showed that the measured toughness is sensitive to how initiation is tracked. The comparison here is kept at initiation for that reason, where both regimes measure the same event. Within that limit, the AA2024 gains toughness with rate while the AA6082-T651 does not, and the AA6082-T651 acts as the rate-insensitive reference against which the rate sensitivity of the AA2024 stands out.

4.6 Methodological Discussion

This section reviews the results in turn and the limits within which they stand. Both alloys were tested under quasi-static and dynamic loading, with the same specimen geometry and the same reduction to ASTM E1820, so any difference in the measured toughness follows from the material or the loading rate. The quasi-static tests gave qualified J_{Ic} values, the dynamic tests gave initiation toughness and resistance curves, and the comparison isolated a rate effect on the AA2024 that the AA6082-T651 did not show.

The tensile tests provided the flow properties needed for the fracture analysis. The temper of the AA2024 was unknown, so its yield and ultimate strengths were measured in tension. Five of the nine specimens gave valid curves, and these grouped closely. The yield strength was 287 ± 5 MPa and the ultimate strength 390 ± 4 MPa. The modulus was less reliable. DIC returned 59 GPa on the mini specimens, well below the expected value. This is likely an artefact of the small elastic strain range, where the DIC noise is a large fraction of the measured strain. The reference value of 70 GPa was used where the modulus enters the fracture calculations. The effective yield strength comes from the strength plateau and not from the elastic slope, so the poor modulus does not affect it.

The quasi-static curves met the validity requirements of ASTM E1820. All six specimens satisfied every criterion for a qualified J_{Ic}. The scatter within each alloy is appreciable. It comes from the natural variability of ductile initiation and from the resolution of the optical crack-length method. It does not affect the qualification, and the values enter the comparison as valid measurements.

The dynamic tests gave a consistent set of results across the eight specimens. The AA2024 was the tougher alloy in every specimen. The two alloys separated more clearly than under quasi-static loading. The initiation value was read as the J at the last frame before the crack grew past a_0. The offset construction was not used, because the frame rate leaves too few points in the blunting region to define the fit. This is the main effect of the frame rate on the dynamic reduction, and it makes the dynamic resistance curve coarser than the quasi-static one.

The two regimes were compared inside the qualified range, both at initiation and at a common crack extension. The second comparison reads the dynamic J at the first propagation point against the mean quasi-static fit at the same Δa, which avoids the different initiation constructions of the two regimes. Both comparisons give the same result. The AA2024 sits above the quasi-static values and the AA6082-T651 coincides with them. The valid range is narrow, since the J calculation no longer applies once the crack grows beyond the qualified window, and the dynamic curve holds few points inside it. The comparison was kept within that window.

The material characterisation limits how far the toughness values can be generalised. The temper of the AA2024 plate and its orientation to the rolling direction were not known. Toughness is strongly anisotropic and depends on temper. The values reported here belong to the material as received and cannot be assigned to a specific condition. For a defined temper and orientation they would differ. The wide published range for AA2024 in naturally aged tempers, 5 to 10 kJ/m^2, is consistent with this. The strength changes little with orientation, so this limitation affects the toughness far more than the tensile data.

The method gave the toughness of both alloys in both regimes. The results were validated against a rate-insensitive reference and agree with the literature. Two limits remain: the frame rate, which sets how much of the resistance curve can be compared and the material characterisation, which sets how far the values can be generalised. Both are addressed in Chapter 5.

Chapter 5

Conclusions and Future Work

5.1 Conclusions

This work measured the fracture toughness of AA2024 and AA6082-T651 under quasi-static and dynamic loading, with one specimen geometry and one reduction to ASTM E1820. The objectives set out in Section 1.3 were met, within the limits discussed in Section 4.6: the initiation of one dynamic specimen falls within the uncertainty of the transition time, and the qualified range of the dynamic curves is narrow.

An experimental methodology was defined for both regimes. It covers the SENB geometry, the ASTM E1820 reduction, the quasi-static and SHPB three-point bending setups, and the instrumentation. Specimens of both alloys were manufactured, fatigue pre-cracked, and tested.

The quasi-static toughness was measured as a J-resistance curve. The qualified J_{Ic} was 8.4 ± 1.3 kJ/m^2 for the AA2024 and 7.8 ± 1.8 kJ/m^2 for the AA6082-T651. The dynamic toughness was measured on the SHPB adapted for three-point bending, at loading rates of the order of 10^5 MPa$\sqrt{\text{m}}$/s. The dynamic initiation toughness was 10.9 ± 1.0 kJ/m^2 for the AA2024 and 8.0 ± 1.2 kJ/m^2 for the AA6082-T651.

Digital Image Correlation tracked the crack in both regimes. It replaced the mechanical methods that cannot follow an event lasting a few hundred microseconds, and it provided the crack length used in the J reduction.

The rate effect was assessed by comparing the two regimes for each alloy, at initiation and at a common crack extension. Under dynamic loading the AA2024 resistance stayed above the quasi-static one at the same crack extension, and the initiation values rose in the same direction. The AA6082-T651 was unchanged within scatter by both measures. The rate effect is real but depends on the alloy, and the AA6082-T651 served as a rate-insensitive reference that confirmed the setup before the AA2024 result was read as material behaviour.

The dynamic J-R curves were built through a procedure consistent with ASTM E1820 adapted to the SHPB. Published dynamic data for these alloys are limited to point values of K_{Id} or come from smooth specimens, so the resistance curves reported here fill a gap for AA2024 and AA6082-T651 under impact loading.

5.2 Future Work

The dynamic tests covered a single nominal rate. Testing at several strain rates would map the dependence of the toughness on rate, rather than establishing it at one point, and would show whether the AA2024 continues to gain toughness as the rate rises.

The frame rate limited the number of points in the qualified window. A higher acquisition rate would give a finer resistance curve, provided the image resolution stays high enough for the DIC to track the crack. The two requirements compete, and finding the acquisition rate that balances them is worth a dedicated study.

The temper and orientation of the AA2024 plate were not known. Repeating the tests on material with a defined temper and a known orientation to the rolling direction would give toughness values that can be compared directly with the literature and assigned to a specific condition.

SEM fractography of the tested specimens, comparing dimple size and distribution between the quasi-static and dynamic surfaces of each alloy, would test the hypotheses advanced in Section 4.5 and identify the mechanism behind the rate sensitivity of the AA2024.

The J-integral was evaluated here from the force and displacement records. Computing it from the contour integral definition with a numerical model, as Pandouria et al. [51] did for AA2014-T6, would give an independent check on the measured values and would extend the analysis into the region where the experimental reduction no longer qualifies.

A numerical model would complete the work. A model based on the Johnson-Cook law [38], validated against the experimental results reported here, would allow the dynamic fracture of these alloys to be predicted in the component geometries used for battery enclosures, which is the setting that motivated the study.

References

[1] T. L. Anderson. “Crack tip parameters for large scale yielding and low constraint configurations”. In: *International Journal of Fracture* 41 (1989), pp. 79–104.

[2] T. L. Anderson. *Fracture Mechanics: Fundamentals and Applications*. 4th. Boca Raton, FL: CRC Press, 2017.

[3] Ansys Granta. *Granta EduPack*. Materials education software, available under FEUP institutional licence. 2024. URL: https://www.ansys.com/products/materials/granta-edupack.

[4] Shashank Arora, Weixiang Shen, and Ajay Kapoor. “Review of mechanical design and strategic placement technique of a robust battery pack for electric vehicles”. In: *Renewable and Sustainable Energy Reviews* 60 (2016), pp. 1319–1331. DOI: 10.1016/j.rser.2016.03.013.

[5] Michael F. Ashby. *Materials Selection in Mechanical Design*. 5th. Oxford: Butterworth-Heinemann, 2017. ISBN: 978-0-08-100586-9.

[6] ASM International, ed. *ASM Handbook, Volume 19: Fatigue and Fracture*. Materials Park, OH: ASM International, 1996. ISBN: 978-0-87170-385-9.

[7] ASM International. *ASM Handbook, Volume 2: Properties and Selection: Nonferrous Alloys and Special-Purpose Materials*. Materials Park, OH: ASM International, 1990. ISBN: 978-0-87170-378-1.

[8] ASM International. *ASM Handbook, Volume 2: Properties and Selection: Nonferrous Alloys and Special-Purpose Materials*. Materials Park, OH: ASM International, 1990.

[9] ASTM International. *ASTM E1820-23: Standard Test Method for Measurement of Fracture Toughness*. West Conshohocken, PA, 2023. DOI: 10.1520/E1820-23.

[10] ASTM International. *ASTM E399: Standard Test Method for Linear-Elastic Plane-Strain Fracture Toughness of Metallic Materials*. West Conshohocken, PA: ASTM International, 2022. DOI: 10.1520/E0399-22.

[11] ASTM International. *Standard Test Methods for Tension Testing of Metallic Materials*. West Conshohocken, PA, USA: ASTM International, 2021. DOI: 10.1520/E0008_E0008M-21.

[12] A. Boag et al. “How complex is the microstructure of AA2024-T3?” In: *Corrosion Science* 51.8 (2009), pp. 1565–1568. DOI: 10.1016/j.corsci.2009.05.001.

[13] R. J. Bucci, G. Nordmark, and E. A. Starke. “Selecting Aluminum Alloys to Resist Failure by Fracture Mechanisms”. In: *ASM Handbook, Volume 19: Fatigue and Fracture*. Materials Park, OH: ASM International, 1996, pp. 771–812. DOI: 10.1361/asmhba0002406.

[14] Pedro Ponces Camanho. *Fracture Mechanics and Fatigue*. Lecture Notes, Faculdade de Engenharia da Universidade do Porto (FEUP). Apontamentos das aulas. 2024.

[15] Vishal Chaudhari et al. “A Critical Review on Lightweight Design of Battery Pack Enclosure for Electric Vehicles”. In: *Automotive Experiences* 4.2 (2021).

[16] W. Chen and B. Song. *Split Hopkinson (Kolsky) Bar: Design, Testing and Applications*. Springer Science & Business Media, 2010.

[17] X. Chen et al. “Flow and fracture behavior of aluminum alloy 6082-T6 at different tensile strain rates and triaxialities”. In: *PLoS ONE* 12.7 (2017), e0181983.

[18] Constellium. *Constellium supplies advanced aluminium solutions for the electric Audi e-tron GT*. Accessed: 28 fev. 2026. 2021. URL: https://www.constellium.com/news/constellium-supplies-advanced-aluminium-solutions-for-the-electric-audi-e-tron-gt.

[19] Correlated Solutions. *VIC-2D*. Version 7, Digital Image Correlation software. https://www.correlatedsolutions.com. Irmo, SC, USA: Correlated Solutions, Inc., 2020.

[20] Frank Czerwinski. “Current Trends in Automotive Lightweighting Strategies and Materials”. In: *Materials* 14.21 (2021). ISSN: 1996-1944. DOI: 10.3390/ma14216631. URL: https://www.mdpi.com/1996-1944/14/21/6631.

[21] Dantec Dynamics. *Istra4D*. Digital image correlation software. https://www.dantecdynamics.com. Ulm, Germany: Dantec Dynamics GmbH.

[22] Geoffrey Davies. *Materials for Automobile Bodies*. 2nd. Oxford: Butterworth-Heinemann, 2012. ISBN: 978-0-08-096979-4.

[23] Uyime Donatus et al. “Corrosion Resistance of Precipitation-Hardened Al Alloys: A Comparison between New Generation Al-Cu-Li and Conventional Alloys”. In: *Advanced Aluminium Composites and Alloys*. Ed. by Leszek A. Dobrzański. IntechOpen, 2020. ISBN: 978-1-83880-456-5. DOI: 10.5772/intechopen.92807.

[24] D. S. Dugdale. “Yielding of steel sheets containing slits”. In: *Journal of the Mechanics and Physics of Solids* 8.2 (1960), pp. 100–104.

[25] J. D. Eshelby. “The force on an elastic singularity”. In: *Philosophical Transactions of the Royal Society of London. Series A, Mathematical and Physical Sciences* 244.877 (1951), pp. 87–112.

[26] European Aluminium. *Aluminium Automotive Manual – Section 2: Materials*. European Aluminium Association. Brussels, Belgium, 2015. URL: https://european-aluminium.eu/resource-hub/aluminium-automotive-manual/.

[27] European Aluminium and Ducker Carlisle. *Aluminium Usage in Cars Surges as Automotive Industry Shifts Towards Electrification*. Online PDF. Accessed: 2 mar. 2026. May 2023. URL: https://european-aluminium.eu/wp-content/uploads/2023/05/23-05-02-European-Aluminium_PR_Aluminium-Usage-in-Cars-Surges-as-Automotive-Industry-Shifts-Towards-Electrification.pdf.

[28] European Commission. *Cars and Vans – CO2 Emission Standards*. https://climate.ec.europa.eu/eu-action/transport-decarbonisation/road-transport/cars-and-vans_en. Automotive Package, December 2025. Accessed 2026. 2025.

[29] European Parliament and Council of the European Union. *Regulation (EU) 2023/851 of the European Parliament and of the Council of 19 April 2023 amending Regulation (EU) 2019/631 as regards strengthening the CO2 emission performance standards for new passenger cars and new light commercial vehicles*. Official Journal of the European Union, L 110/5. Accessed a: 28 fev. 2026. Apr. 2023. URL: https://eur-lex.europa.eu/eli/reg/2023/851/oj.

[30] Dingqin Feng et al. “Crack Detection of Asphalt Concrete Using Combined Fracture Mechanics and Digital Image Correlation”. In: *arXiv preprint arXiv:2305.05057* (2023).

[31] Fernando José Ferreira. “Análise do Comportamento Dinâmico de Componentes Estruturais sob Solicitações Generalizadas”. PhD thesis. Porto, Portugal: Faculdade de Engenharia, Universidade do Porto, 2003.

[32] A. A. Griffith. “The phenomena of rupture and flow in solids”. In: *Philosophical Transactions of the Royal Society of London. Series A, Containing Papers of a Mathematical or Physical Character* 221 (1921), pp. 163–198.

[33] A. L. Gurson. “Continuum theory of ductile rupture by void nucleation and growth: Part I—Yield criteria and flow rules for porous ductile media”. In: *Journal of Engineering Materials and Technology* 99.1 (1977), pp. 2–15. DOI: 10.1115/1.3443401.

[34] J. W. Hutchinson. “Singular behaviour at the end of a tensile crack in a hardening material”. In: *Journal of the Mechanics and Physics of Solids* 16.1 (1968), pp. 13–31. DOI: 10.1016/0022-5096(68)90014-8.

[35] International Energy Agency. *Global EV Outlook 2024*. Tech. rep. License: CC BY 4.0. Paris: IEA, 2024. URL: https://www.iea.org/reports/global-ev-outlook-2024.

[36] G. R. Irwin. “Analysis of stresses and strains near the end of a crack traversing a plate”. In: *Journal of Applied Mechanics* 24.3 (1957), pp. 361–364.

[37] G. R. Irwin. “Plastic zone near a crack and fracture toughness”. In: *Proceedings of the 7th Sagamore Ordnance Materials Research Conference*. Vol. 4. Syracuse University Research Institute, 1960, pp. 63–78.

[38] Gordon R. Johnson and William H. Cook. “A constitutive model and data for metals subjected to large strains, high strain rates and high temperatures”. In: *Proceedings of the 7th International Symposium on Ballistics*. The Hague, The Netherlands. 1983, pp. 541–547.

[39] K. Kishimoto, S. Aoki, and M. Sakata. “On the path independent integral $\hat{J}$”. In: *Engineering Fracture Mechanics* 13.4 (1980), pp. 841–850. DOI: 10.1016/0013-7944(80)90015-6.

[40] H. Kolsky. “An investigation of the mechanical properties of materials at very high rates of loading”. In: *Proceedings of the Physical Society. Section B* 62.11 (1949), p. 676.

[41] P. Lava, S. Cooreman, and D. Debruyne. “Study of systematic errors in strain fields obtained via DIC using heterogeneous deformation generated by plastic FEA”. In: *Optics and Lasers in Engineering* 48.4 (2010), pp. 457–468.

[42] D. R. Lesuer. *Experimental investigations of material models for Ti-6Al-4V titanium and 2024-T3 aluminum*. Tech. rep. DOT/FAA/AR-00/25. Federal Aviation Administration, 1999.

[43] Marc A. Meyers. *Dynamic Behavior of Materials*. New York: John Wiley & Sons, 1994. ISBN: 978-0-471-58262-5.

[44] Grażyna Mrówka-Nowotnik, Jan Sieniawski, and Adam Nowotnik. “Tensile properties and fracture toughness of heat treated 6082 alloy”. In: *Journal of Achievements in Materials and Manufacturing Engineering* 17.1–2 (2006), pp. 105–108.

[45] Grażyna Mrówka-Nowotnik, Jan Sieniawski, and Małgorzata Wierzbińska. “Intermetallic phase particles in 6082 aluminium alloy”. In: *Archives of Materials Science and Engineering* 28.2 (2007), pp. 69–76.

[46] T. Nakamura, C. F. Shih, and L. B. Freund. "Analysis of a dynamically loaded three-point-bend ductile fracture specimen". In: *Engineering Fracture Mechanics* 25.3 (1986), pp. 323–339. DOI: 10.1016/0013-7944(86)90129-3.

[47] A. Olasumboye, P. Omoniyi, and G. Owolabi. "High Strain Rate Deformation of Heat-Treated AA2519 Alloy". In: *Materials* 17.23 (2024), p. 5823.

[48] E. Orowan. "Fracture and strength of solids". In: *Reports on Progress in Physics* 12.1 (1949), pp. 185–232.

[49] Bing Pan. "Reliability-guided digital image correlation for image deformation measurement". In: *Applied Optics* 48.8 (2009), pp. 1535–1542.

[50] A. K. Pandouria, S. Kumar, and V. Tiwari. "Determination of static and dynamic fracture initiation toughness and numerical simulation of dynamic 3-point bend experiments of Al6063-T6". In: *Mechanics Research Communications* 128 (2023), p. 104070. DOI: 10.1016/j.mechrescom.2023.104070.

[51] Anoop Kumar Pandouria and Vikrant Tiwari. "Evaluation of modelling parameters for AA2014-T6 in simulating dynamic fracture event". In: *International Journal of Impact Engineering* 180 (2023), p. 104712.

[52] Salman Pervaiz. "Investigation Cooling and Lubrication Strategies for Sustainable Machining of Titanium Alloys". PhD thesis. Apr. 2014.

[53] Ian J. Polmear. *Light Alloys: From Traditional Alloys to Nanocrystals*. 4th ed. Oxford: Butterworth-Heinemann, 2006. ISBN: 978-0-7506-6371-7.

[54] K. Ravi-Chandar. *Dynamic Fracture*. Amsterdam: Elsevier, 2004. ISBN: 978-0-08-044352-2.

[55] J. R. Rice. "A path independent integral and the approximate analysis of strain concentration by notches and cracks". In: *Journal of Applied Mechanics* 35.2 (1968), pp. 379–386.

[56] J. R. Rice and G. F. Rosengren. "Plane strain deformation near a crack tip in a power-law hardening material". In: *Journal of the Mechanics and Physics of Solids* 16.1 (1968), pp. 1–12. DOI: 10.1016/0022-5096(68)90013-6.

[57] J. R. Rice and D. M. Tracey. "On the ductile enlargement of voids in triaxial stress fields". In: *Journal of the Mechanics and Physics of Solids* 17.3 (1969), pp. 201–217. DOI: 10.1016/0022-5096(69)90033-7.

[58] L. Rubio, J. Fernández-Sáez, and C. Navarro. "Determination of dynamic fracture-initiation toughness using three-point bending tests in a modified Hopkinson pressure bar". In: *Experimental Mechanics* 43.4 (2003), pp. 379–386.

[59] Matthias Rudolph et al. "Technology Trends in High-voltage Battery Development". In: *MTZ worldwide* 84.7-8 (2023), pp. 16–21. DOI: 10.1007/s38313-023-1484-x.

[60] Sahand Pourhassan Shamchi. "High Strain Rate Behavior of Aerospace Materials". PhD thesis. Porto, Portugal: Faculdade de Engenharia, Universidade do Porto, 2021.

[61] M. A. Sutton, J. J. Orteu, and H. Schreier. *Image Correlation for Shape, Motion and Deformation Measurements: Basic Concepts, Theory and Applications*. Springer Science & Business Media, 2009.

[62] G. I. Taylor and H. Quinney. "The latent energy remaining in a metal after cold working". In: *Proceedings of the Royal Society A* 143.849 (1934), pp. 307–326. DOI: 10.1098/rspa.1934.0004.

[63] Tomasz Trzepieciński and Sherwan Mohammed Najm. "Current Trends in Metallic Materials for Body Panels and Structural Members Used in the Automotive Industry". In: *Materials* 17.3 (2024). ISSN: 1996-1944. DOI: 10.3390/ma17030590. URL: https://www.mdpi.com/1996-1944/17/3/590.

[64] G. Ubertalli et al. "High Strain Rate Behavior of Aluminum Alloy for Sheet Metal Forming Processes". In: *Metals* 10.2 (2020), p. 242.

[65] Y. Wang and M. J. Starink. "Precipitates and intermetallic phases in precipitation hardening Al–Cu–Mg–(Li) based alloys". In: *International Materials Reviews* 50.4 (2005), pp. 193–215.

[66] A. A. Wells. "Unstable crack propagation in metals: Cleavage and fast fracture". In: *Proceedings of the Crack Propagation Symposium*. Vol. 1. College of Aeronautics, Cranfield, UK. 1961, pp. 210–230.

[67] H. M. Westergaard. "Bearing pressures and cracks". In: *Journal of Applied Mechanics* 6.2 (1939), A49–A53.

[68] M. J. Worswick et al. "High strain rate behaviour of aluminium alloy sheet". In: *Materials Science Forum* 519 (2006), pp. 139–146.

[69] Chunjie Xia et al. "Impact of functional integration and electrification on aluminium scrap in the automotive sector: A review". In: *Resources, Conservation and Recycling* 204 (2024), p. 107474. DOI: https://doi.org/10.1016/j.resconrec.2024.107532.

[70] Ming-zhi Xing, Yong-gang Wang, and Zhao-xiu Jiang. "Dynamic fracture behaviors of selected aluminum alloys under three-point bending". In: *Defence Technology* 9.4 (2013), pp. 193–200.

[71] L. Xue and T. Wierzbicki. "Ductile fracture characterization of aluminum alloy 2024-T351 using damage plasticity theory". In: *International Journal of Applied Mechanics* 1.2 (2009), pp. 267–304. DOI: 10.1142/S1758825109000174.

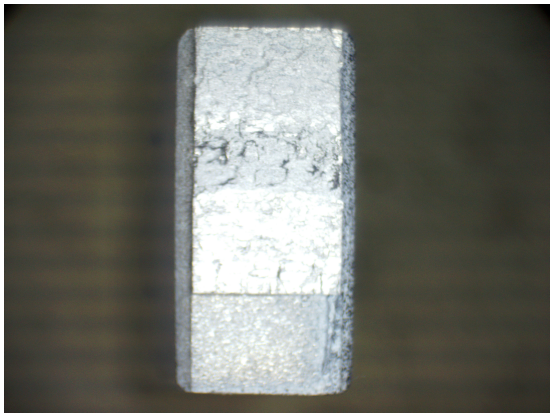
[72] T. Yokoyama. "Determination of dynamic fracture-initiation toughness using a novel impact bend test procedure". In: *Journal of Pressure Vessel Technology* 115.4 (1993), pp. 389–397. DOI: 10.1115/1.2929543.

[73] Yu Zhou et al. "Investigation of dynamic three-point bending fracture properties of SCB sandstone". In: *Theoretical and Applied Fracture Mechanics* 129 (2024), p. 104232.

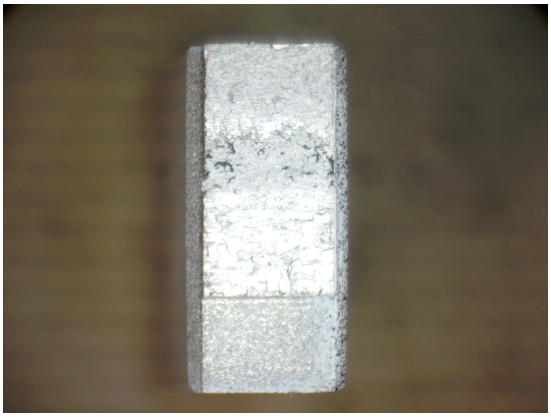
Appendix A

Quasi-Static Fracture Surfaces

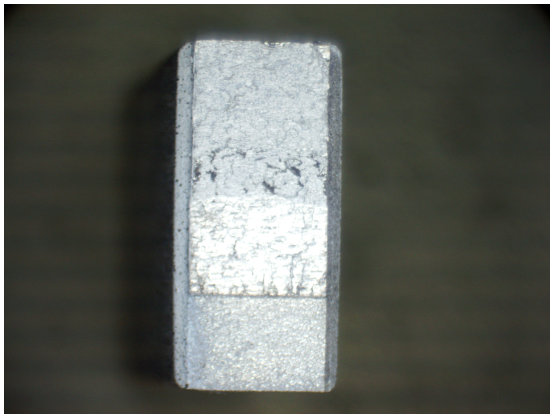
This appendix collects the fracture surface photographs of the quasi-static specimens. For each specimen, the four images used in the nine-point crack-length measurement of Section 3.7.2 are shown.



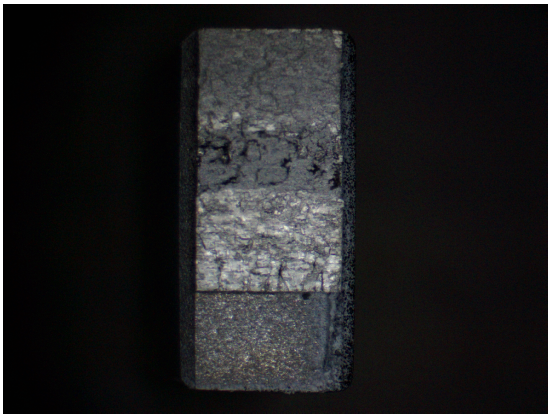
(a)



(b)

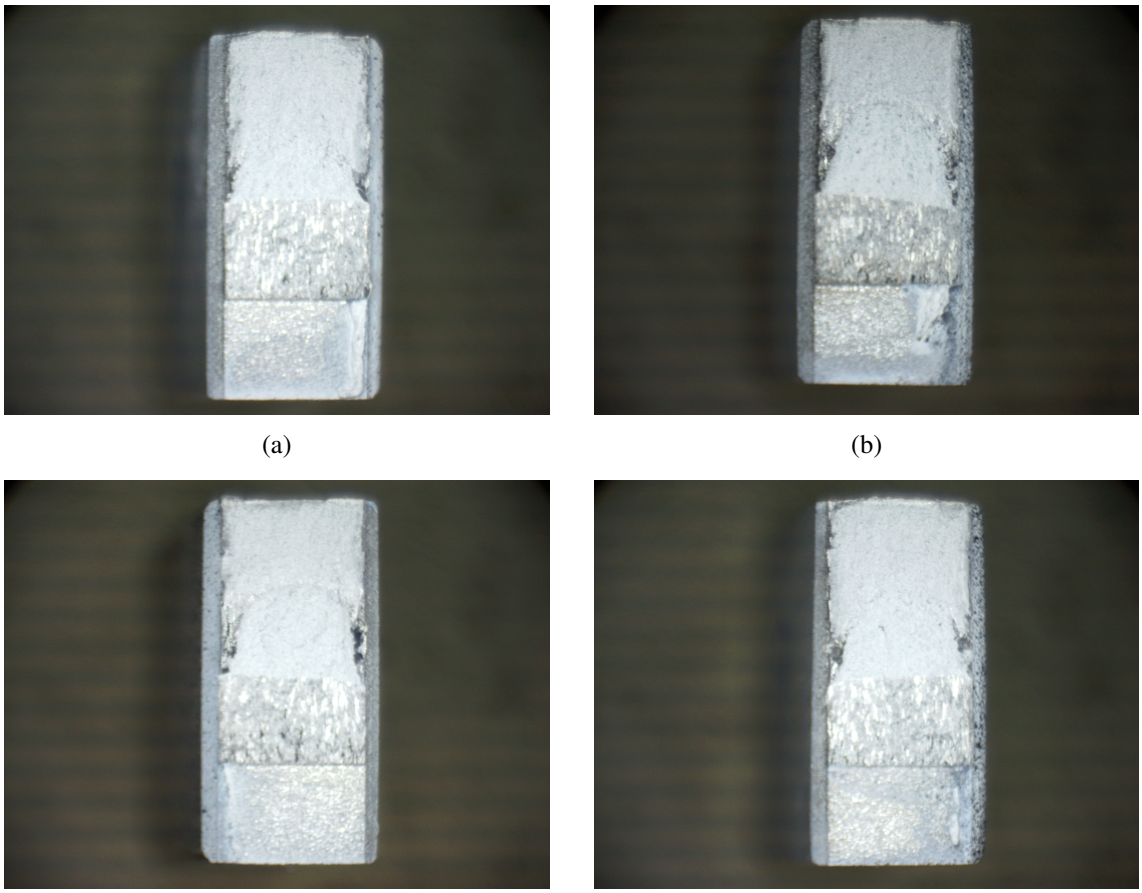


(c)



(d)

Figure A.1: Fracture surfaces of AA2024



(a) (b)

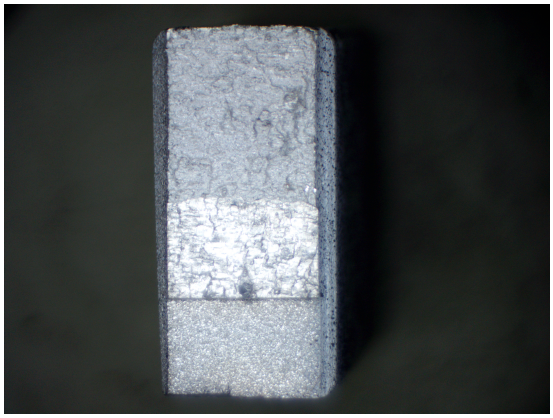
(c) (d)

Figure A.2: Fracture surfaces of AA6082-T651

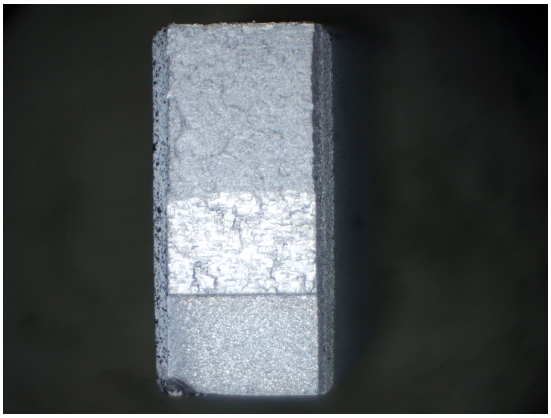
Appendix B

Dynamic Fracture Surfaces

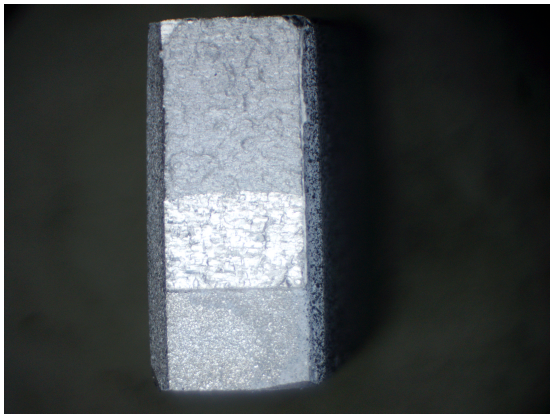
This appendix collects the fracture surface photographs of the dynamic specimens. For each specimen, the four images used in the nine-point crack-length measurement of Section 3.7.2 are shown.



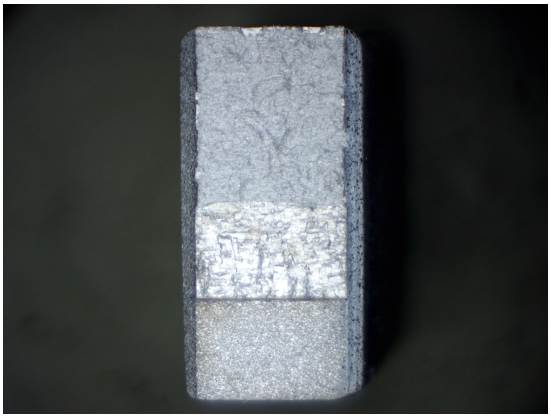
(a)



(b)

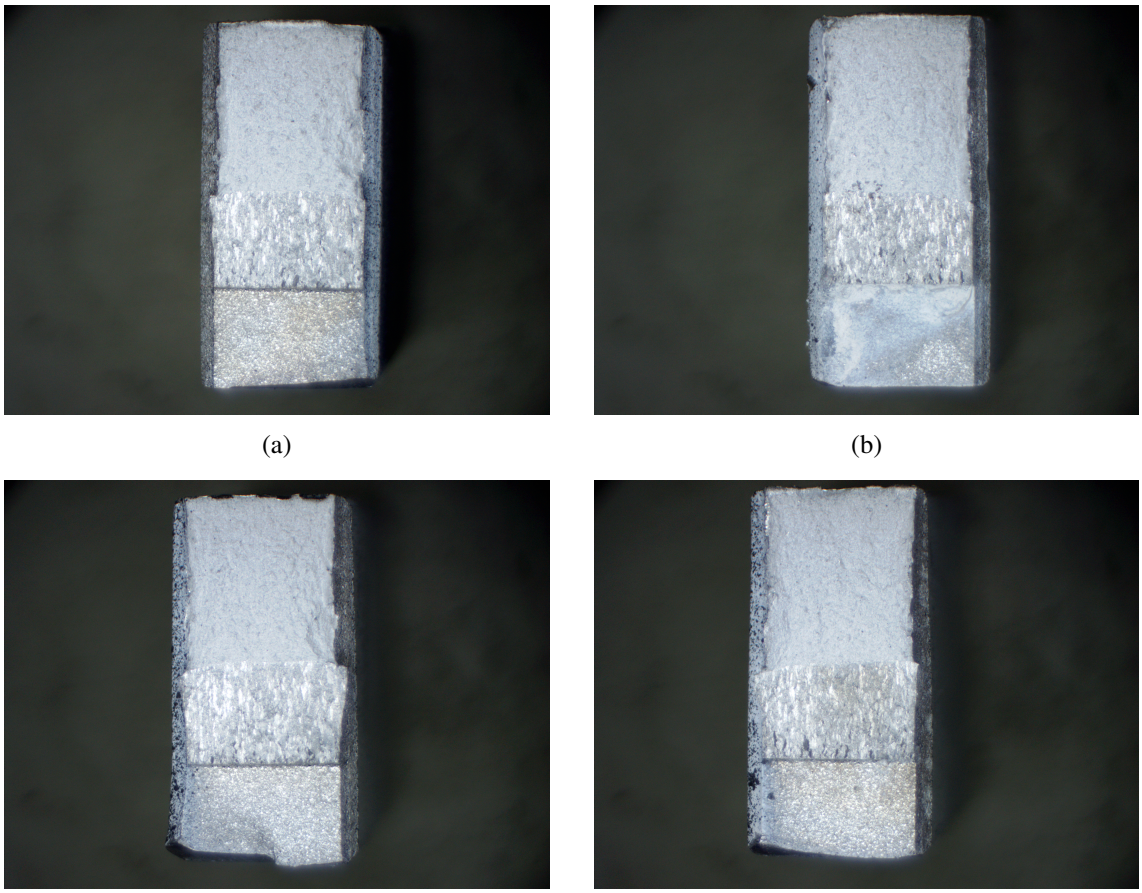


(c)



(d)

Figure B.1: Fracture surfaces of AA2024



(a) (b)

(c) (d)

Figure B.2: Fracture surfaces of AA6082-T651

Appendix C

SHPB Force Signals

This appendix collects the incident, reflected and transmitted forces of the eight dynamic specimens, referred to the specimen by the synchronisation of Section 3.8. The representative traces were discussed in Section 4.3.1; the remaining specimens are shown here.

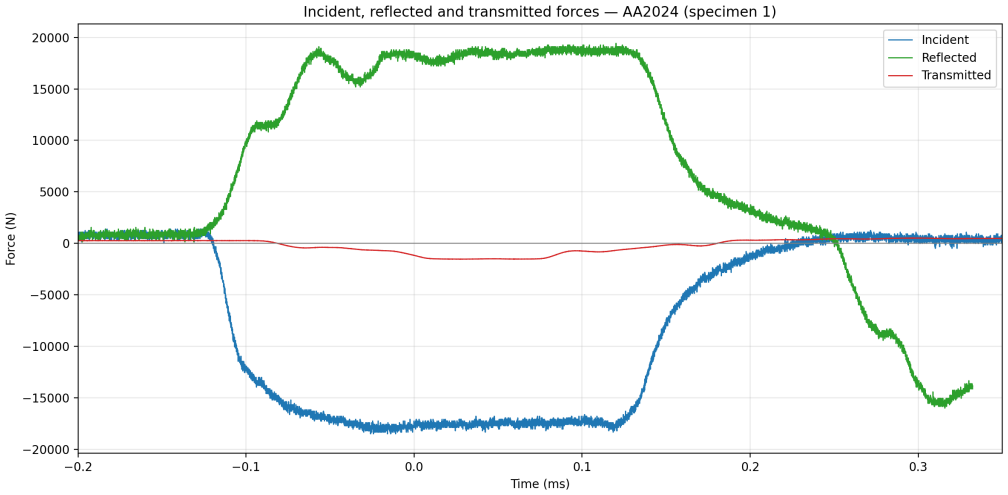


Figure C.1: Incident, reflected and transmitted forces, AA2024, specimen 1.

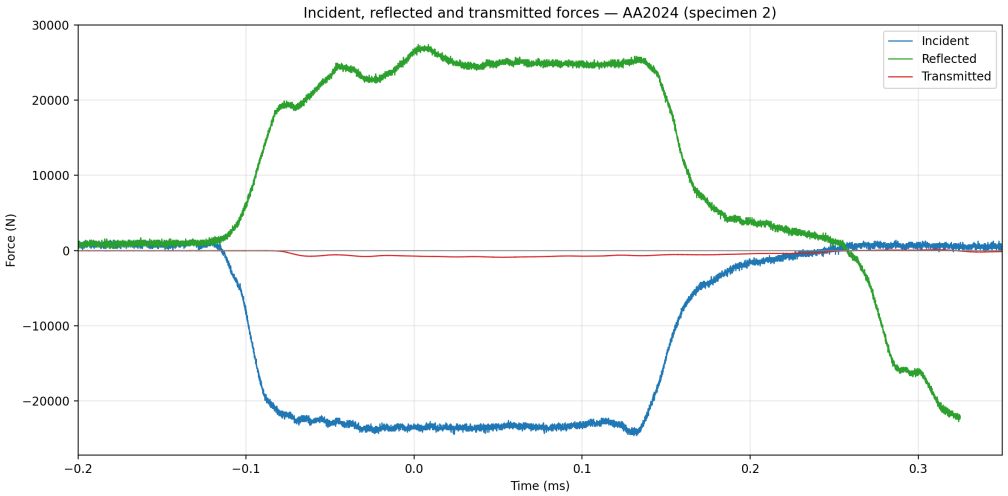


Figure C.2: Incident, reflected and transmitted forces, AA2024, specimen 2.

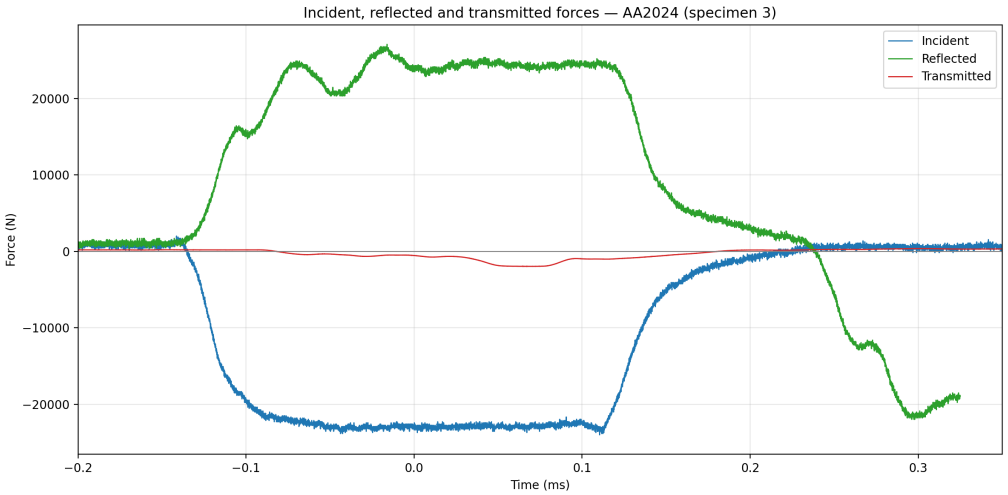


Figure C.3: Incident, reflected and transmitted forces, AA2024, specimen 3.

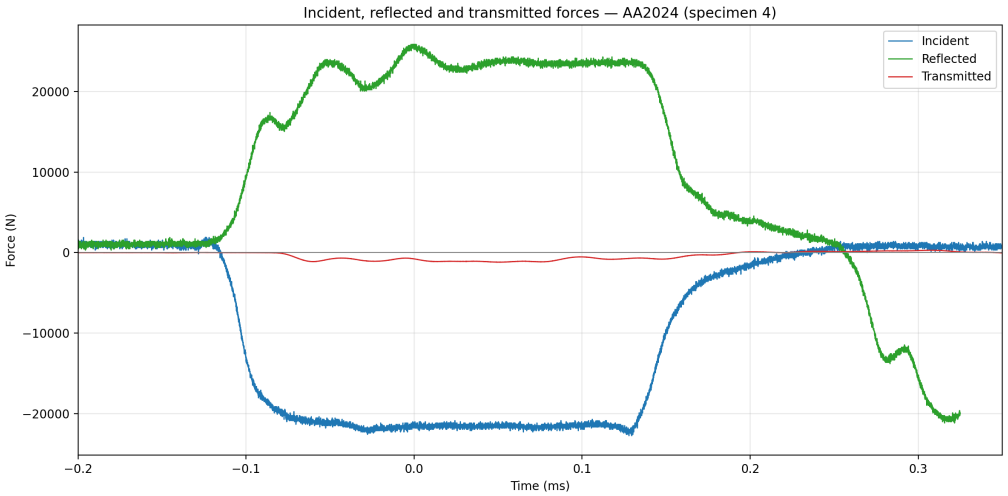


Figure C.4: Incident, reflected and transmitted forces, AA2024, specimen 4.

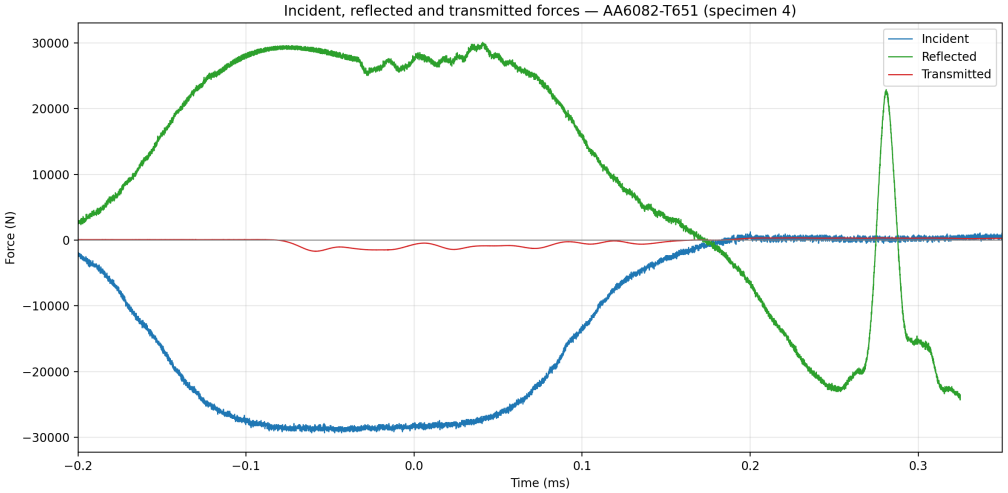


Figure C.5: Incident, reflected and transmitted forces, AA6082-T651, specimen 4.

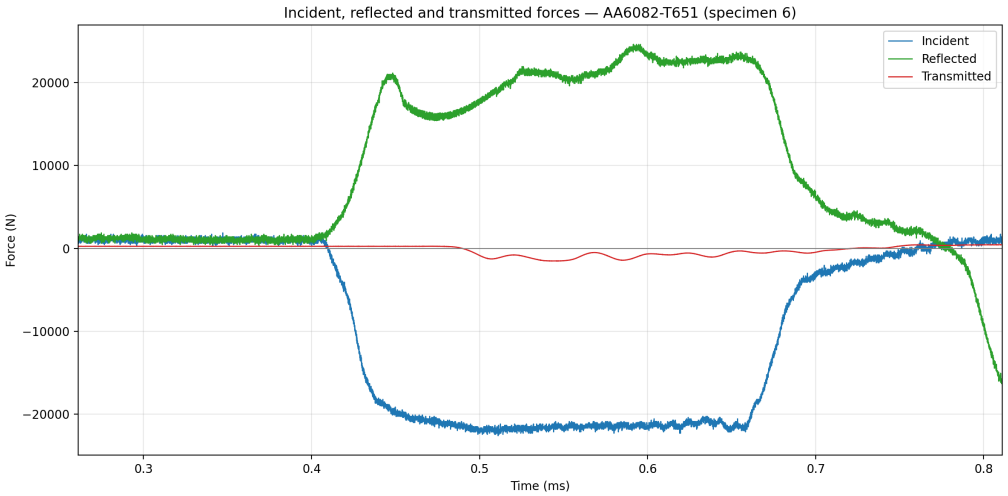


Figure C.6: Incident, reflected and transmitted forces, AA6082-T651, specimen 6.

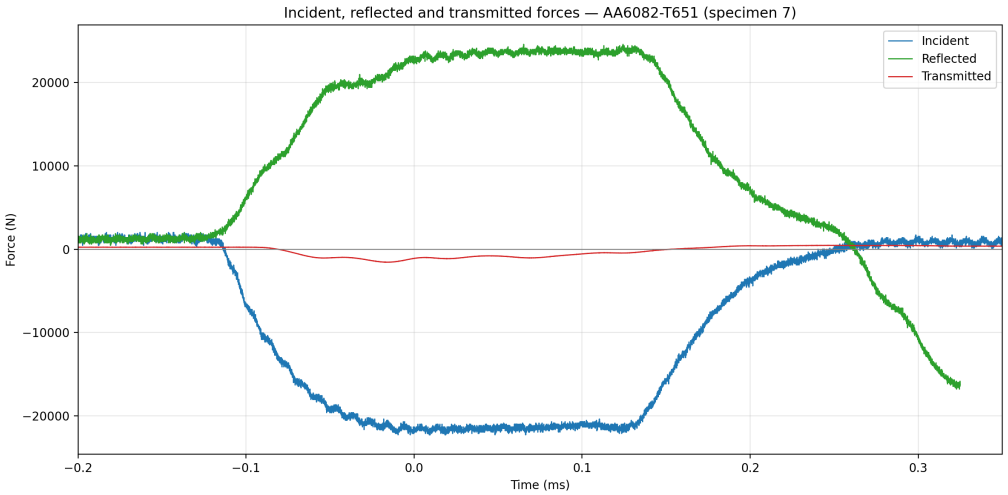


Figure C.7: Incident, reflected and transmitted forces, AA6082-T651, specimen 7.

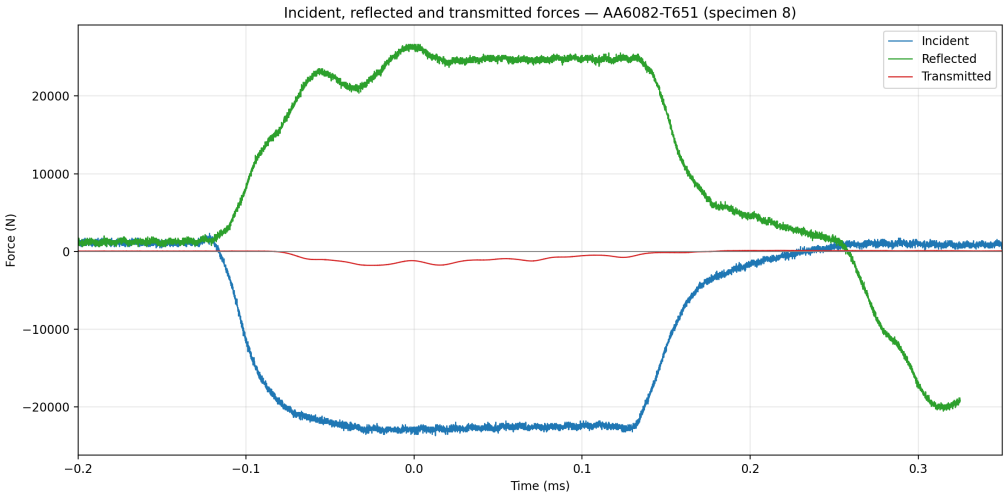


Figure C.8: Incident, reflected and transmitted forces, AA6082-T651, specimen 8.